이학박사학위논문

Theoretical Study on the Structure and Energetics of Energy Storage Materials

에너지 저장 물질의 구조와 에너지론에 대한 이론적 연구

2018년 8월

서울대학교 대학원
물리천문학부
정종현

Theoretical Study on the Structure and Energetics of Energy Storage Materials

에너지 저장 물질의 구조와 에너지론에 대한 이론적 연구

지도교수 박철환

이 논문을 이학박사 학위논문으로 제출함
2018년 7월

서울대학교 대학원
물리천문학부
정종현

정종현의 박사 학위논문을 인준함
2018년 7월

위 원 장	박 건 식	(인)
부위원장	박 철 환	(인)
위 원	이 탁 희	(인)
위 원	민 홍 기	(인)
위 원	홍 석 륜	(인)

Theoretical Study on the Structure and Energetics of Energy Storage Materials

Jong Hyun Jung

Supervised by

Associate Professor **Cheol-Hwan Park**

A Dissertation

Submitted to the Faculty of

Seoul National University

in Partial Fulfillment of

the Requirements for the Degree of

Doctor of Philosophy

July 2018

Department of Physics and Astronomy

The Graduate School

Seoul National University

Abstract

Theoretical Study on the Structure and Energetics of Energy Storage Materials

Jong Hyun Jung
Department of Physics and Astronomy
The Graduate School
Seoul National University

The pollution of fossil fuels used by vehicles can be significantly reduced if hydrogen is used as an energy carrier. The storage of hydrogen is a crucial research area for commercial application of this hydrogen energy. Currently hydrogen is stored in a pressure vessel of 700 atm, and this poses a potential hazard.

Firstly, the hydrogen storage in magnesium amide ($Mg(NH_2)_2$) using chemical bonding is investigated. This is an alternative, safe method to the high pressure vessel because the strong chemical bonding stabilizes hydrogen gas in a solid. Magnesium amide and lithium hydride (LiH) produces H_2 upon ball milling. When KH is introduced in the system, it is known that the high reaction temperature of the hydrogen releasing reaction is reduced. For practical applications, the temperature needs to be reduced further, and for this purpose, basic un-

derstanding of the reaction is required. The interaction of hydrogen with atoms in the system and the effect of KH on the reaction has not been investigated at the molecular level. Here, we intend to explain the gas-phase reaction mechanism of $Mg(NH_2)_2$ and LiH to produce H_2 using *ab initio* electronic structure and total energy calculations based on the density functional theory. We also study the mechanism of the effect KH on the reaction.

Secondly, we propose the storage of hydrogen in the potential well of layered materials. This is to compensate the high reaction temperature and slow kinetics of the chemically bonded systems. The charging and discharging of H_2 in these systems is slow because the strong chemical bond of H_2 should be broken and formed again. Layered materials are advantageous over these systems because relatively weak interaction by physisorption increases the speed of desorption and adsorption of H_2. Two candidate layered materials are intercalated gibbsite and intercalated FeS.

The hydrogen storage mechanism in intercalated gibbsite is investigated. Specifically, $NiSO_4$-intercalated gibbsite, and $Ni(COO)_2$-intercalated gibbsite are studied. We calculate the binding energy for H_2 molecules in these systems. The strength of physisorption is advantageous for storing H_2 safely under low pressure, with fast kinetics at room temperature. We estimated the storage density at the room temperature using the grand canonical Monte Carlo simulation.

Also, the electronic properties, adsorption and intercalation of another candidate layered material FeS is studied. Since this material has high surface area and is metallic, it can be useful for supercapacitor also. When the size of intercalate increases from NH_3 to tetraalkylammonium hydroxides (tetraethylammonium hydroxide and tetrabutylammonium hydroxide), the interlayer spacing

increased. This tuning of interlayer spacing will be useful for optimization of hydrogen storage material or supercapacitor electrode. The charge transfer and intercalation energy are studied. Moreover, as a basic study of this material, the electronic structure of monolayer and bulk FeS are compared. The adsorption of common atoms and molecules in the experimental conditions have also been studied to serve as a reference for future experiments.

Keywords : Hydrogen storage, Layered material, Density functional theory (DFT), Magnesium amide ($Mg(NH_2)_2$), gibbsite ($Al(OH)_3$), Tetragonal FeS (mackinawite)

Student Number : 2011-20422

Contents

List of Figures

List of Tables

Chapter 1

Introduction to the hydrogen storage

Hydrogen (H_2) is an environment-friendly energy carrier that can reduce the pollution of fossil fuels combusted in on-board vehicles. However, hydrogen gas is very bulky in its gas phase, and therefore the increase of storage density is a major issue for commercialization of hydrogen energy. Figure 1.1 shows the increasing interest on the problem of hydrogen storage and major journals concerning the issues. Since 2001, the interest steadily increased and, even The hydrogen storage methods have been reviewed previously [1, 6–13]. Here, we briefly review the basic principles of storage methods focusing on chemisorption in metal hydride and physisorption. Then we review recent research on hydrogen storage methods. The goal of hydrogen storage density set by the US Department of Energy is 5.5 wt% [14]. Currently vehicles such as Nexo by Hyundai and Mirai by Toyota store H_2 in a high pressure vessel of 700 atm. Although the vessels are made up of strong carbon-fiber-reinforced materials [15], this high pressure obviously poses a safety problem.

Various hydrogen storage methods have been proposed. The mechanism of hydrogen storage can be categorized by its binding energy as shown in Fig. 1.2 [1]. Hydrogen atom can be stored in chemical hydrides such as methane, or CH_4. 400 kJ/mol is required to separate a H atom from CH_4 and form H_2 molecules. This high energy is supplied by high temperature. In a vehicle, the temperature is the room temperature, and therefore increasing the temperature requires ad-

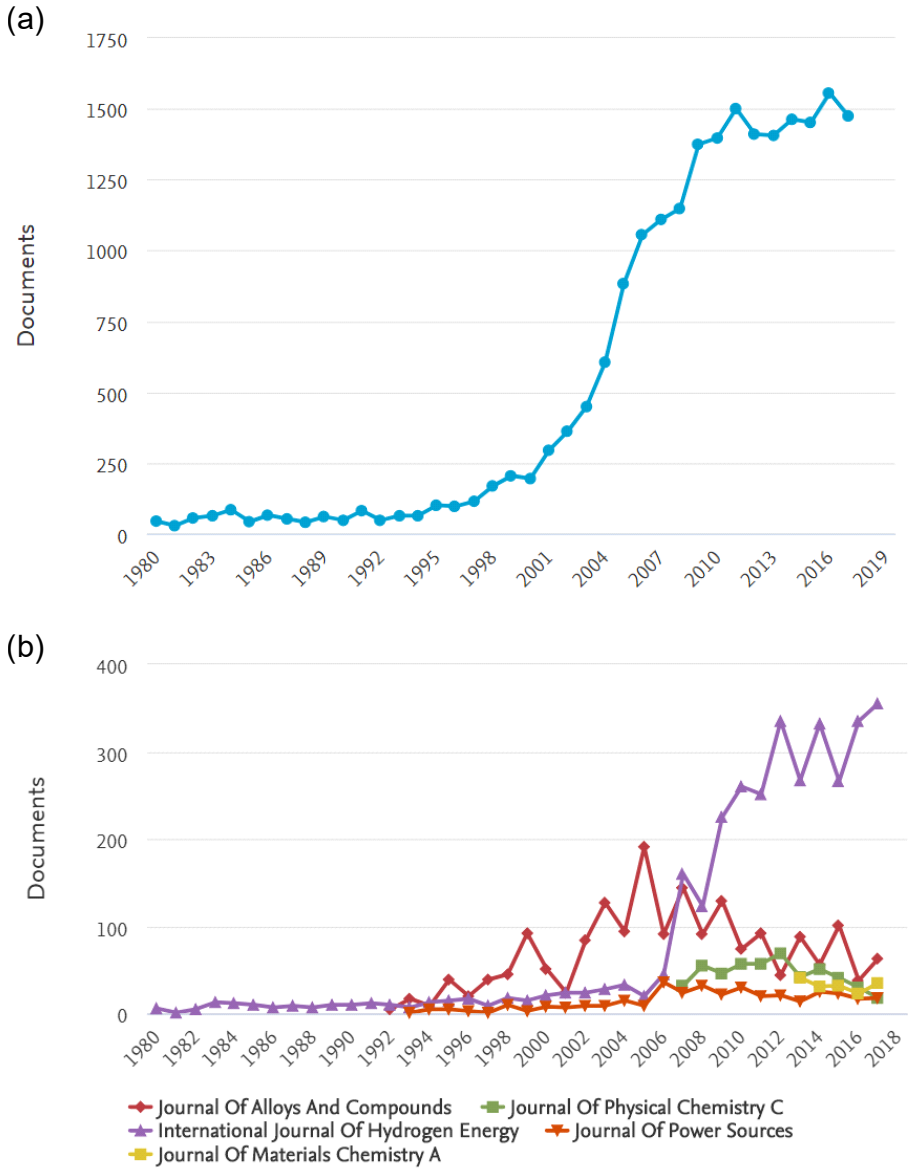

Figure 1.1: The statistics for scientific documents on hydrogen storage collected and analyzed by `scopus.com`. (a) Total number of documents containing the phrase "hydrogen storage." showing increased interest on the topic. (b) The number of documents per year sorted by major journals.

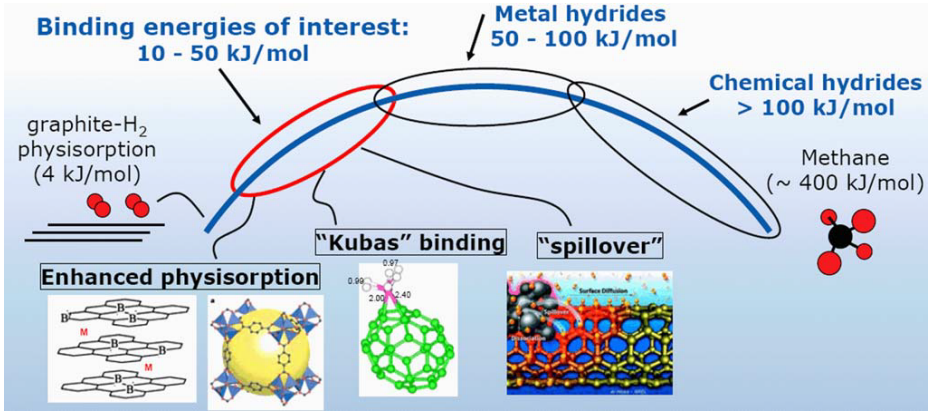

Figure 1.2: The overview of hydrogen storage mechanism categorized by its binding energy. Reprinted from a work by Ströbel et al. [1].

ditional energy. It is desirable to reduce the temperature for obtaining H_2 gas since it requires less additional energy. Metal hydrides has less binding energy in the range of 50–100 kJ/mol, and thus the temperature can be reduced. If the binding energy can be further reduced, then H_2 gas can be obtained at the room temperature. The corresponding binding energy of interest is 10–50 kJ/mol, and the lower limit is set in order to store a significant amount of H_2 gas at the room temperature. The binding energy of interest can be obtained by various mechanisms. Since the binding energy a H_2 molecule to a raw graphite is about 4 kJ/mol, or 40 meV, the strength of physisorption is needed to be enhanced by using metal doping or by using metal organic framework. Or *d* orbital of transition metals may interact to unfilled antibonding H_2 orbital and this interaction is called the Kubas binding. Some suggested that atoms may catalyze a H_2 molecule and split it to atoms, and this is called spillover.

1.1 Chemisorption in metal hydrides

Metal hydrides lower the binding energy of a H atom compared to CH_3, and thus the reaction temperature is reduced. Examples of metal hydrides include MgH_2 and $LiBH_4$. H_2 is charged in the hydrides at high H_2 partial pressure environment, and discharged at low H_2 partial pressure environment at high temperature. For $Mg(NH_2)$ and LiH system, when the solid-phase materials are mixed by ball milling, and heated, the H_2 gas is generated. Compared th the high pressure vessel, the pressure of the system is low because a H_2 molecule in gas is dissociated and stored in solid metal hydrides (Table 1.1). Therefore metal hydride system is much safer than the high pressure vessel. A disadvantage of metal hydride is that the charging and discharging of H_2 is slow, or the kinetics is slow compared to the high pressure vessel. This is because the chemical bond of a H_2 molecule should be broken or formed, and this reaction needs to overcome energy barriers. However, for the high pressure vessel, H_2 is stored in gas phase, the phase of the H_2 does not change, and the energy barrier associated with the phase change does not exist. Metal hydride system has another disadvantage that, to overcome the energy barrier, the system should be heated to greater than usually 180 °C. Our material $Mg(NH_2)_2$ and LiH with K doping can reduce the temperature to $\sim$130 °C and will be investigated in Chapter 3.

Recently progress on hydrogen storage by chemisorption focusing on metal hydrides have been reviewed [16–19]. There remains a need for a review on more recent literature. Cho et al. stored H_2 in hexagonal Mg nanocrystals coated by reduced graphene oxide which selectively allows the influx of H_2 while protecting the entrance of O_2 and H_2O [20]. The gravimetric storage density was 6.5 wt% and the volumetric storage density was very high 105 g/L since H_2 is

Table 1.1: A comparison of hydrogen storage methods

	Compression	Chemical bond	Physisorption	
			Metal organic framework, carbon materials	Potential well in layered material
Pressure (atm)	700	Low	1 – 100	100
Kinetics	Fast	Slow	Fast	Fast
Temperature	Room temperature	High, >180°C (Our proposed material: ∼130°C)	Low (77 K)	Room temperature
Storage density	High	High	Moderate	Moderate

stored in a solid phase (Table 1.2). Zhang et al. reported the storage of H_2 in Mg_2NiH_4 nanoparticles by using a microencapsulated nanoconfinement technique [21]. To increase the kinetics, the small size of a sample is beneficial, but then the nanoparticle suffer from aggregation and surface passivation. By coating the Mg_2NiH_4 nanoparticles though oxidation and forming MgO layer stabilized the nanoparticles while allowing the entrance of H_2 only. The nanostructuring enabled a very low activation energy (31.2 kJ/mol$^-$1) for dehydrogenation reaction. Lototskyy et al. with industrial customers combined AB_2-type H_2 storage system with a compressed H_2 composite cylinder and proton exchange membrane fuel cell. The resulting H_2 storage capacity was 19 nm^3 or 1.7 kg where pressure is lower than 100 bar near the room temperature [22]. Huang et al. doped MgH_2 by Co or Ni, and wrapped its nanoparticles by carbon and lowered the dehydrogenation temperature of MgH_2 to 275.7 °C [23]. Muthu et al. ultrasonicated multi-walled carbon nanotubes and hexagonal boron nitride nanocomposite. The storage capacity of 2.3 wt% was achieved and the desorption of H_2 started at 120 °C. Due to the high desorption temperature, H_2 is expected to chemisorbed on the material [24].

Table 1.2: Recent progress on hydrogen storage properties of various materials between 2016 and 2018 (the present). GO: graphene oxide, CNT: carbon nanotube.

Material	Storage density, Gravimetric (wt%)	Volumetric (g/L)	Temperature (°C)	Pressure (atm)	Reference
Mg nanoparticles in reduced GO	6.5	105	$T_{\text{des}} = 300$	0	[20]
Mg_2NiH_4 nanoparticles coated by MgO layer	-	-	$T_{\text{des}} = 176.8$	-	[21]
AB_2, where A=(Ti, Zr), B=(Fe, Cr, Mn, Ni) with compression cylinders	(Total 1.7 kg)	-	$T_{\text{des}} = -25$ to 75	0.1 – 200	[22]
MgH_2-6% Co coated by C	6.1	-	$T_{\text{des}} = 250$	-	[23]
Multi-walled CNT/h-BN	2.3	-	$T_{\text{des}} = 120$	-	[24]
MOF with open Cr^{2+} sites	2.4	-	-196	1.2	[25]
Mg-containing MOF	1.8	9.4	25	100	[26]

Continued on the next page

Material	Storage density, Gravimetric (wt%)	Storage density, Volumetric (g/L)	Temperature (°C)	Pressure (atm)	Reference
Pd-CNT/Pd/porous silicon/Si, galvanostatic characterization	2.05	-	-	-	[27]
Sc, Ti-CNT	5.85 (theory)	-	27	660	[28]
Mesoporous GO with K	4.65	-	27	40	[29]
Reduced-GO foam with polydopamine and Pt nanoparticles	3.19	-	25	100	[30]
Monolayer $MnPS_3$	0.07	-	25	2.0	[31]
Li-doped random CNT network (Li:C = 1:5)	3.3 (theory)	22 (theory)	25	100	[32]
Li-doped graphene-fullerene nanocomposite	4.78 (theory)	-	-196	1	[33]

1.2 Physisorption in porous materials

1.2.1 Carbon materials and metal organic framework

The storage using chemical amide has several fundamental issues. It requires still a high temperature [34] and the desorption and adsorption of H_2 is relatively slow because strong chemical bond of H_2 should be broken or formed.

An alternative method is to store H_2 in a porous material with large surface area because the storage density increases linearly with the surface area (Fig. 1.3). This is because a H_2 molecules adsorbs on a surface by physisorption. The mechanism of physisorption includes van der Waals (dispersion) interaction and the interaction between a dipole and an induced dipole. Sevilla et al. fabricated polypyrrole-based activated carbons with high surface area and showed that the H_2 storage density can be increased up to 7.03 wt% by increasing the surface area to 3500 $m^2\,g^{-1}$.

Then can we use the activated carbon for a practical H_2 storage system? Only if the strength of physisorption is enhanced. The binding strength of a carbon material such as graphite is only 51.7 meV without zero-point vibration correction, and 41.6 meV by considering the vibration [35]. The binding strength is measured by scattering H_2 molecules on graphite surface. The strength is comparable to the thermal energy of the room temperature, $k_B T = 26$ meV, where k_B is the Boltzmann constant. Therefore, the large storage density is only possible at a very low temperature, for example, -196 °C. At the room temperature, graphite, activated carbon, or carbon nanotube cannot be used to store H_2 without further decoration to enhance the physisorption.

Metal organic framework (MOF) achieves the enhancement the binding strength of a H_2 molecule in a porous material by decorating metal atoms [36].

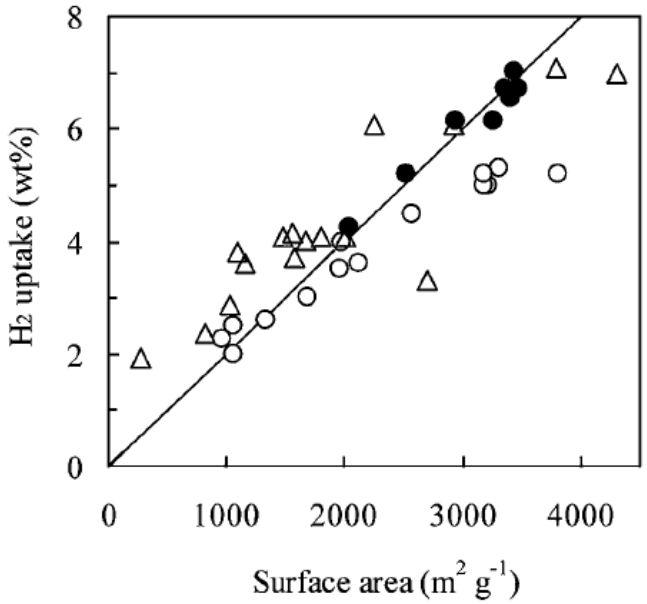

Figure 1.3: The hydrogen storage density increases linearly with the surface area of activated carbons and MOFs. Reprinted from a work by Sevilla et al. [2].

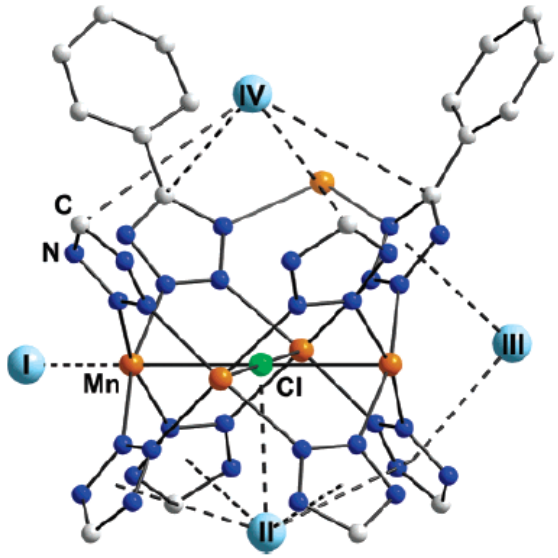

Figure 1.4: Adsorption site of D_2 in a metal organic framework. Cyan balls indicate D_2 adsorption sites revealed by neutron spectroscopy. Reprinted from a work by Dinca et al. [3].

Since metal atoms has high cohesive energy and easily form clusters, a carbon based framework is required to separate each metal atom. Dinca et al. synthesized an MOF with exposed Mn^{2+} sites and observed that D_2 bind to the Mn^{2+} atoms (Fig. 1.4) [3]. The position of the D_2 molecules were found by the Rietveld refinement of the neutron powder diffraction pattern. The gravimetric storage density reached 6.9 wt% at 77 K and 90 bar. The maximum isosteric heat of adsorption was 10.1 kJ/mol, and as the storage density increases, the heat reduced to 6 kJ/mol. However, for practical applications, room temperature storage is required, which requires further enhancement of the adsorption strength. To increase strength, the density of metal atoms were increased. Then the metal atoms form clusters due to large cohesive energy reactivity. The binding strength is rarely increased over 50 meV/H_2, and it is generally hard to solve this problem.

Recent works on H_2 storage in MOF and carbon materials have been reviewed [37, 38]. We review more recent works on carbon materials. Bloch et al. synthesized a MOF with open Cr^{2+} sites and stored 2.4 wt% of H_2 at 77 K at 1.2 atm (Table 1.2) [25]. Gygi et al. synthesized a MOF family containing Mg, Mn, Fe, Co, Ni, and Zn, and for a Mg-containing MOF, the BET surface area reached 3300 m^2/g and H_2 storage capacity was 1.8 wt% and 9.4 g/L even at the room temperature 25 °C and 100 bar [26]. Ruse et al. studied the spillover kinetics of carbon nanotube-Mg composite and the showed that thg morphology of nanotube has significant effect on the kinetics [39]. Shiraz et al. formed porous silicon on silicon substrate, deposited Pd nanoparticles on the porous silicon, and grew carbon nanotubes on the Pd nanoparticles, and decorated the carbon nanotubes with Pd. The hydrogen storage capacity reached 2.05 wt%,

and the storage density decrease by only 0.05 % after 100 cycles [27]. Manang-haya et al. performed *ab initio* and classical molecular dynamics simulation of H_2 storage in Sc and Ti-containing carbon nanotubes [28]. They calculated the theoretical storage density of 5.85 wt% at 300 K. Ariharan et al. synthesized a boron-substituted carbon material with BET surface area of 55.1 m^2/g and reported H_2 storage capacity of 5.9 wt% at 298 K and 100 bar [40]. The reported capacity is quite dubious because the value is very high given small BET surface area. Also the capacity reduced to 1.1 wt% at 77 K which seems to be contrary to a thermodynamic principle that the thermal energy stirs H_2 molecules and the amount of bound H_2 reduces as the temperature increases.

1.2.2 Potential well

An alternative approach of H_2 storage method is to store H_2 in gas-phase in the potential well of layered materials [29,41,42]. Compared to storage on the two-dimensional surface of a porous material or binding at zero-dimensional metal atoms in MOF, the concept of potential well emphasizes a storage in a three-dimensional space. The storage in the potential well is advantageous because it stores H_2 in a gas phase, and thus the degree of freedom, or the motion of H_2 is not reduced upon storage. A material that weakly attracts nearby H_2 molecules provides a stable potential well near the material (Fig. 1.5(a)). At thermal equilibrium, the density ρ_{in} of H_2, in the potential well with depth $-|U|$, is roughly proportional to the Boltzmann factor

$$\rho_{\text{in}} = \rho_{\text{out}} \exp(|U|/k_B T) \tag{1.1}$$

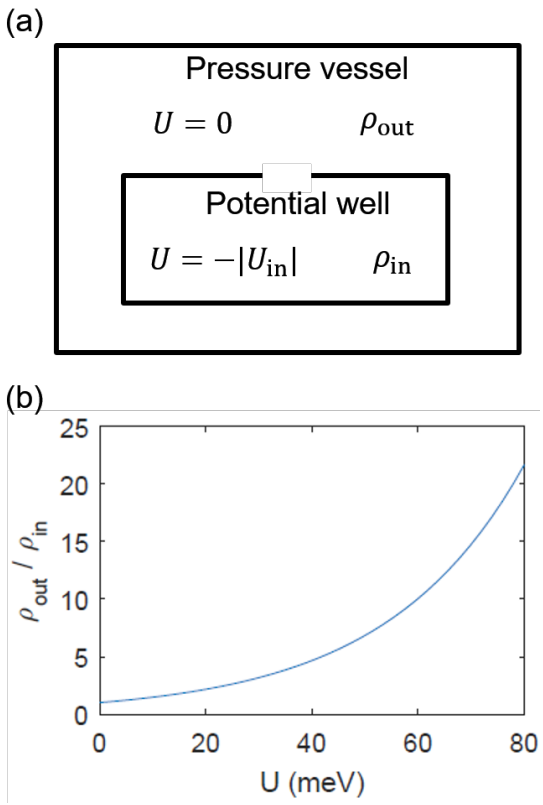

Figure 1.5: The physics of storage in a potential well. (a) A potential well inside a pressure vessel. (b) The exponential increase of storage density for an ideal gas as the potential well depth U increases.

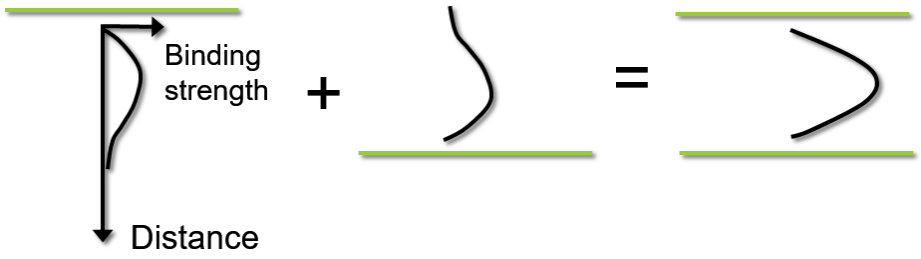

Figure 1.6: The increase of H_2 binding strength, or potential well depth by using two layers.

where k_B is the Boltzmann constant, T is the absolute temperature, and ρ_{out} is the density of H_2 outside the potential well, inside the pressure vessel. The density increases exponentially with the well depth for an ideal gas (Fig. 1.5(b)). At the room temperature, $k_BT = 26$ meV. When the potential well depth is k_BT or 26 meV, the density increases by $\exp(1)$ or 2.7. As the potential well deepens to -80 meV, the density is multiplied by 21.

The potential well can be realized by using intercalated layered materials. A layer attracts H_2 by van der Waals interaction and by polarizing H_2 by a charge. In the layered material, a H_2 molecule is attracted by both top and bottom layers, and therefore the binding strength is enhanced compared to an isolated monolayer (Fig. 1.6).

The advantage of potential well system is that the temperature need not to be high compared to the chemical hydride systems since weak interaction is easily broken. The speed of adsorption or desorption is faster since the gas phase of H_2 is kept, while in chemical hydride, the phase changes between gas and solid during chemical reaction. The applied pressure is significantly lower than compressed H_2 system.

Various systems utilizing a potential well such as pillared graphene or intercalated layered materials have been proposed. Dimitrakakis et al. theoretically proposed a pillared graphene decorated with Li cations and achieved the storage density of 6.5 wt% and 42 g/L at 300 K and 10 bar [43]. To realize the remarkable capacity, in practice, the Li atoms need to be dispersed with high density. Our coworker Kim et al. synthesized mesoporous graphene oxide by dispersing graphene oxide in KOH and treating hydrothermally [29]. Consequently, the sample became mesoporous and the physisorption of H_2 enhanced by K^+ ions, and the storage capacity reached 4.65 wt% at 4 MPa and 27 °C. H. Jung et al. fabricated reduced-graphene oxide foam with polydopamine and Pt nanoparticles, and the resulting storage capacity reached 3.19 wt% at room temperature and 100 bar [30]. Cabria et al. simulated the H_2 storage on a monolayer $MnPS_3$, which is attracting interest as a transition metal 2D layer [31]. The maximum binding energy by physisorption was -25 meV obtained by the exchange-correlation functional of Perdew, Burke, and Ernzerhof (PBE) [44] in combination with the dispersion corrected atom-centered nonlocal pseudopotentials (DCACPs). Experimental H_2 storage capacity reached 0.07 wt% at 298.15 K and 2.0 MPa, and the capacity was explained by theoretical estimation. Baykasoglu et al. investigated the effect of Li doping on the random carbon nanotube network using the grand canonical Monte Carlo (GCMC) simulation [32]. The network doped by Li atoms (Li:C = 1:5) yielded H_2 storage capacity of 3.3 wt% and 22 g/L at 298 K and 100 bars. Ozturk et al. performed GCMC simulation on Li-doped graphene-fullerene nanocomposite and resulting H_2 storage capacity was 4.78 wt % at 77 K and 1 bar [33].

1.3 The organization of the following chapters

Various H_2 storage methods are reviewed including storage using chemisorption, porous carbon materials and metal organic frameworks, and in potential wells. In the next chapter, we review the methodology for obtaining the binding energy of a H_2 molecule. In chapter 3, we will investigate the mechanism of H_2 storage in the $Mg(NH_2)_2$ and LiH system. Next, in chapter 4, we will study the storage of H_2 in the potential well of a layered material, intercalated gibbsite. Finally, in chapter 5, we will obtain the properties of another intercalated layered material, FeS, which can provide a potential well for H_2 storage.

Chapter 2

Computational Methods: Density Functional Theory

We utilized density functional theory (DFT) to calculate total energy and optimize structures for hydrogen storage in the subsequent chapters. DFT has been a workhorse for modern quantum computation of materials in physics, chemistry, and materials science for the last five decades. Its theory and historical development is already described [45, 46]. Here, we briefly review basic theory and the treatment of van der Waals interaction for evaluating the binding energy of hydrogen.

There is an ample resource for beginning graduate students to learn and run DFT calculations. A short introductory paper is written by Perdew et al., entitled "Fourteen Easy Lessons in Density Functional Theory" [47]. It succinctly introduces the concept of density as a basic variable of a quantum system, to the various approximation methods. A book chapter by Giuliani et al. describes the same topic in more detail including current density functional theory [48]. Becke has written a comprehensive review paper of DFT mainly focusing on atoms and molecules for chemistry society [49].

Martin et. al has written an encyclopedia-like book of DFT and overall electronic structure methods for solids for physics community [45]. Kohanoff has written a book on DFT for both solid and molecules, or for both physics and chemistry community [46]. For understanding the development of approx-

imation methods, a lecture series by K. Burke entitled "The ABC of DFT" is recommended [50]. A diverse benchmark tests for DFT exchange-correlation functionals for chemical phenomena is presented [51]. For example, binding energy of molecules, and energy barriers are tested.

For running DFT calculations, there is a cookbook by Scholl [52] which aims at running DFT calculations. A useful resource for the physics of each calculation step is provided in the lectures of VASP Workshop in 2003 available in `http://vasp.at/index.php/documentation`.

2.1 Basic Theory

2.1.1 Wave function versus density

Density functional theory uses electron density as a basic variable for describing a quantum system instead of its wave function. Using the wave function as a variable of a large quantum system is not quite feasible due to its large dimension.[1] We consider a system consisting of N electrons. Then the wave function has $3N$ coordinates for x, y, and z coordinates of each electron:

$$\Psi(x_1, y_1, z_1, x_2, y_2, z_2, \cdots, x_N, y_N, z_N). \tag{2.1}$$

For a system consisting of about 100 electrons such as an uranium atom ($Z = 92$), the dimension of Ψ is about 300. To write the wave function, we use 10 grid points for a dimension. Then, the values of Ψ for 10^{300} points need to be written. If we compare the number of points with 1 TB, or 10^{12} byte, the number of points is huge and cannot be written in any computer storage device. Al-

[1] The following argument based on the dimension of wavefunction and density is from a lecture by E.K.U. Gross.

though this problem is circumvented by importance sampling in accurate quantum Monte Carlo method, its cost is much higher than density functional theory. Description using the wave function does not seem to be feasible for large systems.

2.1.2 Density as a basic variable

Hohenberg and Kohn proposed that the density of the system can exactly describe the system. Since the density has only 3 coordinates:

$$n(x,y,z), \tag{2.2}$$

for the system with 100 electrons, only 10^3 grid points are needed to describe the system. Therefore, the use of density is hugely efficient than the use of wave function for a large system. Hohenberg and Kohn presented the proof for the density as a basic variable in 1964 [53]. This notion has become a basic theorem of density functional theory.

We briefly present the proof by Hohenberg and Kohn as follows. Electrons in a box are considered. Then the Hamiltonian is

$$H = T + V + U, \tag{2.3}$$

where the kinetic energy is

$$T = \frac{1}{2}\int \nabla\psi^*(\mathbf{r})\psi(\mathbf{r})d\mathbf{r}. \tag{2.4}$$

The energy from the external potential $v(\mathbf{r})$ including electric potential by nuclei

and any external source is

$$V = \int v(\mathbf{r})\psi^*(\mathbf{r})\psi(\mathbf{r})d\mathbf{r}, \tag{2.5}$$

and the energy from electron-electron interaction is

$$U = \frac{1}{2}\int \psi^*(\mathbf{r})\psi(\mathbf{r}')\psi(\mathbf{r}')\psi(\mathbf{r})d\mathbf{r}d\mathbf{r}'. \tag{2.6}$$

We assume that the ground state is non-degenerate.

The following proof is *reductio ad absurdum*. Suppose there exists another potential $v(\mathbf{r}')$ and ground state Ψ' with same density $n(\mathbf{r})$, where $v(\mathbf{r}') - v(\mathbf{r})$ is not a constant. Then from the variational property of Hamiltonian,

$$E' = (\Psi', H'\Psi') < (\Psi, H'\Psi) = (\Psi, (H + V' - V)\Psi), \tag{2.7}$$

$$E' < E + \int [v'(\mathbf{r}) - v(\mathbf{r})]n(\mathbf{r})d\mathbf{r}. \tag{2.8}$$

When we interchange primed and unprimed values, we obtain

$$E < E' + \int [v(\mathbf{r}) - v'(\mathbf{r})]n(\mathbf{r})d\mathbf{r}. \tag{2.9}$$

We add (2.8) and (2.9) and obtain an inconsistent result:

$$E + E' < E' + E. \tag{2.10}$$

Therefore, $v(\mathbf{r})$ is, up to a constant, a unique functional of $n(\mathbf{r})$. When $v(\mathbf{r})$ is given, then H is obtained. Thus, the many-particle ground state obtained from H is a unique functional of $n(\mathbf{r})$. This is surprising because although the number

of coordinates of wave function Ψ is much greater than that of $n(\mathbf{r})$, $n(\mathbf{r})$ has, in principle, the same information as Ψ has. Then Hohenberg and Kohn showed that the energy E can be obtained by minimizing the energy functional with respect to $n(\mathbf{r})$, or E of the ground state is the variational minimum of $n(\mathbf{r})$.

In the theorem, only densities associated with some other external potential (called v-representable) is considered in the variational principle. What if another density not associated with the external potential has lower energy than the ground state? Levy [54] extended the range of density from v-representable to any density derivable from an antisymmetric wavefunction (called N-representable).

Hohenberg and Kohn approximated the total energy functional $E[n]$ by using the energy from the external potential and classical electron-electron interaction energy called Hartree energy,

$$E[n] = \int v(\mathbf{r})n(\mathbf{r})d\mathbf{r} + \frac{1}{2}\int \frac{n(\mathbf{r})n(\mathbf{r}')}{|\mathbf{r}-\mathbf{r}'|}d\mathbf{r}d\mathbf{r}' + G[n]. \tag{2.11}$$

The remaining part $G[n]$ is also a unique functional of density, and can be represented as

$$G[n] = \int g_r[n(\mathbf{r})]d\mathbf{r}. \tag{2.12}$$

Hohenberg and Kohn approximated the kernel of density functional for kinetic energy as that of a free-electron gas,

$$g_r[n(\mathbf{r})] = \frac{3}{10}[k_{\mathrm{F}}(n)]^2 n, \tag{2.13}$$

where the Fermi momentum k_{F} is

$$k_{\mathrm{F}}(n) = (3\pi^2 n)^{1/3}. \tag{2.14}$$

Now, instead of this approximation, more accurate kinetic energy of single-particle Kohn-Sham orbitals are used. Hohenberg and Kohn suggested that the energy density of density functional may be expanded as terms involving the gradients of $n(\mathbf{r})$. At present, this is developed to the widely-used generalized gradient approximation.

The remaining partial energy density functional may be approximated to the low-density approximation by Wigner,

$$g_0(n) \approx \left(\frac{2.21}{r_s^2} - \frac{0.916}{r_s} - \frac{0.88}{r_s + 7.8} \right) n, \tag{2.15}$$

where r_s is the Wigner-Seitz radius of electron. Today, local density approximation fitted to quantum Monte Carlo calculations are used.

In conclusion, the density of electron can be used as a basic variable instead of a wave function. The external potential $v(\mathbf{r})$ is a unique functional of density $n(\mathbf{r})$. The energy functional of density $E[n(\mathbf{r})]$ assumes its minimum value for the correct ground state density $n(\mathbf{r})$ (relative to densities associated with some other external potential $v'(\mathbf{r})$).

2.1.3 Mapping to independent particle system

Previously we showed that the density is a basic variable of a quantum system. This is a theorem for the existence of the density functional, and we need approximations to the functional for practical utility. Otherwise, nobody would know the functional, and would not be able to calculate anything. The approximation by the kinetic energy of homogeneous electron is too crude to be useful for practical calculations. The brilliant idea of Kohn and Sham is that they approximated the kinetic energy density functional by using independent par-

ticle approximation [55]. From a theoretical point of view, they provided an exact mapping from an interacting system to non-interacting system, called exact Kohn-Sham system. Eq. 2.11 defines the remaining functional $G[n]$ which includes kinetic energy. Then

$$G[n] = T_s[n] + E_{\mathrm{xc}}[n], \tag{2.16}$$

where $T_s[n]$ is the kinetic energy of non-interacting electrons with density $n(\mathbf{r})$. Now the remaining part is $E_{\mathrm{xc}}[n]$, which represents the exchange and correlation energy of an interacting system with density $n(\mathbf{r})$. Note that exchange means the effect of antisymmetric wave function captured under Hartree-Fock level, and correlation means still remaining high-order effect.

We may express $E_{\mathrm{xc}}[n]$ as follows:

$$E_{\mathrm{xc}}[n] = \int n(\mathbf{r}) \varepsilon_{\mathrm{xc}}(n(\mathbf{r})) d\mathbf{r}, \tag{2.17}$$

where $\varepsilon_{\mathrm{xc}}$ is the exchange and correlation energy per electron. From the variational property of the total energy,

$$\int \delta n(\mathbf{r}) d\mathbf{r} = 0, \tag{2.18}$$

and

$$\int \delta n(\mathbf{r}) \left(\phi(\mathbf{r}) + \frac{\delta T_s[n]}{\delta n(\mathbf{r})} + \mu_{\mathrm{xc}}(n(\mathbf{r})) \right) d\mathbf{r} = 0, \tag{2.19}$$

where

$$\phi(\mathbf{r}) = v(\mathbf{r}) + \int \frac{n(\mathbf{r}')}{|\mathbf{r} - \mathbf{r}'|} d\mathbf{r}', \tag{2.20}$$

and

$$\mu_{\rm xc} = d(n\varepsilon_{\rm xc}(n))/dn. \tag{2.21}$$

Then we see that Eqs. (2.18, 2.19) represent noninteracting electrons moving in potential $\phi(\mathbf{r}) + \mu_{\rm xc}(n(\mathbf{r}))$. Therefore, we obtain equivalent one-particle Schrödinger equation

$$\left(-\frac{1}{2}\nabla^2 + [\phi(\mathbf{r}) + \mu_{\rm xc}(n(\mathbf{r}))]\right)\psi_i(\mathbf{r}) = \varepsilon_i\psi_i(\mathbf{r}), \tag{2.22}$$

and

$$n(\mathbf{r}) = \sum_{i=1}^{N} |\psi_i(\mathbf{r})|^2, \tag{2.23}$$

where N is the number of electrons.

Now the only physically meaningful quantity is $n(\mathbf{r})$ because the $n(\mathbf{r})$ of noninteracting electrons equals the $n(\mathbf{r})$ of interacting electrons. The eigenvectors, the noninteracting states, and the eigenvalues, ε_i, are artificially introduced to simplify the formalism.

Although the energies of noninteracting electrons ε_i does not have a physical meaning, in practice, they are regarded as an approximation to the energy of noninteracting electrons. These energies are the energies of a band structure in the single particle picture. In a crystalline solid, with periodic boundary condition, using the Bloch theorem, the crystal momentum $\mathbf{k}$ becomes a good quantum number to label the state of an noninteracting electron, and the band dispersion is obtained as the relationship between ε_i and $\mathbf{k}$.

In a crystalline solid, the evaluation of the total energy requires ill-defined infinite summation of long-ranged Coulomb potential. The Hartree energy and the Coulomb interaction of nuclei are known to be conditionally convergent,

and its physical reason is that the charge at the surface of a finite-sized crystal influences the total energy of the crystal. The formulation of total energy is obtained as a balanced Ewald summation in the momentum space [56].

2.2 Projector augmented wave method (pseudopotential)

It is well known that the chemistry of an atom or a molecule is dominated by its valence electrons, where core electrons are nearly frozen. The cause of this observation is that the core electrons are close to a nucleus and has small overlap with an electron of another atom. Also, the close distance greatly stabilizes the core electrons, and their energies are so low to interact with nearby valence electrons.

In practice, the calculation of valence electrons only can significantly reduce computational load. For example, an Fe atom has 26 electrons, while its valence electron configuration is $3d^6 4s^2$. Therefore, these 8 valence electrons in combination with electrons with 3p or 3s orbitals are sufficient to describe its bonding to neighboring atoms. As the number of electron reduces, the required number of electronic band is reduced, and hence the iterative diagonalization of Hamiltonian becomes efficient.

Another advantage of describing only valence electrons is that it avoids the description of core electron wave functions with wiggles. For example, a 2s electron wave function has 1 node, and a 3s electron has 2 nodes and corresponding wiggles. To describe the wiggles, the wave function should change fast in the real space, and it requires more basis. For atomic orbital basis, the basis of core electrons should be included, and for plane-wave basis, the wave with

small wavelength, or high kinetic energy should be included. These results in increased dimension of Hamiltonain matrix, and therefore avoiding description of core electrons is greatly efficient.

The description of valence electrons is achieved by using pseudopotentials, and nowadays projector augmented wave method by Blöch is widely used [57, 58]. The method employs a transformation $\mathscr{T}$ from a pseudo wave function $|\tilde{\Psi}\rangle$ to an all-electron wave function $|\Psi\rangle$:

$$|\Psi\rangle = \mathscr{T}|\tilde{\Psi}\rangle. \tag{2.24}$$

Outside an augmentation sphere Ω_R centered at a nucleus containing the core electrons and some of valence electrons, the pseudo wave function is identical to the all-electron wave function. Inside the region, while the all-electron wave function has wiggles, the pseudo wave function is expected to have less wiggles for computational efficiency. The all-electron wave function can be expanded partial waves ψ_i. A partial wave is a radial function multiplied by a spherical harmonics function. For an all-electron partial wave, we can consider a corresponding pseudo partial wave $\tilde{\psi}_i$. The pseudo partial waves is identical to the all-electron partial waves outside the augmentation region, and should form a complete set of functions in the augmentation region. The pseudo wave function can be expanded to pseudo partial waves:

$$|\tilde{\Psi}\rangle = \sum_i |\tilde{\psi}_i\rangle c_i \quad \text{within} \quad \Omega_R. \tag{2.25}$$

Similarly, the all electron wave function has also partial waves

$$|\Psi\rangle = \sum_i |\psi_i\rangle c_i \quad \text{within} \quad \Omega_R, \tag{2.26}$$

where the coefficients c_i are identical in both expansions. Then the all-electron wave function is expressed as

$$|\Psi\rangle = |\tilde{\Psi}\rangle - \sum_i |\tilde{\psi}_i\rangle c_i + \sum_i |\psi_i\rangle c_i. \tag{2.27}$$

We want the transformation $\mathscr{T}$ to be linear, therefore we consider some functions $|\tilde{p}_i\rangle$ called projector functions, such that

$$c_i = \langle \tilde{p}_i | \tilde{\Psi} \rangle. \tag{2.28}$$

We let the projector functions fulfill the conditions

$$\sum_i |\tilde{\phi}_i\rangle\langle\tilde{p}| = 1 \quad \text{within} \quad \Omega_R. \tag{2.29}$$

We find that the linear transformation is given as

$$\mathscr{T} = 1 + \sum_i (|\phi_i\rangle - |\tilde{\phi}_i\rangle)\langle\tilde{p}_i| \tag{2.30}$$

. Using this relationship, the expectation value of an observable by all-electron wave function can be expressed by using the pseudo wave functions. The wave functions can be obtained by variationally minimizing the total energy expressed by pseudo wave functions.

2.3 Local density approximation

Scuseria et al. described the development of exchange-correlation functional in-depth [59]. Pedagogical lectures are given by Burke [50]. A natural way of approximating the exchange-correlation functional $E_{\mathrm{xc}}[n(\mathbf{r})]$ in a solid system is considering a homogeneous electron gas, or the jellium model. A Slater determinant of plane-waves yields the exchange energy per electron as

$$\varepsilon_X(n) = 3\frac{k_F}{4\pi}. \tag{2.31}$$

It is more arduous to approximate the correlation energy. Ceperley and Alder performed the accurate quantum Monte Carlo calculation at several electron densities of jellium to obtain the correlation energy [60].

In practice, the local density approximation (LDA) is a huge success for describing realistic systems despite its simple approximation. The physics is that it holds the sum rules for the exchange-correlation holes, which has been considered for further developments of exchange-correlation functionals.

A spin-polarized system can be treated by considering the spin-scaling relation of single particle kinetic energy, and exchange functional, For correlation functional, there is a well-known parameterization of quantum Monte Carlo calculation.

2.4 Gradient generalized approximation

A real system is far from a homogeneous electron gas because it has high electron density near the nuclei, and a low density at the interstitial region. First attempts to incorporate the gradient of the electron density into the exchange-

correlation functional have been performed. The exchange-correlation energy is described as

$$E_{\mathrm{XC}}[n_\uparrow, n_\downarrow] = \int d\mathbf{r} n(\mathbf{r}) \varepsilon_{\mathrm{XC}}^{\mathrm{unif}} F_{\mathrm{XC}}(n_\uparrow, n_\downarrow, |\nabla n_\uparrow|, |\nabla n_\downarrow|), \tag{2.32}$$

where $\varepsilon_{\mathrm{XC}}^{\mathrm{unif}}$ is the exchange-correlation energy per electron in a homogeneous electron gas, and the deviation from the homogeneous gas is expressed as the exchange-correlation enhancement factor F_{XC}. These methods are called "gradient expansion approximation" and the perturbation of the electron density total energy at a varying electron density was used [61, 62]. These approximations were not consistently more accurate than the LDA. Later people realized the importance of the sum of exchange-correlation holes.

The gradient expansion approximation is improved by obeying exact rules such as sum rules of hole density in generalized-gradient approximation (GGA). The hole is the absence of a surrounding electron felt by an electron [50]. The hole is defined from the pair density

$$P(x,x') = N(N-1) \int dx_3 \cdots \int dx_N |\Psi(x,x',x_3,...,x_N)|^2, \tag{2.33}$$

where $x = (\mathbf{r}, \sigma)$. For a noninteracting system, the pair density will be simply

$$P(x,x') = n(x)n(x'). \tag{2.34}$$

However, the interaction between electrons modifies the previous equation,

$$P(x,x') = n(x)(n(x') + n_{\mathrm{XC}}(x,x')), \tag{2.35}$$

where the modifying term $n_{\mathrm{XC}}(x,x')$ is defined as the exchange-correlation hole. An exact property of the hole is that

$$\int dx' n_{\mathrm{XC}}(x,x') = -1, \tag{2.36}$$

meaning that two electrons are not usually located closely. To obey the sum rule of the holes, in the real space, the exchange hole is truncated at a cutoff distance to satisfy that the total amount of the exchange hole to be -1 in numerical GGA [63].

Perdew, Burke and Ernzerhof presented a simple formulation of the exchange-correlation energy [64], and this formulation is now widely used for solid systems. The formulation obeys the sum rule for the exchange-correlation hole. The functional employs a second-order gradient expansion at the limit of slowly varying density. In the rapidly varying limit, the correlation is vanished. The spin-scaling relationship is obeyed, and the Lieb-Oxford bound is respected. The resulting functional gives improved atomization energy over the LDA, and the bond length which is too short by the LDA increased.

2.5 Meta-generalized gradient approximation, SCAN

Although GGA by Perdew, Burke and Ernzerhof improves the atomization energy and bond lengths over LDA, the atomization energy has still errors of 10 kcal/mol, or 40 meV. [65]. The large deviation is attributed to failing to describe a one-electron system, or 'self-interaction error'. For a one-electron system, the Hartree energy is unnecessary because the sole electron does not interact with itself. However, the Hartree term it is nonzero, and should be can-

celed by the exchange-correlation energy. LDA fails to cancel because it is designed to describe a homogeneous electron gas, and GGA also because it is a modification of LDA. GGA can be improved by reducing the self-interaction error by considering an additional information, i.e. the kinetic energy density,

$$\tau_\sigma = \sum_i^{\text{occ.}} \frac{1}{2} |\nabla \psi_{i,\sigma}|^2, \tag{2.37}$$

where the sum is over occupied orbitals. τ_σ yields information on whether an electron density is composed of an orbital or many orbitals. Then appropriate correction can be made only for a region composed of nearly one orbital. A GGA using τ_σ is called meta-generalized gradient approximation (meta-GGA). Tao, Perdew, Staroverov, and Scuseria (TPSS) proposed a meta-GGA [66], and Sun et al. revised the meta-GGA and named it revTPSS [65].

Sun and Perdew et al. developed the strongly constrained and appropriately normed semilocal meta-GGA (SCAN) by holding more exact conditions than TPSS or revTPSS does [67,68]. The functional is strongly constrained in a sense that it obeys 17 exact constraints. For example, the exchange energy is nonnegative, it respects the spin-scaling relation, uniform-density scaling, fourth-order gradient expansion, and tight-bound for two-electron densities. The functional form has flexibility by adding free parameters that cannot be determined by the exact constraints. The functional is exact for not all but certain systems by adjusting the parameters and is called appropriately normed. Examples of the norms are for uniform and slowly-varying densities, the jellium surface energy, the H atom, and the He atom.

For describing the binding energy of hydrogen, SCAN is satisfactory compared to LDA or GGA since the mean absolute deviation of 22 weakly inter-

acting molecular complexes (S22) is reduced. The deviation is 2.3 kcal/mol for LDA, 2.8 kcal/mol for PBE, and 0.9 kcal/mol for SCAN (1 kcal/mol = 43.4 meV).

2.6 The exchange-correlation functionals for the van der Waals interaction of hydrogen molecules

In this section, we briefly review some functionals for the van der Waals correction. Then we explain why we relax the structure by PBE-D2 and obtain the binding energy by SCAN + rVV10 for efficient and accurate calculation of hydrogen binding energy in the subsequent chapters.

Van der Waals interaction (dispersion) is crucial for describing the physisorption of hydrogen molecules to backbone materials. Since hydrogen molecules do not chemically react, the interaction is weak and over the range of 50 to 200 meV. At this energy scale, the size of the correction of van der Waals interaction to the density functional theory is similar to the binding energy, and therefore is important. The hydrogen storage density may increase proportional to the Boltzmann factor,

$$\exp\left[\frac{|U|}{k_{\mathrm{B}}T}\right], \tag{2.38}$$

where $-|U|$ is the binding energy, k_{B} is the Boltzmann constant, and T is the absolute temperature. The deviation of the binding energy even by $1k_{\mathrm{B}}T$, or 26 meV at 300 K may increase of decrease the predicted storage density by exp[1], or 2.7. Therefore, estimating the hydrogen binding energy within 26 meV is a key technique for predicting the hydrogen storage density.

There are excellent reviews or benchmark tests on van der Waals [69], and

van der Walls for hydrogen storage [70–72].

The van der Waals interaction is a fluctuating dipole interaction, which is intrinsically nonlocal [48, 73]. We consider two atoms (1 and 2) whose distance is r. When the first atom has a transient dipole moment p_1, then the polarization of atom 2 is induced as

$$p_2 = \alpha E \approx \frac{\alpha p_1}{r^3}, \tag{2.39}$$

where α is the polarizability of the atom. The interaction energy of the two dipoles is

$$\frac{p_2 p_1}{r^3} \approx \frac{\alpha p_1^2}{r^6}. \tag{2.40}$$

Although the time average of a dipole moment at each atom is 0, the fluctuation give rises to the stabilization energy. This stabilization energy can be estimated by a simple system using the Schrödinger equation, also. The van der Waals energy depends on the fluctuation of two sites, and therefore it is nonlocal.

Due to the nonlocal nature of the van der Waals interaction, the local density approximation and semilocal gradient generalized approximation have difficulty in describing it accurately. Local density approximation largely overestimates the binding, and a widely-used gradient-generalized approximation by Perdew, Burke, and Ernzerhof [64] gives too weak binding for the physisorption of molecules.

2.6.1 Dispersion correction D2

Grimme presented a hugely popular semiempirical correction of the van der Waals interaction where by considering the distance r between atoms and the

coefficient of the $1/r^6$ term [74]. The total energy is corrected by

$$E_{\mathrm{DFT-D}} = E_{\mathrm{KS-DFT}} + E_{\mathrm{disp}}, \tag{2.41}$$

where the total energy from Kohn-Sham DFT formalism $E_{\mathrm{KS-DFT}}$ is augmented by an empirical dispersion correction term E_{disp}. The correction term is

$$E_{\mathrm{disp}} = -s_6 \sum_{i=1}^{N_{\mathrm{at}}-1} \sum_{j=i+1}^{N_{\mathrm{at}}} \frac{C_6^{ij}}{R_{ij}^6} f_{\mathrm{dmp}}(R_{ij}), \tag{2.42}$$

where R_{ij} is the distance between the i-th atom and the j-th atom, and C^{ij} is an atom pair i, j dependent dispersion coefficient, and s_6 is a global scaling factor for the exchange-correlation functional. Since the term $1/R_{ij}^6$ has singularity at $R_{ij} = 0$, the singularity is removed by multiplying the damping function f_{dmp}, where

$$f_{\mathrm{dmp}}(R_{ij}) = \frac{1}{1+\exp[-d(R_{ij}/R_r - 1)]}. \tag{2.43}$$

Here, d is an empirical parameter and set to $d = 20$. R_r is the sum of the predefined van der Waals radius of each atoms, which is set to the distance where the density of an atom drops to the $0.01a_0^{-3}$. The dispersion coefficient is approximated as the geometric mean of the coefficient for the same atoms,

$$C_6^{ij} = \sqrt{C_6^i C_6^j}. \tag{2.44}$$

Although the a dispersion coefficient for the same atom is obtained from the ionization potential and the static polarizability, the physical reason is not quite sound, and it might be regarded as an empirical fitting parameter.

The semiempirical approximation remarkably reproduces the van der Waals

interaction energy and binding distance. Grimme tested the functional for 40 test systems of non-covalently bound complexes, where the bonding of some of the systems are dominated by dispersion such as two benzenes, some are dominated by hydrogen bond, and the others are dominated by mixed dispersion and hydrogen bond. Using the exchange-correlation functional by Perdew, Burke and Ernzerhof in conjunction of Grimme's dispersion correction, the deviation of the energy of weak bonds was usually less than 30 meV, and was overestimated by only 10 to 20 meV in average. The advantage of this correction is computational efficiency compared to nonlocal functionals because only a term need to be calculated for each atom pairs. Grimme et al. improved the DFT-D2 correction by considering three-body van der Waals interaction and refining parameters, and named DFT-D3 [75]. They also changed the damping function to the form by Becke and Johnson and confirmed that a specific form of a damping function is more or less insignificant for van der Waals interaction [76].

For the relaxation of the binding energy of a hydrogen molecule, we utilized the exchange-correlation functional by Perdew, Burke, and Ernzerhof in conjunction with D2 dispersion correction (PBE-D2). The advantage of this combination is that it is very efficient compared to other van der Waals corrections, the geometry is correct, and the binding energy is reasonable.

2.6.2 Van der Waals density functional (vdW-DF)

Although the dispersion correction D2 by Grimme is efficient and reasonably accurate, its physical motivation needs further development, and the use of many empirical parameters for each atom makes it hard to predict when it works well and when it fails. It works well for some atoms with well-fitted param-

eters, but not for others with ill-fitted parameters. The group of Langreth and Lundqvist developed nonlocal exchange-correlation functionals by approximating exact formulas and thus they are more physically sound than the works of Grimme [77–79]. The exact correlation energy can be expressed in terms of density response to the full electric potential $\tilde{\chi}_\lambda$ and the interelectronic Coulomb potential V_λ using the adiabatic connection formula,

$$E_c = -\int_0^\infty \frac{du}{2\pi}\int_0^1 \frac{d\lambda}{\lambda}\mathrm{tr}[(1-\tilde{\chi}_\lambda V_\lambda)^{-1}\tilde{\chi}_\lambda V_\lambda - \tilde{\chi}_0 V_\lambda]. \tag{2.45}$$

Here, λ is a coupling constant. This formula can be approximated for long-range van der Waals interaction using the plasmon pole approximation for the inverse dielectric function, the authors and termed it van der Waals density functional, or vdW-DF:

$$E_c^{\mathrm{nl}}[n] = \int d^3r \int d^3r' n(\mathbf{r})\phi(\mathbf{r},\mathbf{r}')n(\mathbf{r}'). \tag{2.46}$$

Here, the kernel ϕ is a function of the distance $|\mathbf{r}-\mathbf{r}'|$, $n(\mathbf{r})$, and $\nabla n(\mathbf{r})$.

Kyuho Lee et al.[2] improved vdW-DF and proposed a second version (vdW-DF2) by replacing the Perdew-Burke-Ernzerhof (revPBE) exchange correlation functional with Perdew-Wang (PW86), because revPBE is too repulsive at equilibrium distance [80]. While vdW-DF models a solid system by describing an electron gas with slowly varying density, vdW-DF2 models the binding of two molecules with exponentially decaying tails by using a large-N asymptote for neutral atoms. The binding energy is significantly improved and the maximum error of the binding energy is only 70 meV underestimation of a H-bonded complex among the S22 duplexes.

[2]Kyuho Lee was a student of Prof. Jaejun Yu at Seoul National University.

I. Hamada proposed a variant of vdW-DF2 by adjusting the parameters of vdW-DF2 for the binding energy of molecular complexes and termed rev-vdW-DF2 [81, 82]. Although the binding energy of weakly bound molecules for the S22 set is improved, and the lattice constant for layered materials are enhanced, the interlayer interaction energy is compromised. This work also shows by using a plane-wave basis package VASP, that the maximum deviation of the binding energy of molecular duplex in the S22 data set is 40 meV underestimation.

For describing the hydrogen binding energy, we prefer Grimme's D2 method to vdW-DF2 or rev-vdW-DF2 because the D2 method is more than 2 times faster than vdW-DF2 which employs nonlocal integration, and the deviation is less.

2.6.3 A nonlocal vdW functional by Vydrov and Van Voorhis (VV10)

Vydrov and Van Voorhis proposed a nonlocal correlation energy functional VV10 for the van der Waal interaction, which is similar to the vdW-DF family of functionals [83]. This functional only uses the electron density, therefore the cost is considerably less than random phase approximation. The authors does not provide any derivation for the functional form, but they show that the functional reproduces binding energy and distance of weak and strong interactions simultaneously. The nonlocal correlation functional utilizes the local plasma frequency

$$\omega_p^2(\mathbf{r}) = \frac{4\pi n(\mathbf{r})e^2}{m} \tag{2.47}$$

and the local band gap given by

$$\omega_g^2(\mathbf{r}) = C\frac{\hbar^2}{m^2}\left|\frac{\nabla n(\mathbf{r})}{n(\mathbf{r})}\right|^4. \tag{2.48}$$

Here, C is adjusted for accurate asymptotic van der Waals C_6 coefficients. Since van der Waals is a fluctuating dipole interaction, the local plasma frequency and the local band gap may play important roles. Remarkably, the mean absolute deviation energy for weak interaction energy of the S22 test set is as small as 14 meV. Sabatini et al. revised the VV10 functional and proposed the rVV10 functional for efficient evaluation of the nonlocal correlation in a plane wave framework [84].

2.6.4 SCAN + rVV10

Although VV10 and rVV10 functionals are highly accurate for weakly interacting systems, it remains a question whether they are reliable for solid systems. Peng and Perdew et al. proposed a van der Waals functional SCAN + rVV10 by combining the meta-GGA SCAN and nonlocal correlation functional rVV10 [85]. SCAN is known to describe the solid accurately, SCAN + rVV10 may work for both weakly interacting solid and molecules. Peng et al. adjusted a parameter of rVV10 to be used with SCAN by fitting the binding curve of Ar. Thus SCAN + rVV10 is better than rVV10 for solids, and it describes the molecular systems as well as rVV10.

For efficiently evaluating the binding energy of a hydrogen molecule on a layer, first we relaxed the geometry by using PBE-D2, and then obtained the binding energy at the geometry by using SCAN + rVV10. This is because the geometry by PBE-D2 is reasonable, and the energy by SCAN + rVV10 seems to be more accurate. The computational load of SCAN + rVV10 is 13 times of PBE-D2 for a gibbsite layer since SCAN is a complex functional, and rVV10 requires nonlocal integrations. According to the comparison of the binding en-

ergy to an accurate CCSD(T) calculation, the real binding energy may be between those of PBE-D2 and SCAN + rVV10, and the binding energy seems to be closer to the value by SCAN + rVV10.

Chapter 3

The hydrogen storage mechanism of the magnesium amide ($Mg(NH_2)_2/LiH$) system

3.1 Introduction

Hydrogen is a promising environment-friendly energy carrier, but it is so bulky in its gas phase that how to increase the storage density is a crucial issue for practical applications such as hydrogen-fuel-cell-powered vehicles [1] [86, 87]. The currently-employed high-pressure compression at 70 MPa obviously poses a potential safety problem. An alternative method safer than the pressure vessel is to use complex hydrides such as Li–N–H [88–91], Li–Ca–N–H [92], Li–Cl–N–H [93], Li–Mg–N–H [94–100] systems, and B and N based hydrides [101].

As an alternative hydrogen storage material, Xiong *et al.* proposed magnesium amide, $Mg(NH_2)_2$ [102, 103] whose hydrogen storing (or releasing) reaction is as follows.

$$Mg(NH_2)_2 + 2LiH \leftrightarrow Li_2Mg(NH)_2 + 2H_2 \tag{3.1}$$

This system could in principle reversibly store 5.6 wt% of hydrogen. The system underwent ten cycles with little change in the desorption temperature [104].

[1] This chapter was published previously [34].

It was suggested that, at the molecular level, the negatively charged hydrogen (H^-) of LiH and the positively charged hydrogen ($H^{\delta+}$) of $Mg(NH_2)_2$ might attract each other electrostatically to form an intermediate phase. Then the H atoms from these reactants would be able to form H_2 [102, 105]. However, the reaction's activation energy was too high and the reaction required a high temperature, 186 °C, to reach the peak reaction rate [102]. It was necessary to reduce the temperature to make the hydrogen storage system commercially available. The activation energy was found to be reduced by the catalyses of V or V-based compounds [106], and $ZrFe_2$ [107]. Ru-doped carbon nanotubes also served as a catalyst [108]. When potassium was introduced in the form of KH, the activation barrier was reported to be reduced, the reaction temperature was substantially lowered to 132 °C [103], and the desorption rate was greatly enhanced [109]. K reduced the barrier by producing activated species [110]. However, little attention has been paid to the interaction of hydrogen with other atoms and the change of energy during the reaction. In the present study, we intend to explain the hydrogen storage and release mechanism for the Li–Mg–N–H system based on *ab initio* theoretical methods. We will investigate in detail the reaction of $Mg(NH_2)_2$ and LiH molecules with and without KH to clarify the reaction processes and the role played by KH, which has not been closely examined theoretically before.

3.2 Computational Methods

We carried out electronic structure calculations for molecular interactions based on the density functional theory (DFT) with the Perdew–Burke–Ernzerhof (PBE) exchange-correlation functional [44] using the Vienna *ab initio* simulation pack-

age (VASP) 5.4 [111]. We employed the projector-augmented wave (PAW) pseudopotential [58]. The energy cutoff for the plane-wave basis set was 750 eV, and the structure was relaxed until the force on each atom was less than 0.01 eV/Å. The size of the supercell was 16 Å$\times$ 15 Å$\times$ 14 Å, and the Γ point was used in the Brillouin zone sampling. The atomic configuration of the transition states was approximated through the nudged elastic band (NEB) method implemented in the VASP Transition State Tools [112]. Eight images of structures were chosen in the NEB method, and the one with the highest energy was identified as the transition state. The grid-based Bader charge analysis was used to determine the atomic charge [113].

3.3 Results and Discussion

3.3.1 H_2-releasing reaction of $Mg(NH_2)_2$ and LiH

We first consider an intermolecular (gas-phase) reaction of $Mg(NH_2)_2$ and LiH without KH. We examine the reaction of releasing one H_2 molecule in detail, and then the more advanced reaction of releasing two H_2 molecules will be described rather briefly. The release of a single H_2 molecule is expressed in the following equation.

$$Mg(NH_2)_2 + LiH \leftrightarrow LiMgN_2H_3 + H_2 \tag{3.2}$$

Optimized geometries of the molecules involved in the reaction are summarized in Fig. 3.1, and the corresponding energy diagram is illustrated in Fig. 3.2. Computed bond lengths are presented in Fig. 3.1 and they agree with experimental values for known cases indicated in Fig. 3.1(a). As $Mg(NH_2)_2$ and LiH begin

to react, an intermediate complex (Int-1), $Mg(NH_2)_2$–LiH is formed. The intermediate is stabilized by the electrostatic interaction among Mg^{2+}, N_a^-, Li^+, and H_a^-, where the subscript indicates a particular atom shown in Fig. 3.1(a). Calculated Bader charges are $1.59e$ for Mg, $-1.51e$ for N_a, $0.89e$ for Li, and $-0.80e$ for H_a, respectively. As charged atoms in the reactants bond together, a fraction of electrons of the neighboring bonds moves to new bonds. Consequently, the Li–H_a and Mg–N_a bonds are elongated. This phenomenon agrees with a previous calculation of the reaction of similar molecules [89]. This reaction step is exothermic and the formation of the Int-1 releases 235.1 kJ/mol of energy (the first step in Fig. 3.2), which is relatively large because two bonds are formed.

Starting from the Int-1, the motion of the hydrogen atoms leads to the formation of a transition state. The energy pathway releasing a hydrogen molecule obtained from the NEB calculation is presented in Fig. 3.3. A hydrogen atom (H_a) of LiH and another hydrogen atom (H_b) of the NH_2 group approach each other to form a weak elongated bond (0.791 Å), and are weakly bound to Li. The motion of the two H atoms is facilitated by their electrostatic interaction in the Int-1 [102]; Bader charges of H_a and H_b are $-0.80e$ and $0.34e$, respectively. Meanwhile, the bonds of the Int-1 (Mg–H_a and N_a–H_b) are broken, as indicated by their atomic separation. A fraction of the electrons of these bonds moves to remaining bonds of N_a (N_a–Mg, N_a–Li), and the bonds are shortened. These changes of bonds absorb 191.3 kJ/mol. This process absorbs a large amount of energy because the broken bonds (Mg–H_a and N_a–H_b) are ionic and strong, but the newly generated bonds (H_a–H_b, Li–H_aH_b) are neutral and relatively weak.

As the two hydrogen atoms (H_a, H_b) move to a more stable position, a second intermediate complex, $LiMgN_2H_3$–H_2 (Int-2), is formed. Here, H_2 weakly

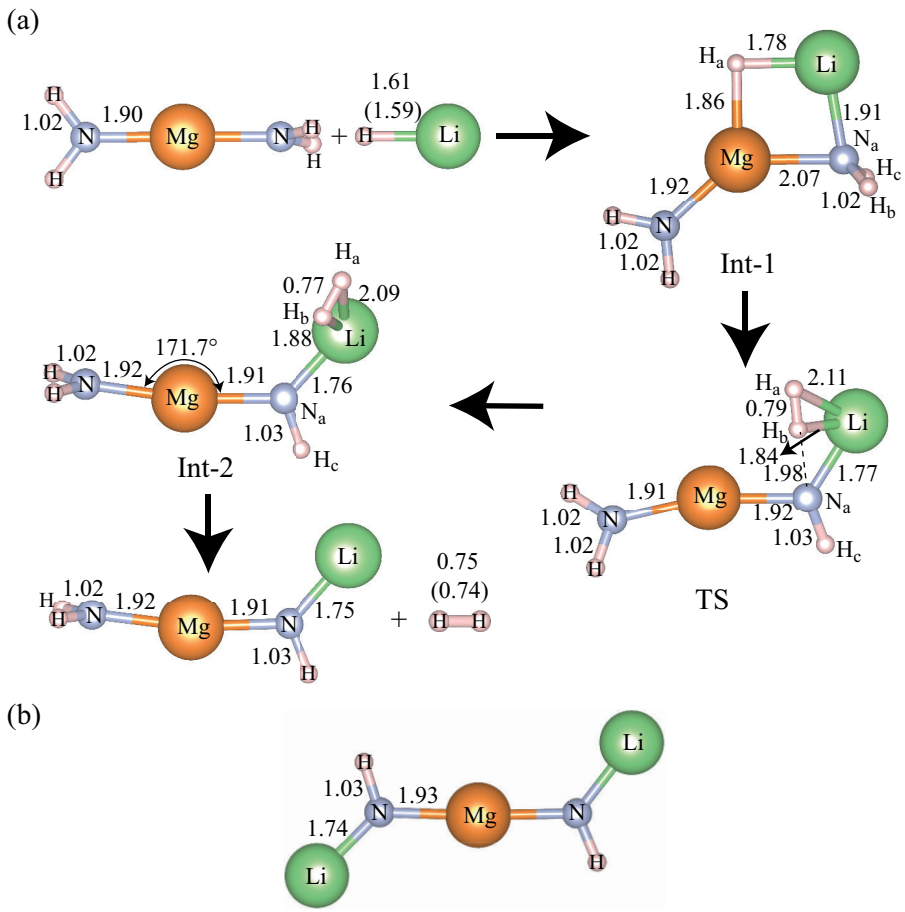

Figure 3.1: (a) Optimized structures of the reactants, the intermediate complexes (Int-1, 2), the transition state (TS), and the products of the reaction of releasing a hydrogen molecule (Eq. (3.2)). (b) The optimized structure of the product of the more advanced reaction of releasing two hydrogen molecules (Eq. (3.1)). The bond lengths are in Å. Some experimental bond lengths are presented in parentheses for comparison [4].

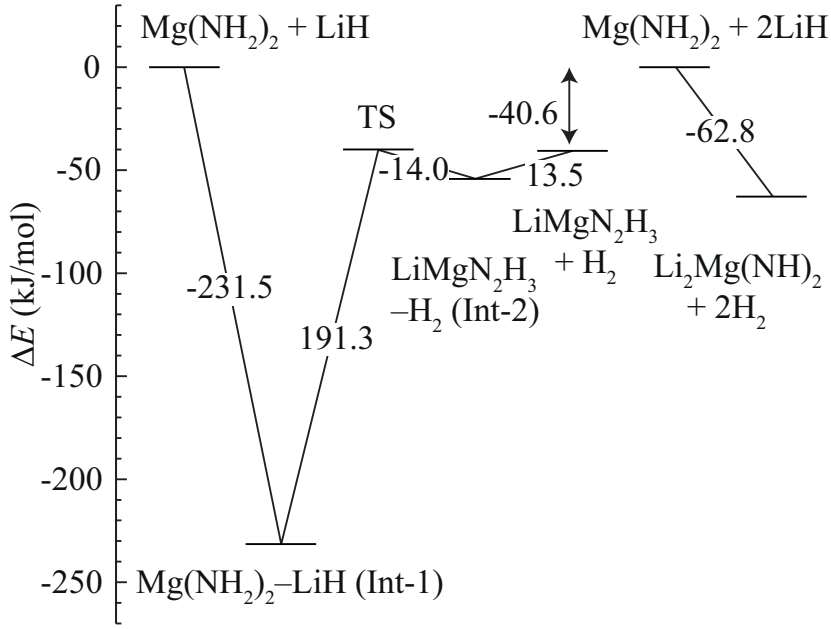

Figure 3.2: Energy diagram of the dehydrogenation reactions (Eqs. (3.1), (3.2)). (96.5 kJ/mol = 1 eV)

bonds to Li and this step releases 14.0 kJ/mol. Then H_2 is liberated, completing the reaction described by Eq. (3.2). The overall reaction is exothermic by 40.6 kJ/mol.

The release of another H_2 molecule by the reaction with one more LiH molecule (Eq. (3.1)) is similar to the previous reaction. Li of the second LiH molecule bonds to the remaining NH_2 group. Then a H atom of LiH and another H atom of the NH_2 group approach each other to form a H_2 molecule. The H_2 molecule is liberated, leaving $Li_2Mg(NH)_2$ behind (Fig. 3.1(b)). The overall reaction is exothermic, and releases 62.8 kJ/mol (Fig. 3.2). A more energy is released than the previous reaction implying that the generation of the second H_2 molecule is also exothermic.

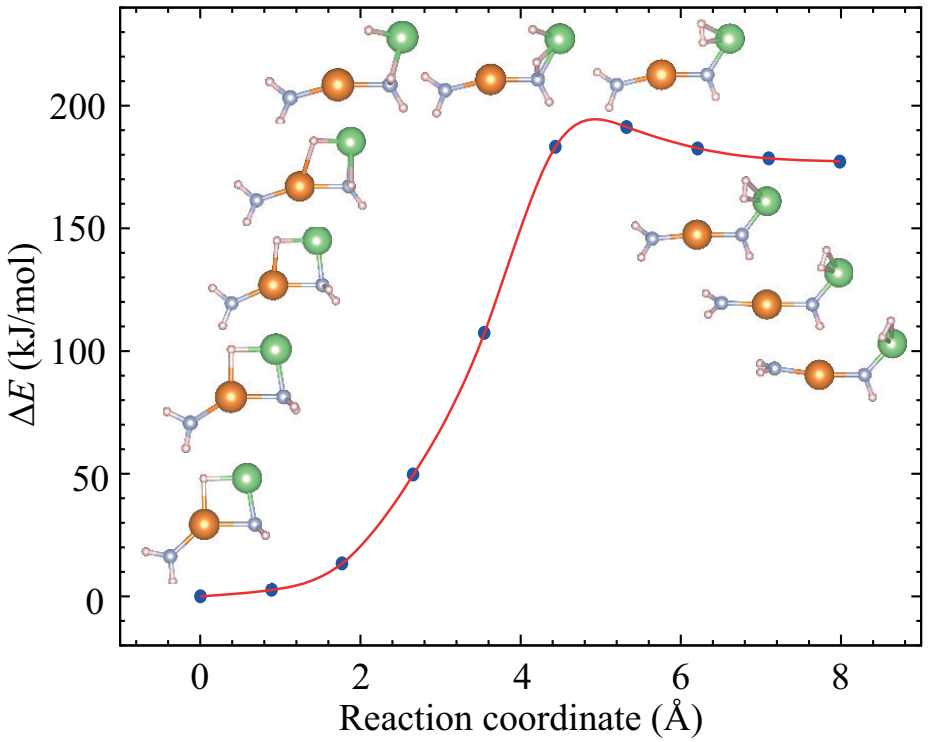

Figure 3.3: Minimum energy path (intrinsic reaction coordinate) of the reaction of releasing a hydrogen molecule (Eq. (3.2)).

3.3.2 The effect of KH

Next, we consider the effect of KH on this system. In experiment [103], a small amount of added KH (3 mol%) is known to act as a catalyst. Here, we consider the following reaction.

$$\mathrm{Mg(NH_2)_2KH + LiH \leftrightarrow LiKMgN_2H_4 + H_2} \tag{3.3}$$

The optimized geometries of the molecules involved in the reaction process are summarized in Fig. 3.4 and the corresponding energy diagram is presented in Fig. 3.5. When KH is added to $\mathrm{Mg(NH_2)_2}$, the H atom of KH bonds to Mg, and

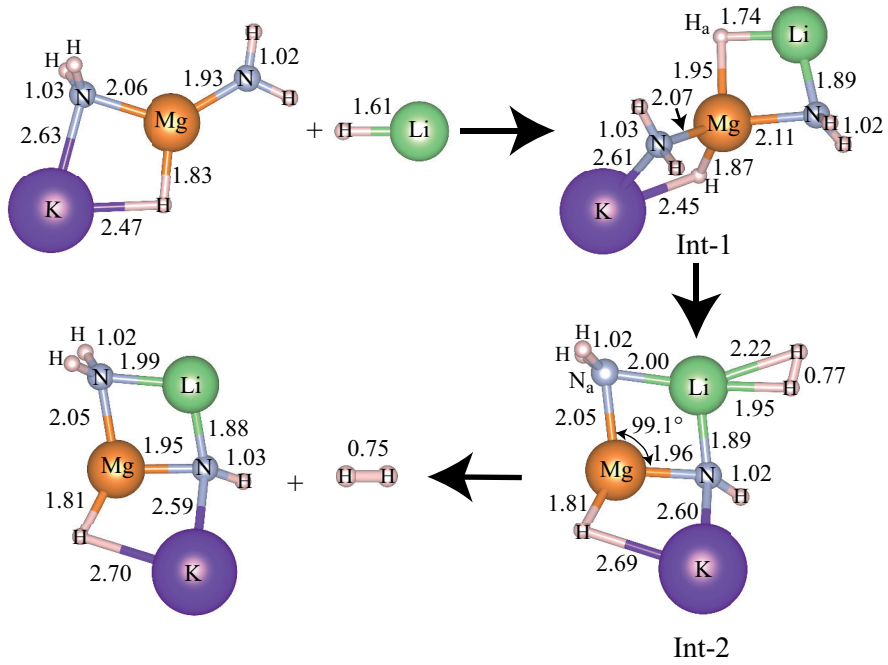

Figure 3.4: Optimized structures of the reactants, the intermediate complexes (Int-1, 2), and the products of a reaction removing a hydrogen molecule from magnesium amide with potassium hydride (Eq. (3.3)). The bond lengths are in Å.

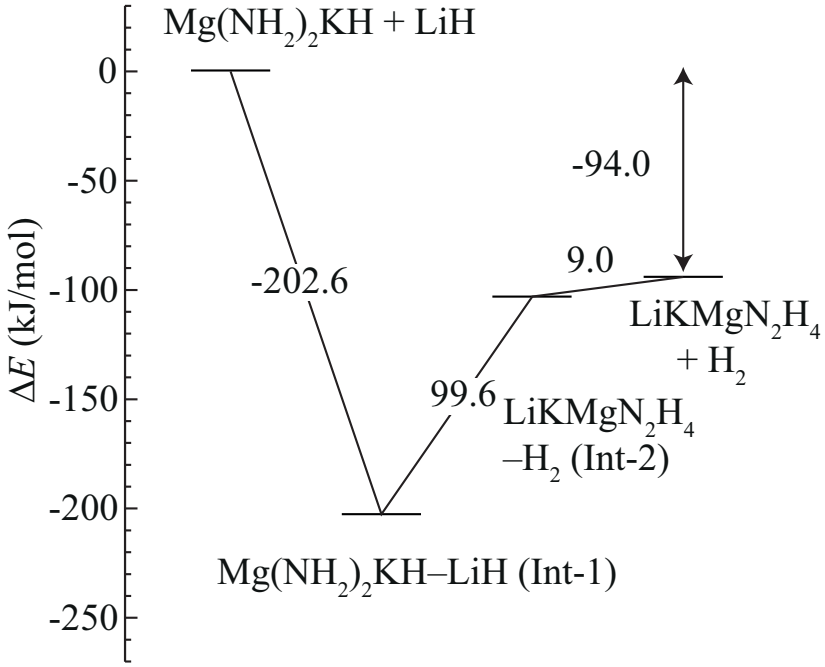

Figure 3.5: Energy diagram of the dehydrogenation reaction of magnesium amide with potassium hydride (Eq. (3.3)).

the coordination number of Mg increases from two to three. As LiH bonds to $Mg(NH_2)_2KH$ and an intermediate complex is formed (Int-1), two new bonds are formed, and the Int-1 is substantially stabilized (Fig. 3.5). This step releases 202.6 kJ/mol, slightly less than the case where KH is absent.

The second intermediate complex (Int-2 in Fig. 3.4) is stabilized by the bond of Li and N_a, which is facilitated by KH. The H atom (H_a) bonded to Li and the H atom bonded to N form the H_2 molecule, weakly interacting with Li. In the case without KH, Li bonds to one N only (Fig. 3.1). On the other hand, when KH is present, H of KH bonds to Mg and Mg's coordination number increases from two to three as mentioned above, and the N–Mg–N angle decreases from 171.7° to 99.1°. Then Li easily bonds to two N atoms. This step absorbs 99.6 kJ/mol

which is much smaller than the case without KH. As the hydrogen molecule is liberated, the reaction in Eq. (3.3) is completed. The interaction between H_2 and Li in the removing process (Int-2) is weak as indicated by the long bond lengths of Li and H_2 (1.95, 2.22 Å) in Fig. 3.4. This step absorbs 9.0 kJ/mol. The overall energy lowering is -94.0 kJ/mol, much lower than the case where KH is absent (-40.6 kJ/mol). This lowering is ascribed to the stabilization of the Int-2 by KH.

If the gas-phase structures of the molecular units introduced above do not change appreciably in their solid-state counterparts, a reaction mechanism similar to the one described above is expected to operate in the solid phase. (Note that the actual experiment is carried out with the ball-milled solid-phase environment.) There exist both similarities and differences between two phases. For example, one of the reactants $Mg(NH_2)_2$ has an amide group, $–NH_2$ in both phases [114–116]. Also, in both gas and solid structures, N bonds to Mg. However, a Mg atom bonds to two N atoms and a N atom bonds to one Mg atom in the gas phase, while a Mg atom bonds to four N atoms and a N atom usually bonds to two Mg atoms in the solid phase. In both gas and solid phases of $Li_2Mg(NH)_2$, N bonds to N only, and Li bonds to N only, and Mg to N only. However, the number of bonds differ between two phases. In the solid-phase reaction, the activation energy is 102 kJ/mol, and the reaction energy is 44.1 kJ/(mol H_2) (endothermic) [102]. The energy difference in different phases is attributed to the heat of vaporization and other structural differences. In any case, since the chemical reaction always occurs at the surface of solid particles, future works should focus on the effect of solid surface structures on the reaction mechanism for a more accurate analysis.

3.4 Conclusions

The hydrogen storage and release reactions of the gas-phase Li–Mg–N–H system have been investigated. The intermediates and the transition states for the reaction between $Mg(NH_2)_2$ and LiH have been identified through the electronic structure calculations based on the density functional theory. The hydrogen releasing reaction is found to be exothermic. When KH is added to the gas-phase system, the reaction energy is lowered. This work shows a detailed dehydrogenation mechanism of the Li–Mg–N–H system, and helps to design new catalysts to further lower the reaction temperature.

Chapter 4

Hydrogen storage in intercalated gibbsite

4.1 Introduction

The storage of hydrogen (H_2) is a significant issue for practical applications such as hydrogen fuel-cell driven vehicles [12]. Storage of H_2 in gas-phase in the potential well of layered materials is advantageous because it utilizes weak interaction [41] and the storage or desorption of H_2 does not require high temperature. Previously, the storage of H_2 in potential well was studied by using pillared or intercalated graphene [43, 117–120], and metal organic frameworks [121,122]. We and our coworkers stored 4.65 wt% of H_2 in K-intercalated mesoporous graphene oxide experimentally [29] and analyzed the system theoretically [29, 42]. In the experiment, the mass of graphene oxide sample was 50 μg, and when the mass increased and the sample was pelletized, the storage density did not increase linearly as expected. The structure of the mesoporous graphite oxide has some degree of uncertainty, and the engineering of its structure is thus somewhat limited. Although the X-ray diffraction pattern shows a peak corresponding to the interlayer spacing, the intensity of the peak decreased much during treatments. The activation by KOH makes holes and bends the graphene plane.

In this study, we propose intercalated aluminum hydroxide ($Al(OH)_3$, gibb-

site) as a competitive hydrogen storage material that provides a potential well between layers. Compared to the KOH activation used in mesoporous graphite oxide, the intercalation is a weaker treatment using a lower temperature. We can know the atomic structure of intercalate aluminum hydroxide better, and analyze, predict and engineer its H_2 storage in more detail. Aluminum hydroxide is a layered material with ample hydroxyl groups (OH^-) that have charge and attract H_2. This material consists of light elements, and therefore the weight ratio of stored hydrogen to gibbsite could be high. We studied the intercalation of $NiSO_4$ (nickel sulfate) and $Ni(COO)_2$ (nickel oxalate) Firstly, sulfate and oxalate ions are large so that they can increase the spacing between the layers. Secondly, the charged group of ${SO_4}^{2-}$ is known to attract H_2 strongly by polarization [123], and ${(COO)_2}^{2-}$ would work similarly. The capacity of hydrogen storage in intercalated gibbsite is estimated by calculating the potential well depth using the density functional theory, and the grand canonical Monte Carlo simulation on the equilibrium.

4.2 Computational Methods

Total energy and structure are calculated by using electronic structure calculations based on the density functional theory (DFT). We employed the projector augmented-wave pseudopotential [124] as implemented in the Vienna *ab initio* simulation package (VASP) 5.4 [125].

We performed the nudged elastic band calculation to find the minimum energy path and the energy barrier of the entrance of Li cation. The structure of the transition state was accurately obtained by the climbing image method [126] implemented in the Transition State Tools for the VASP package. To perform

the nudged elastic band calculation, atoms far from the vacant site, where the Li cation enters, were fixed. The effect of fixing on the energy of final configuration was 0.1 eV and negligible. The height of the barrier was estimated by using a more accurate local Minnesota functional developed in 2006 (M06-L) [127].

To obtain accurate binding energy of H_2 to layered materials, first, the relaxed structure was obtained by using an exchange-correlation functional by Perdew, Burke, and Ernzerhof (PBE) [64] and the van der Waals interaction correction D2 by Grimme, [74]. The structure was relaxed until the force on each atom was less than 0.02 eV/Å. Second, using the structure, the binding energy was obtained by the strongly constrained and appropriately normed (SCAN) meta-generalized gradient approximation to the functional [67] with the revised Vydrov-van Voorhis (*r*VV10) nonlocal correlation functional [85]. The kinetic energy cutoff for the plane-wave basis set was 520 eV for cell relaxation and otherwise 400 eV. The Γ-point was used for sampling the Brillouin zone. The ferromagnetic configuration for Ni (2.000 bohr for a Ni atom) is 1 eV/Ni stable than nonmagnetic one, and the ferromagnetism opens a gap. The ferromagnetic configuration was used. The binding energy of an n-th H_2 molecule to an intercalated-gibbsite was calculated cumulatively by $\Delta E = E[\text{backbone} - (H_2)_n] - E[\text{backbone} - (H_2)_{n-1}] - E[H_2]$.

The storage capacity of H_2 at a finite temperature is obtained by using the grand canonical Monte Carlo simulation [42, 128]. The interaction energy of a H_2 molecule to NiOxalate-intercalated gibbsite at an arbitrary point in space is linearly interpolated from the binding energy at grid points by density functional theory. The linear interpolation was performed by using the BSPLINE-FORTRAN package v.5.4.0 [129]. The Monte Carlo simulation was performed by a home-

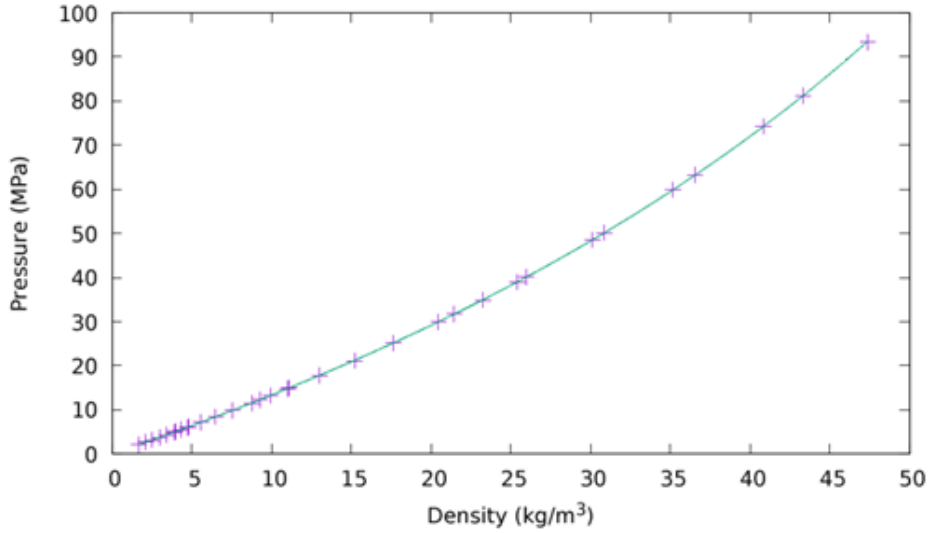

Figure 4.1: The fitting of the equation of state of H_2 gas at 25°C [5] to the van der Waals equation of state.

made Fortran and python code.

4.3 Results and Discussion

4.3.1 Potential well depth required to store H_2

A moderate potential well of around -100 meV can significantly increase the density of hydrogen. We set the target storage density of H_2 to be that of pressure vessels in commercial vehicles with 700 atm. We obtained the depth of potential well required to reproduce the same density.

First, we fitted the van der Waals equation of state to a measured pressure and density of H_2 at 25°C [5] (Fig. 4.3.1). As we aim for describing H_2 storage at the room temperature, the temperature for the equation of state was 25°C.

The range of pressure was up to 90 MPa since we compare a pressure vessel of 70 MPa. The van der Waals equation of state follows:

$$\left(P + \frac{a}{v^2}\right)(v - b) = kT, \tag{4.1}$$

where $v = N/V$, N is the number of molecules, V is the volume, k is the Boltzmann constant, and T is the absolute temperature. The physical meanings of the parameters a and b are

$$a = \frac{2\pi r_0^3 u_0}{3}, \tag{4.2}$$

$$b = \frac{2\pi r_0^3}{3}. \tag{4.3}$$

Here, r_0 is the radius of the minimum distance between molecules, and $-u_0$ is the maximum depth of the attractive potential proportional to $-r^6$ when $r = r_0$. We obtained $a = 7.50 \times 10^{-51}$ m^3 J, $b = 2.74 \times 10^{-29}$ m^3, $r_0 = 2.36$ Å, and $u_0 = 1.71$ meV. The asymptotic standard errors were 8.58 % for a and 0.25 % for b. The quality of the fitting is good as shown by small $\sqrt{\mathrm{WSSR}/\mathrm{NDF}} = 0.0402365$, where WSSR is the weighted sum of squared residuals, and NDF is the number of degrees of freedom. Lide et al. reported the coefficients of the van der Waals gas as $a = 6.76 \times 10^{-50}$ m^3 J, and $b = 4.40 \times 10^{-29}$ m^3 [4]. These parameters are derived from the triple point of H_2, consequently they differ from the parameters of our fitting. Our fitting is to describe H_2 at the room temperature in the pressure range of 1–90 MPa.

Second, using the formula of chemical potential for the van de Waals gas, the potential well depth required to reproduce the density is obtained in Table 4.1 as function of volume fraction of backbone. The well depth is calculated

Table 4.1: The potential well required to store hydrogen

Volume fraction of backbone	Outside pressure (atm)					
	10	30	50	70	100	180
0	-121	-92	-79	-70	-60	-44
0.3	-145	-116	-103	-94	-84	-68
0.4	-161	-132	-119	-110	-100	-84
0.5	-189	-160	-147	-138	-128	-112

by the following procedure. The target density of H_2 in a 700.0 atm high pressure vessel is $39.59\,\mathrm{kg/m^3}$. The chemical potential $\mu_{\mathrm{H2-H2}}$ of the gas inside the potential well from the interaction between the H_2 gas molecules is the same as the chemical potential corresponding to the density [130] outside the well, and is given by

$$\mu_{\mathrm{H2-H2}} = \frac{kT}{1-nb} - 2na - kT\left\{\log\left[\frac{n_Q}{n}(1-nb)\right]+1\right\}, \tag{4.4}$$

where $n = N/V$ is the number density, and the quantum density n_Q is given by

$$n_Q = \left(\frac{MkT}{2\pi\hbar^2}\right)^{3/2}. \tag{4.5}$$

For H_2 in a 700.0 atm vessel, $\mu_{\mathrm{H2-H2}} = -0.1189$ eV. From the given outside pressure, outside density n is obtained by using the van der Waals equation of state (Eq. 4.1). Then the chemical density μ_{out} corresponding to the outside density n is calculated. Now the potential well depth U is required to change the chemical potential μ_{H2-H2} inside the vessel, so that the inside gas is in

Table 4.2: The effect of calculation method on the binding energy (ΔE) of H_2 on and perpendicular to benzene. The equilibrium distance is d.

Method	ΔE (meV)	d (Å)	Reference
CCSD(T)	-41.5	3.2	[71]
PBE-D2	-56.5	3.0	[71]
	-56.1	3.07	This work
SCAN + rVV10	-37.5	3.08	This work

equilibrium with the outside gas:

$$\mu_{\mathrm{H2-H2}} + U = \mu_{\mathrm{out}}. \tag{4.6}$$

From the above equation, U is calculated. Using the above calculation, for example, when the backbone is absent in an ideal case, and the pressure outside the potential well is 30 atm, potential well of -92 meV can reproduce the density of H_2 in a 700 atm vessel. Because the density of pressure significantly reduced, the system becomes more safer. In practice, the potential well comes from the interaction with backbone material. Therefore, when the volume fraction of backbone is 0.5, and the outside pressure is 100 atm, the potential well of -128 meV can store the same density of H_2. Still this is a huge improvement of safety over the compression vessel.

4.3.2 Test of functionals of density functional theory for H_2 storage system

A benchmark test of functionals on the binding energy of H_2 to benzene is shown in Table 4.2. The H_2 molecule lies in the line perpendicular to the benzene plane, and the line passes the center of benzene. The binding energy by

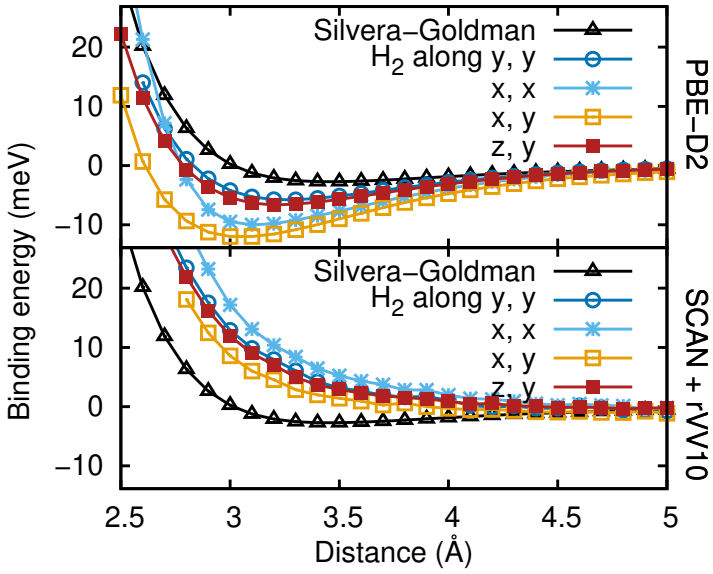

Figure 4.2: The energy of binding between two H_2 molecules, where one is at the origin, and the other is at $(r,0,0)$, where r is the distance between the molecules. Two functionals are used, and are compared to Silvera-Goldman potential from experiment.

CCSD(T) is regarded to be close to an experimental value and the deviation is usually less than 10 %. PBE-D2 and SCAN + rVV10 produce binding energy close to the CCSD(T) value, where PBE-D2 predicts stronger binding, and SCAN + rVV10 weaker binding. The binding distances are close to CCSD(T) values. From now on, to save the time, we calculate the structure by using PBE-D2, and calculate the binding energy at the geometry by using PBE-D2 and SCAN + rVV10.

Figure 4.2 shows the ability of functionals to reproduce the energy of binding between two H_2 molecules. One molecule is at the origin, and the other is at $(r,0,0)$. Two functionals are used, and are compared to Silvera-Goldman potential from experiment. Compared to the Silvera-Goldman potential, PBE-D2 predicts stronger binding, and SCAN + rVV10 unbinding. Therefore, the

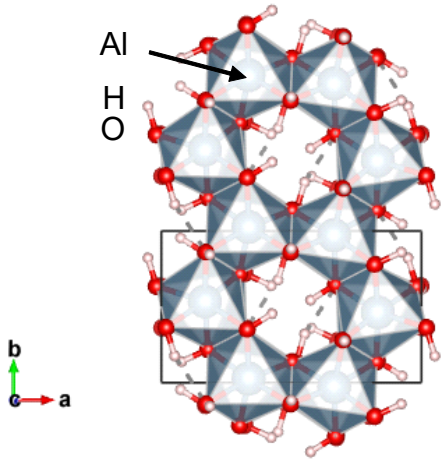

Figure 4.3: The structure of a gibbsite layer. The rectangle denotes the unit cell.

Table 4.3: The effect of functional on the binding energy of H_2 to a single layer gibbsite

	Local functional	Nonlocal vdW functional
Functional	PBE	PBE - D2
ΔE (meV)	-33	-120
Functional	SCAN	SCAN + rVV10
ΔE (meV)	-60	-82

experimental value lies between PBE-D2 and SCAN + rVV10 values.

4.3.3 The binding of H_2 to gibbsite

When H_2 binds to a gibbsite layer, the van der Waals interaction contributes the binding energy significantly. Figure 4.3 shows the structure of a gibbsite ($Al(OH)_3$) layer. An Al atom is surrounded by the octahedron of 6 O atoms, and an O atom is connected to a H atom. The octahedrons form a distorted honeycomb lattice. Figure 4.4 shows the structure of H_2 bound to a gibbsite layer. The

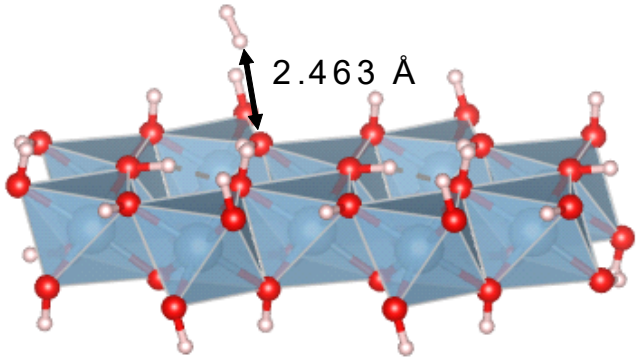

Figure 4.4: The binding of H_2 to a gibbsite layer

binding energy is evaluated using various functionals in Table 4.3 at the structure optimized by PBE-D2. Using a local PBE functional, the binding energy is as small as -33 meV, but when the van der Waals interaction was corrected empirically by using PBE-D2, the binding energy increased to -120 meV. Similarly, when a nonlocal rVV10 correlation functional was used in conjunction with local SCAN functional, the binding increased significantly. The van der Waals interaction is significant in the binding of H_2 to a gibbsite. The binding energy by SCAN + rVV10 is expected to be closer to an experimental one since this functional is more accurate.

Figure 4.3.3 shows that the orientation of a H_2 molecule seems to be parallel to the electric field generated by the lone pairs of oxygen in gibbsite. In Fig. 4.3.3(c), the lone pair electrons of O is electrically negative and has positive (repulsive) local potential. The dash represents the boundary of region that can be accessed by H_2 due to ion core repulsion from exchange and correlation. The boundary is an envelop of region (blue) near the cores. The region with positive local potential coincides with the position lone pair electrons of hydroxyl groups parallel to the gibbsite plane (Fig. 4.3.3), and therefore a H_2 molecule

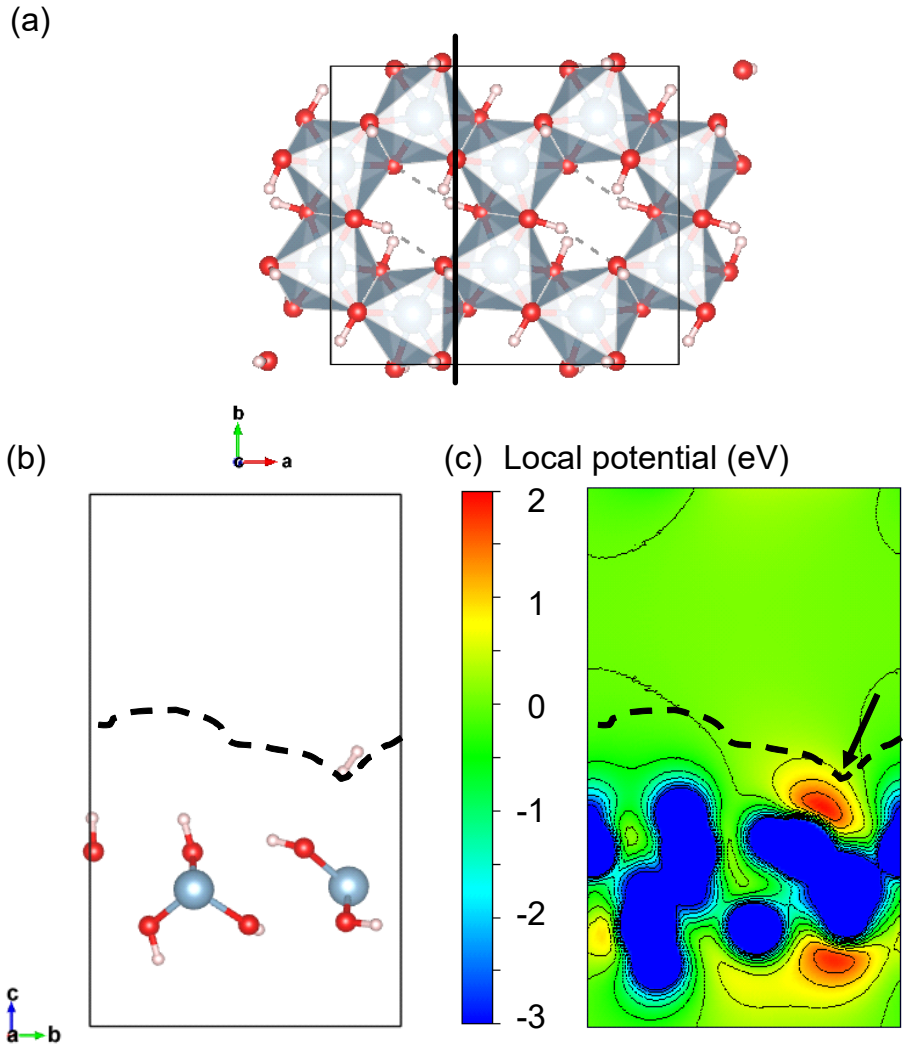

Figure 4.5: The local potential of gibbsite showing that the direction of a H_2 molecule is related to the equipotential lines, or the electric field generated by the lone pair electrons of oxygen. (a) Structure of a gibbsite with a line showing the position of cross section in (b) and (c). (b) Cross sectional view of gibbsite and bound H_2. The dashed line indicates a rough envelope of atoms. (c) The local potential of gibbsite without H_2. The arrow shows the position of bound H_2 if it is present.

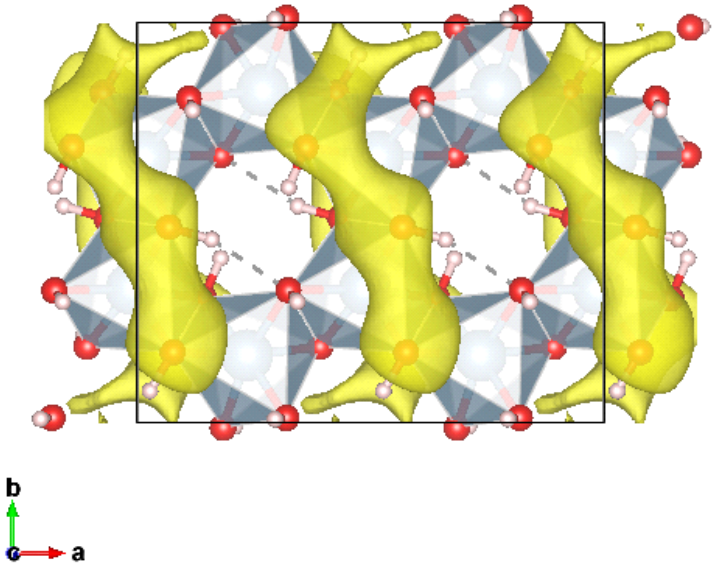

Figure 4.6: The isosurface of local potential showing the lone pair electrons of gibbsite. The level of isosurface is 0.7 eV relative to the vacuum.

binds to the lone pair of oxygen.

The electric polarization contributes to the binding of H_2 to gibbsite. The electric field is obtained from the gradient of the local potential. The stabilization energy by polarization is given by,

$$U_{\mathrm{p}} = -\frac{1}{2}\alpha_{\parallel}E_{\parallel}^2 - \alpha_{\perp}E_{\perp}^2, \tag{4.7}$$

where α is the polarizability, and E is the electric field. The subscript $\parallel$ denotes that the direction is parallel to the axis of a H_2 molecule, and $\perp$ denotes the perpendicular direction. We use the values of α's obtained by Rychlewski by a perturbation calculation: $\alpha_{\parallel} = 6.39e^2a_0^2/E_h$, and $\alpha_{\perp} = 4.59e^2a_0^2/E_h$ [131]. The strength of the electric field where H_2 binds is 0.57 V/Å, $E_{\parallel} = 0.41$ V/Å, $E_{\perp} = 0.41$ V/Å, which means that the direction of a H_2 molecule is not exactly

parallel to the electric field, but is somewhat related. The resulting $U_{\mathrm{p}} = -13.2$ meV, which contributes to the total binding energy.

4.3.4 An intercalated cation is in the center of hexagon of gibbsite

To calculate the binding energy of H_2 molecule to an intercalated gibbsite, the structure of the intercalated gibbsite should be known. When $LiSO_4$ is intercalated in gibbsite, the Li cation will be first positioned in the center of the Al hexagon of gibbsite, and not between layers. This is because when LiCl is intercalated in gibbsite, the Li cation moves to the empty site at the center of the Al hexagon [132, 133]. However, the empty site is covered by OH groups, and therefore the entrance of Li may be hampered.

Here, we show that the OH groups easily open to allow the entrance of Li cation at the room temperature by finding the minimum energy path of Li entrance. Figure 4.7 shows the minimum energy path, where the first barrier height is as low as 0.22 eV obtained by the PBE functional, and still 0.40 eV by the M06-L functional which gives a more accurate barrier height.

A crude estimate of the reaction rate of entrance of Li indicates that a Li atom easily enters the vacant site. According to the transition state theory, the reaction rate k_r is given by

$$k_r = \frac{\kappa kT}{h} \exp\left[\frac{-\Delta G}{kT}\right], \tag{4.8}$$

where ΔG is the barrier height, and κ is the transmission coefficient ranging from 0 to 1. For this reaction, assuming that $\kappa = 1$, we obtain $k_r = 1.3 \times 10^6\ \mathrm{s}^{-1}$, and as a result, the entrance of a Li ion occurs fast. Similarly, other cations

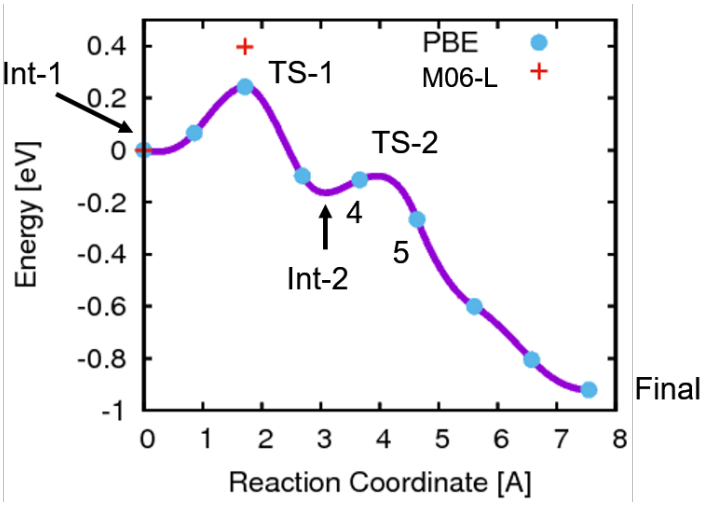

Figure 4.7: The minimum energy path for the entrance of a Li ion in a gibbsite layer. PBE: using the exchange-correlation functional by Perdew, Burke, and Ernzerhof; M06-L: using a local Minnesota functional developed in 2006; Int-1: the first intermediate; and TS-1: the first transition state. The energy of the first transition state (TS-1) is evaluated by the functional M06-L which gives a more accurate barrier height.

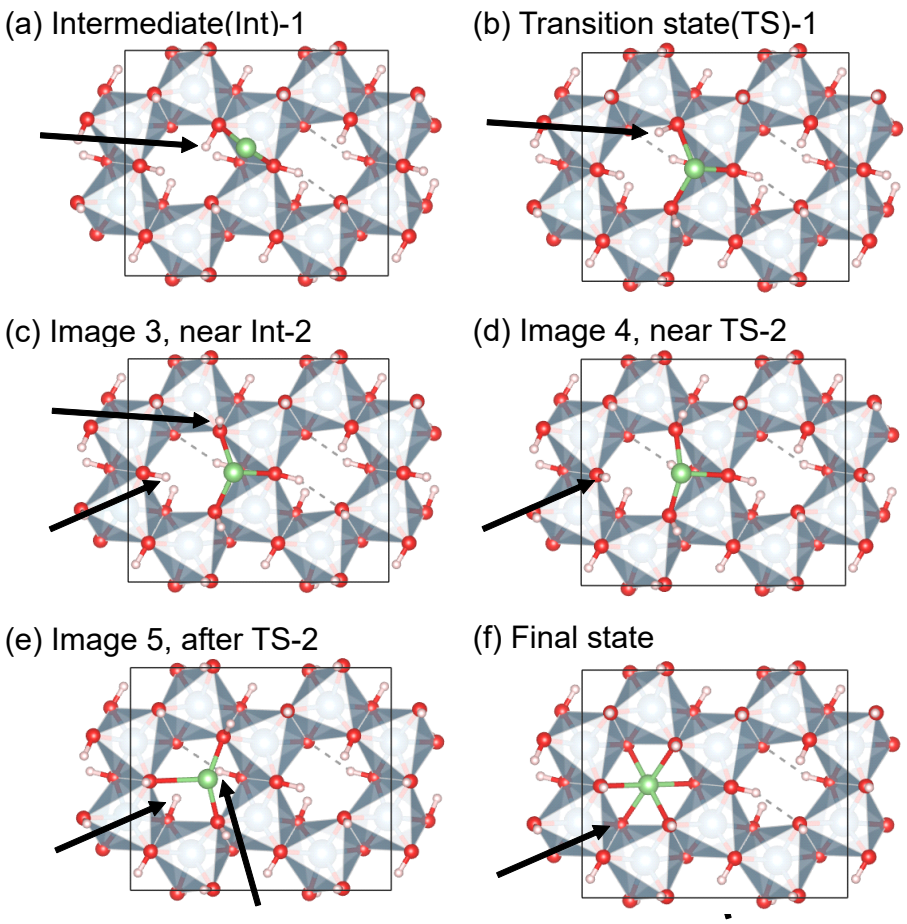

Figure 4.8: The intermediate states, a transition state, and final intermediate state during the entrance of a Li ion in a gibbsite layer. Arrows denote the opening of OH groups covering the vacant Al site, which enables the entrance of the Li ion.

such as Ni that is considered later will enter the vacant site easily at the room temperature.

4.3.5 The binding of H_2 to intercalated gibbsite

$NiSO_4$-intercalated gibbsite can accommodate a layer of H_2 molecules, where the interlayer is relaxed (Fig. 4.9). Note that a gibbsite unitcell contains two $Al(OH)_3$ layers, and we focus on the space between top and middle layers. The interlayer spacing is relaxed to 9.23 Å, and then approximately a layer of H_2 can reside in the potential wells. Also, H_2 molecules point to charged O because polarization along the axis of H_2 molecule increases binding. The potential well is deep because a H_2 molecule interacts with the upper and lower gibbsite layers and SO_4, which will result in a large storage density. Ni is in the center of six Al atoms of gibbsite 1layer, and SO_4 is between the gibbsite layers. When an Ni atom enters the center of an Al hexagon, lying OH bonds in the center stand up. These OH bonds then bind to SO_4 molecules by hydrogen bond.

The binding energy of H_2 to $NiSO_4$-intercalated gibbsite with relaxed spacing is very high (Figure 4.10). The binding energy for the first 9 H_2 molecules by SCAN + rVV10 ranges from -135 to -67 meV and the average value is -107 meV. The binding energy by PBE-D2 shows similar trend, and the average value for the first 9 H_2 molecules is -138 meV.

When the interlayer spacing is set to 10 Å, $NiSO_4$-intercalated gibbsite can accommodate two layers of H_2 molecules (Fig. 4.11). We fix the interlayer spacing because then approximately two layers of H_2 can reside between potential wells and the storage density will be large. In experiment, additional molecules larger than SO_4 is needed to be a pillar between the gibbsite sheets. H_2 forms

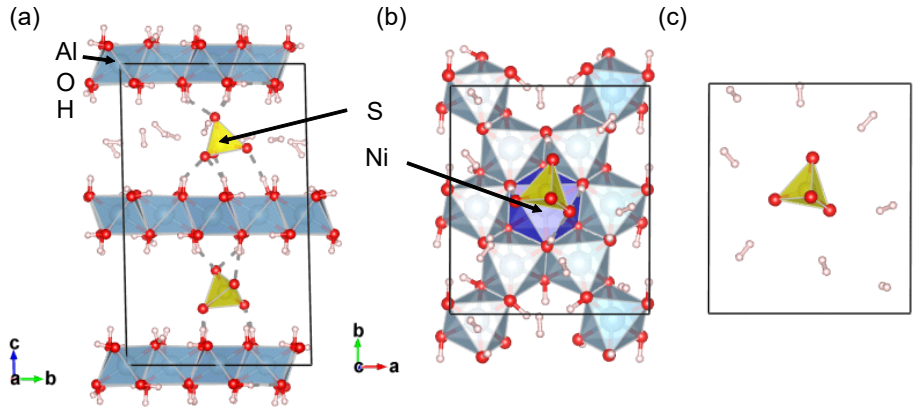

Figure 4.9: The binding of H_2 to $NiSO_4$-intercalated gibbsite with relaxed interlayer spacing. (a) The side view where H_2 forms a layer and interacts with the upper and lower gibbsite layers. Also, H_2 molecules point to charged O. The top view of showing the position of (b) SO_4 and (c) H_2.

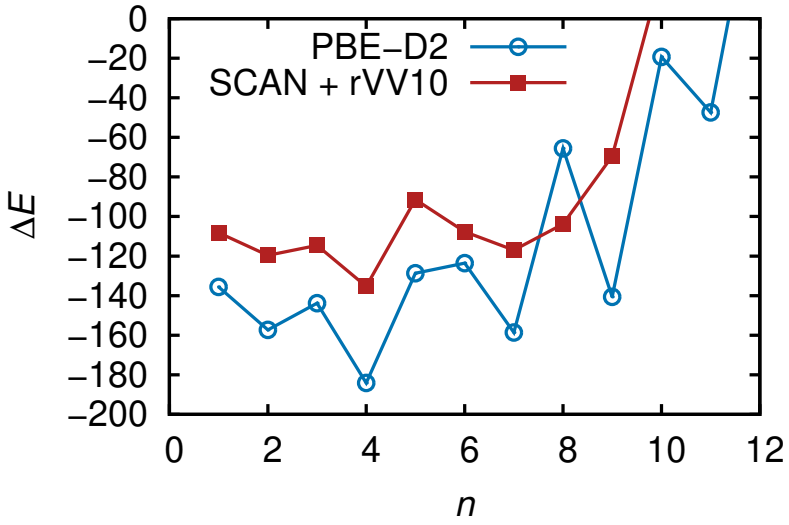

Figure 4.10: The binding energy of n-th H_2 molecule to $NiSO_4$-intercalated gibbsite with relaxed spacing.

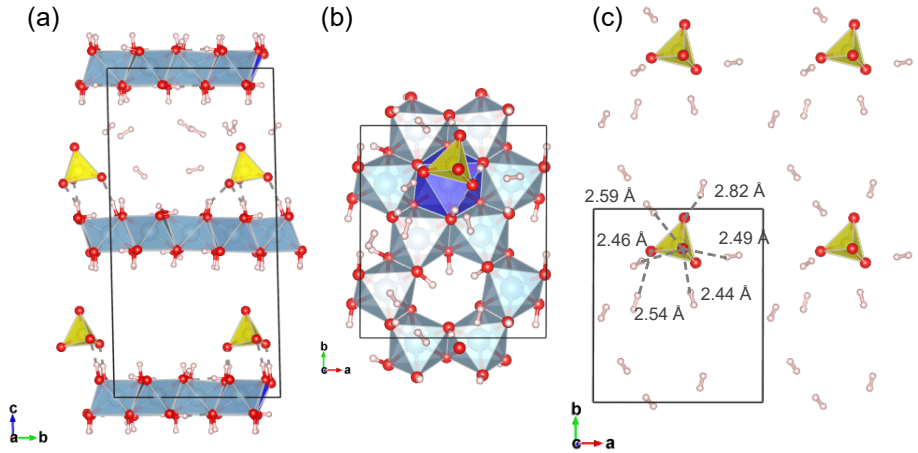

Figure 4.11: The binding of H_2 to $NiSO_4$-intercalated gibbsite, where the interlayer spacing is set to 10 Å. (a) The side view where H_2 forms two layers and bound to top and middle gibbsite layers. Also, H_2 molecules point to charged O. The top view of showing the position of (b) SO_4 and (c) H_2.

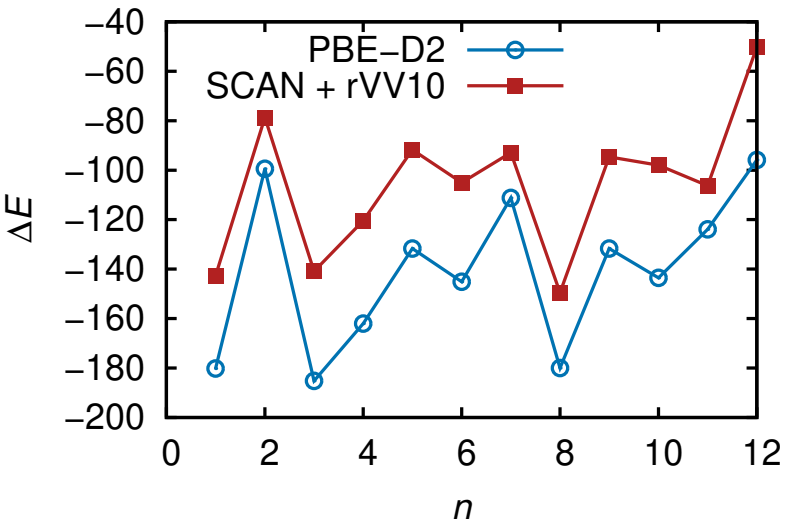

Figure 4.12: The binding energy of n-th H_2 molecule to $NiSO_4$-intercalated gibbsite, where the interlayer spacing is set to 10 Å.

two layers, where the upper H_2 layer binds to the upper gibbsite layer and SO_4, and the lower H_2 layer to the lower gibbsite layer and SO_4. Also, H_2 molecules point to charged O because polarization along the axis of H_2 molecule increases binding.

The binding energy of H_2 to $NiSO_4$-intercalated gibbsite is very high (Figure 4.12). The binding energy by SCAN + rVV10 ranges from -140 to -80 meV and the average value is -111 meV for first 11 H_2 molecules. The binding energy by PBE-D2 shows similar trend, and the average value for first 11 H_2 molecules is -145 meV.

$Ni(COO)_2$-intercalated gibbsite also can store many H_2 molecules (Fig. 4.13). Oxalate dianion ($(COO)_2$) is between the gibbsite layers. The interlayer spacing is optimized to 9.26 Å. H_2 also forms two layers near gibbsite layers. $(COO)_2{}^{2-}$ anions are charged and attracts H_2 molecules strongly. Figure 4.14 shows the binding energy and is as high as $NiSO_4$-intercalated gibbsite. The average binding energy for first 11 H_2 molecules is -130 meV for PBE-D2, and -99 meV for SCAN + rVV10, However, since SO_4 ion is large enough to form large space, the intercalation of $Ni(COO)_2$ is more advantageous than that of $NiSO_4$.

When the density of $Ni(COO)_2$ reduced by the half, the binding energy of H_2 reduced slightly (Fig. 4.15, Table 4.4). The binding strength is weaker than the case of high density Ni(COO)2 due to increased distance to the oxalate pillars. The oxalate has charged oxygen atoms and contributes to the binding. On the other hand, a pillar molecule reduces the space available for H_2 storage. Thus, reduced pillar density increases the available space, and the competition between binding energy and available space should be considered.

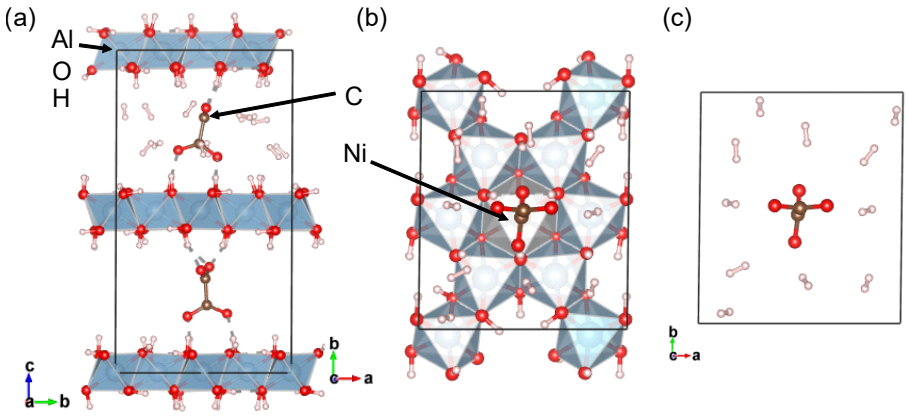

Figure 4.13: The binding of H_2 to $Ni(COO)_2$-intercalated gibbsite

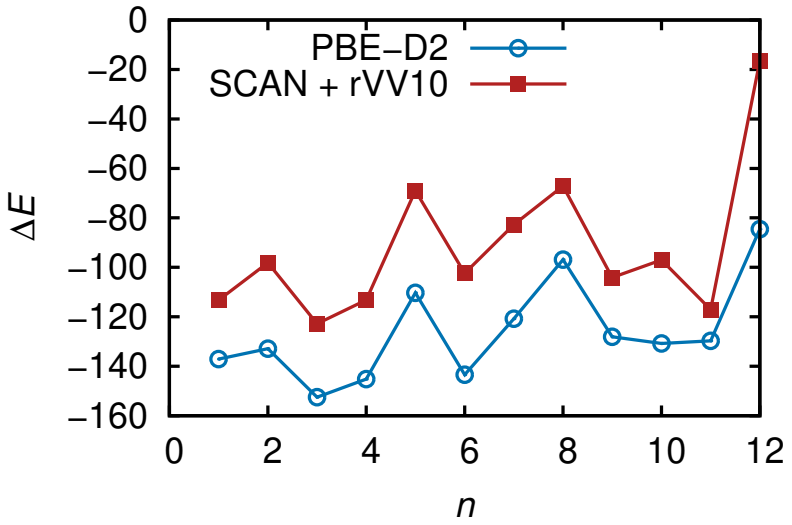

Figure 4.14: The binding energy of n-th H_2 molecule to $Ni(COO)_2$-intercalated gibbsite

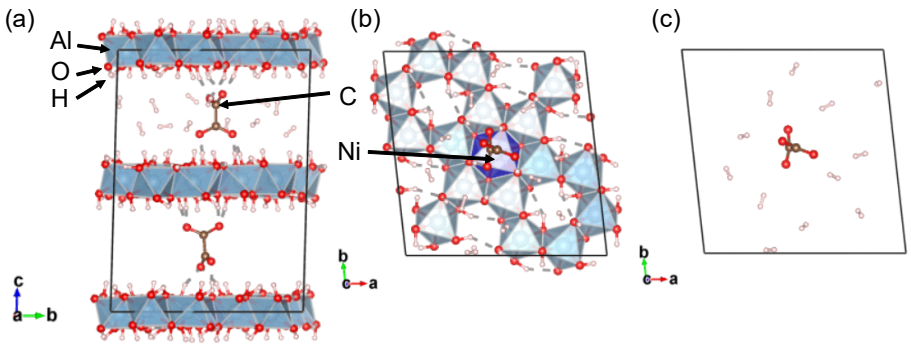

Figure 4.15: The binding of H_2 to sparse $Ni(COO)_2$ and gibbsite.

Table 4.4: The binding energy of n-th H_2 molecule to sparse $Ni(COO)_2$ and gibbsite.

Number of H_2 molecules	Binding energy (meV) when H_2 is relaxed by using PBE - D2	
	PBE-D2	SCAN + rVV10
1	-142	-108
2	-118	-104
3	-129	-111
4	-109	-87
5	-141	-90
6	-110	-84
7	-137	-100
8	-144	-89
9	-103	-79
10	-102	-75
11	-133	-93
12	-114	-89
Average	-124	-93

4.3.6 Grand canonical Monte Carlo simulation of the storage capacity

Figure 4.3.6 shows the potential energy surface of H_2 in $Ni(COO)_2$-intercalated gibbsite, or the binding energy obtained at three-dimensional grid points. The energy was calculated by using the density functional theory. In reality, a H_2 molecule rapidly rotates with a terahertz frequency, and the binding energy should be obtained by averaging the direction of the molecule. Here, we sampled only the upright direction as a first approximation. Since the direction is fixed, the maximum binding energy is lower than when the direction was relaxed (Fig. 4.14).

Figure 4.3.6 shows the grand canonical Monte Carlo simulation of the storage capacity of NiOxalate-intercalated gibbsite at 298.15 K. The interaction energy of a H_2 molecule to NiOxalate-intercalated gibbsite at an arbitrary point in space is linearly interpolated from the binding energy at grid points by density functional theory. The z-projected density (Fig. 4.3.6(b)) indicates that the H_2 molecules are populated near a gibbsite layer, and when it is far from a layer in the middle plane, the density reduces. This population is consistent with high potential energy near the gibbsite (Figs. 4.3.6(d) and (e)). Figs. 4.3.6(c) and (d) displays the gravimetric and volumetric storage capacity obtained by the grand canonical Monte Carlo simulation. The storage density is moderate since the available space is limited as illustrated in Fig. 4.3.6(b), and the potential is not very strong.

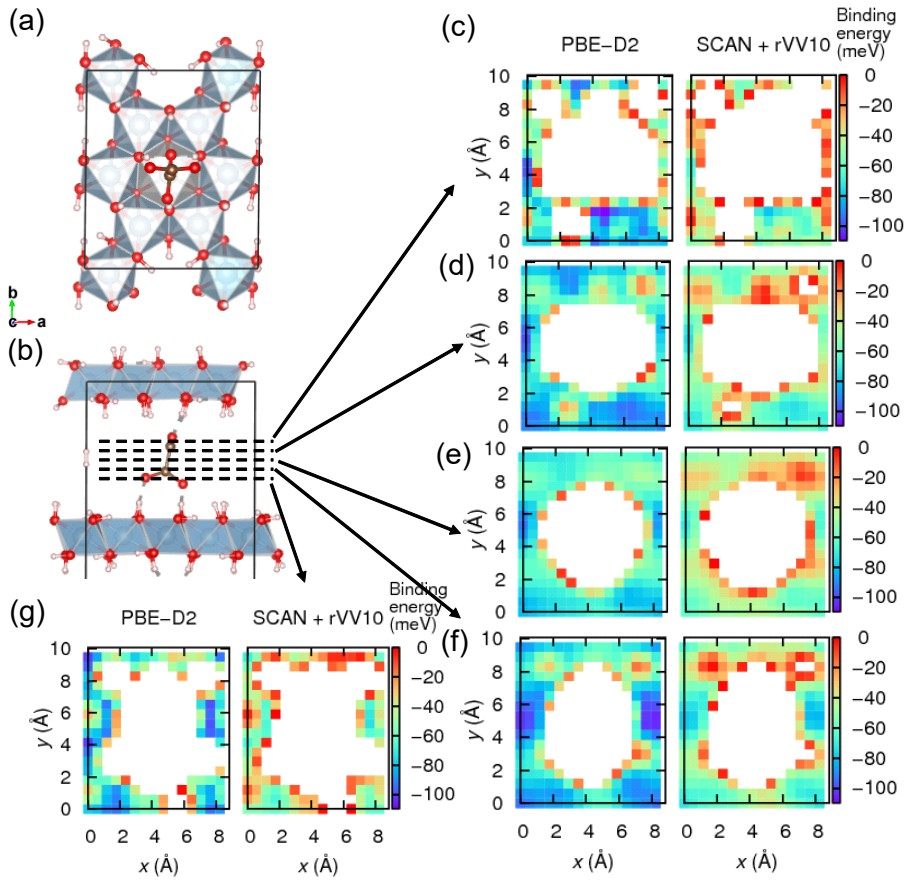

Figure 4.16: The potential energy surface of H_2 in $Ni(COO)_2$-intercalated gibbsite. The optimized interlayer distance is 9.26 Å, and the size of grid is 0.59 Å. (a) The top view and (b) the side view of NiOxalate-intercalated gibbsite. The dashes indicate sections. (c–g) The binding energy, or potential of an upright H_2 molecule to NiOxalate-intercalated gibbsite evaluated by using PBE-D2 and SCAN + rVV10 functionals. White means the binding energy is positive, or H_2 is nonbonding due to steric hindrance.

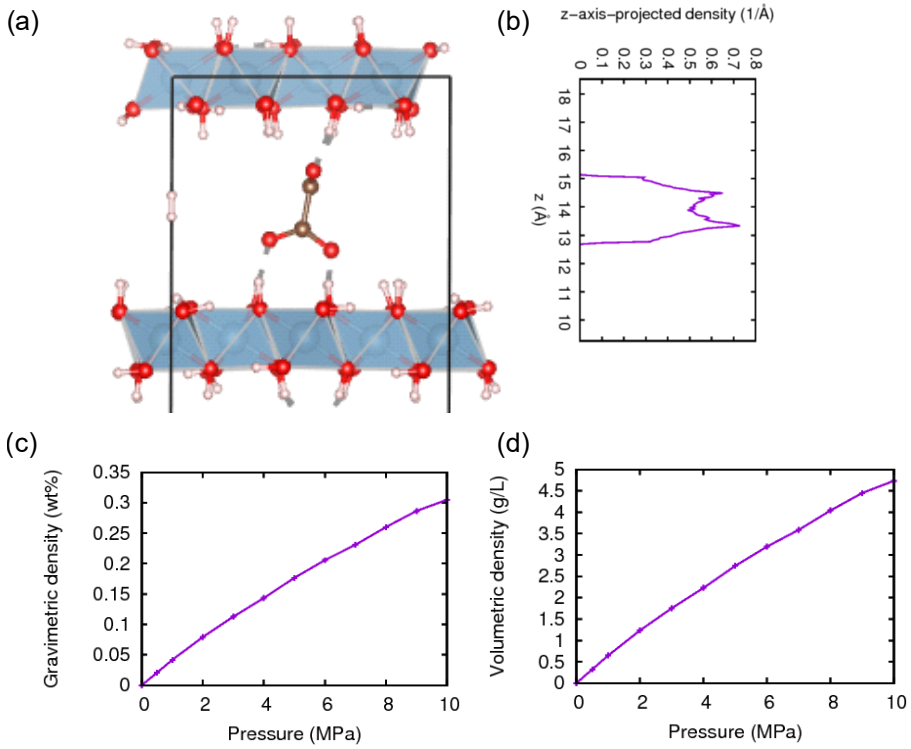

Figure 4.17: Grand canonical Monte Carlo simulation of the storage capacity of NiOxalate-intercalated gibbsite at 298.15 K using the potential by the rVV10 functional. (a) The side view and (b) the z-projected density at 10 MPa. The z values in (b) coincide to the z values in (a). (c) The gravimetric storage density and (d) volumetric storage density.

4.4 Conclusions

We studied the hydrogen storage in $NiSO_4$-intercalated gibbsite, and $Ni(COO)_2$-intercalated gibbsite. The binding energy for first 11 H_2 molecules were -111 and -99 meV by using SCAN + rVV10 functional. These high binding energy are advantageous for storing H_2 safely under pressure lower than high-pressure vessels.

Chapter 5

Structures and properties of monolayer, adsorbed, and intercalated FeS

5.1 Introduction

In a previous chapter, we studied the hydrogen storage in the potential well of intercalated layered material gibbsite. However, the storage density needs to be improved further for applications. A competitive layered material is tetragonal iron sulfide (FeS, mackinawite). Tetragonal FeS is the major constituent of FeS precipitated from aqueous solutions in anoxic conditions [134]. It is widespread in low-temperature aqueous environments. FeS has magnetism arising from strong itinerant spin fluctuation, which means that spins are not localized but nearly free-electron like [135]. FeS is advantageous for hydrogen storage in many aspects. Because it is composed of light elements, it is advantageous for high weight ratio of stored H_2 to storage material. The atomic mass of Fe is 55.8, which is much less than that of Mo, 95.9. Therefore, FeS is much lighter than MoS_2, a transition metal dichalcogenide. The S of FeS has lone pair electrons that is negatively charged and attracts H_2 well by polarizing H_2. Also, FeS is composed of inexpensive elements and was stable in air for at least 3 months [136].

Moreover, the large surface area of FeS upon intercalation can be useful for supercapacitor also. Supercapacitor stores energy by utilizing the electric

double layer between electrode and electrolyte, and the possible reduction and oxidation of the electrode material [137, 138]. Since FeS is metallic [136], it may be suitable for an electrode material. The transition metal Fe may induce a reduction and oxidation and may be advantageous for storing energy.

To utilize FeS for hydrogen storage or supercapacitor, it should be intercalated to add a spacing between the layers. Ammonia (NH_3) has been intercalated in FeS, and its conductivity was measured [139]. In relation to the intercalation, the adsorption on FeS has been studied. Dzade et al. investigated the water adsorption and dissociation on the side surfaces of FeS mackinawite [140], and on the oxygen-covered surfaces of FeS [141]. The adsorption of methylamine [142] and cystein [143] on FeS surfaces have been studied in order to increase the FeS crystal's side surfaces that are able to catalyze some reactions. The reactions of NO_x [144] and CO_2 [145] on the surfaces of FeS have also been studied.

However, the increased layer spacing of FeS is limited. In this study, we examine the increased layer spacing and the bonding of ammonia and tetraalkylammonium-intercalated FeS. Specifically, the investigated intercalants are ammonia, tetraethylammonium hydroxide, and tetrabutylammonium hydroxide. Ammonia and tetraalkylammonium ions are good intercalants because the length of alkyl chain, and hence the interlayer spacing can be tuned. As a basic study, the electronic structure of a monolayer and bulk FeS mackinawite are compared, and the surface energy of FeS is calculated. The adsorption of various atomic and molecular species to a monolayer FeS is studied since this is a reference for analyzing the interaction of FeS to the species in real experiments.

5.2 Computational Methods

We carried out electronic structure calculations based on the density functional theory (DFT) with an exchange-correlation functional by Perdew, Burke, and Ernzerhof (PBE) [64] and the van der Waals interaction correction D2 by Grimme, [74]. As an exception, the correction was not used for the calculation of cohesive energy. We employed the projector augmented-wave pseudopotential [124] as implemented in the Vienna *ab initio* simulation package (VASP) 5.4 [125]. The energy cutoff for the plane-wave basis set was 520 eV when the shape of a cell was relaxed, and otherwise 400 eV. The structure was relaxed until the force on each atom was less than 0.02 or less eV/Å. The **k**-point meshes used for sampling the Brillouin zone were $13 \times 13 \times 9$ for the unit cell of FeS, and $13 \times 13 \times 1$ for a slab. For adsorption studies, the size of the supercell was 3×3 of the unit cell, and the mesh was $4 \times 4 \times 1$. For NH_3 intercalated FeS, the mesh was $13 \times 13 \times 5$. For FeS with intercalated tetraethylammonium hydroxide, the supercell was 3×3 of the unit cell, and the mesh was $4 \times 4 \times 4$. For FeS with intercalated tetrabutylammonium hydroxide, the supercell was 4×4 of the unit cell, and the mesh was $3 \times 3 \times 2$. The Bader charge analysis was used to determine the atomic charge [146] , and the orbital charges were estimated from the projection of the PAW method. The energy of adsorption or intercalation of atom or molecule A was calculated by $\Delta E = E[(\text{FeSsupercell})A) - [E((\text{FeSsupercell})) + E(A)]$. Negative value of ΔE means that the adsorbed or intercalated state is stable. Nonmagnetic calculation was performed for FeS, while the magnetization of the atoms and molecules are considered (?). The adsorption or intercalation energy by PBE was evaluated at the structure relaxed by PBE with the vdW correction. The contribution of

Table 5.1: The structure of single layer and bulk FeS

Structural parameter	Theory		Experiment [136]
	Single layer	Bulk	Bulk
$a(=b)$ (Å)	3.555	3.564	3.6802
z_S (Å)	1.233	1.219	1.269
c (Å)		4.908	5.0307

the vdW energy ΔE_{vdW} to the energy change was approximated as $\Delta E_{vdW} = E_{vdW}[(FeS)_{18}A] - \{E_{vdW}[(FeS)_{18}] + E_{vdW}(A)\}$, where E_{vdW} is the Grimme's DFT-D2 correction of vdW energy. For vibrational analysis, density functional perturbation theory was utilized to determine interatomic force constants and Γ-point phonon spectrum.

5.3 Results and Discussion

5.3.1 Structure

The structure of a single layer FeS is slightly different from a layer in the bulk counterpart due to the absence of interlayer interaction. The single layer FeS has Fe in the planar square lattice and S on and under the Fe lattice (Fig. 5.1). An S atom is coordinated with 4 Fe atoms, and an Fe atom is in a tetrahedron of S atoms. The in-plane lattice constant ($a = b$) of a single layer is 3.555 Å, slightly smaller than its bulk value 3.564 Å(Tab. 5.1).

When the single layers are stacked, the interlayer vdW interaction stabilizes the structure. As the bulk lattice constant decreases from the single layer's value, the atoms in different layers become closer. Then the atoms' van der

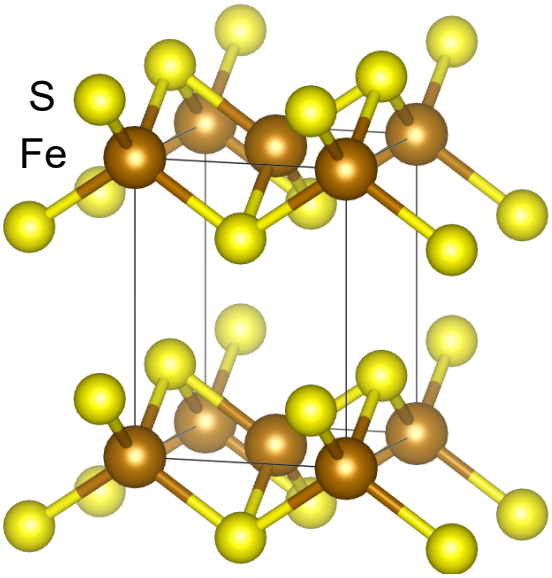

Figure 5.1: The structure of FeS. The bulk FeS is shown. The single layer FeS is nearly identical to a layer in the bulk.

Waals interaction increases. The contraction of the lattice constant stabilizes the structure in spite of increased in-plane lattice elastic energy. Thus, a single layer's in-plane lattice constant is slightly less than its bulk value. The height of the anion S (z_S) from the Fe plane in the bulk (1.233 Å) is slightly less than its single-layer counterpart (1.219 Å).

5.3.2 The electronic band structure of single layer and bulk FeS

Previously Lebegue et al. [147] performed high-throughput electronic structure calculations of a single layer FeS along with nearly a hundred layered materials. Here, we obtain the band of single layer FeS and describe it in detail. Welz et al. [148] and Hao et al. [149] calculated the band of bulk FeS, and Kwon et al. [135] obtained its projected density of states. Here, we calculate the bulk

band to compare it with the band of the single layer.

The single layer FeS has Fe *d* orbitals at the Fermi level. Nonmagnetic calculation was performed. The electronic structure of FeS is derived from Fe and S atoms. The electronic band is shown in Fig. 5.2, and the atom-projected density of states is shown in Fig. 5.2. Fe has valence electron configuration $3d^6 4s^2$. Fe p orbitals have low energy, -53 eV (not shown in Fig. 5.2). Fe *s* orbitals are at -6 eV, and Fe *d* orbitals are at the Fermi level. When spin degeneracy is neglected, there are 5 states for *d* orbitals. The number of states, and the bonding and antibonding of two Fe atoms in a unit cell form 10 states near the Fermi level, as in the case of bulk FeS [148]. If the spin degeneracy is counted, there are 20 *d* states. Fe atoms are close to each other, and the distance between them is 2.514 Å, similar to bcc Fe's nearest neighbor distance 2.48 Å [150]. So the Fe *d* bands are dispersive, and the bandwidth is as large as 6 eV. The Fermi level is at the *d* bands, and so the single layer FeS is a metal.

Below the Fe *d* bands, there are S *p* bands. The valence electron configuration of S is $3s^2 3p^4$. The *s* bands have low energy at -14 eV (not shown in Fig. 5.2). When spin degeneracy is neglected, a *p* orbital has three states. The number of states, and the bonding and antibonding of two S atoms in a unit cell form 6 *p* bands below the Fe *d* bands. The spin degeneracy doubles the number of bands to 12. The bonding states have lower energy then the antibonding states. The *p* bands are hybridized with Fe *d* orbitals. Our band structure of single layer FeS band agrees with a previous result [147].

As the single layers of FeS are stacked to form a bulk, the bonding and antibonding among them affects the electronic structure slightly. The filled shell layers interact via weak hybridization, and small dispersion along out-of-plane

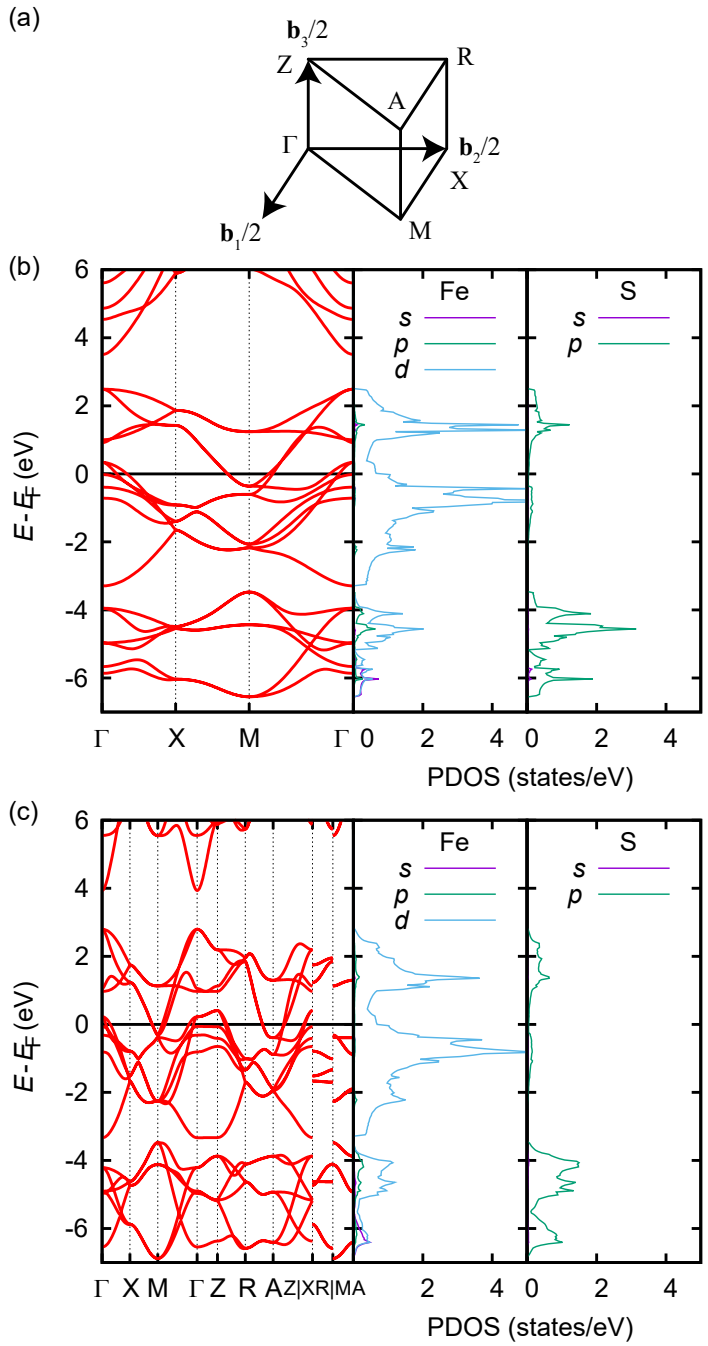

Figure 5.2: The band structure and projected density of states (PDOS) of (a) single layer and (b) bulk FeS.

crystal momentum is produced, which is along Γ-Z, X-R, and M-A. The dispersions of the S *p* bands are greater than that of the Fe *d* bands near the Fermi level because in a bulk, the top S atoms of a layer and bottom S atoms of above layer are in contact. Our bulk band and PDOS agrees with previous calculations [135, 148, 149].

5.3.2.1 Cohesive energy

The single layer and bulk FeS forms a strong ionic bond. The vdW correction by Grimme was not used for cohesive energy because the correction overestimates the cohesive energy (per atom) of magnetic bcc Fe solid from 4.88 eV to 5.28 eV. Without the vdW correction, the cohesive energy is more close to an experimental value, 4.28 eV [151]. The cohesive energy of single layer nonmagnetic tetragonal FeS per atom is 5.01 eV, and that of bulk per atom is 4.99 eV. These values are similar to our calculation of the cohesive energy of nonmagnetic troilite FeS, 4.47 eV, whose structure was from a previous work [152], and Raybaud's calculation of troilite FeS, 4.43 eV [153]. Since the troilite is stable, tetragonal FeS could be stable if cohesive energy is considered.

5.3.2.2 Surface energy

Fig. 5.3) shows the surface energy of few layer FeS. The converged surface energy is 12.7 meV/m^2. The cleavage energy is the energy required to separate a bulky material into two parts by cleaving across a basal plane [154]. The cleavage energy is twice the converged surface energy, 25.4 J/m^2. The main component of the cleavage energy is the attractive van der Waals correction by Grimme and repulsive Pauli repulsion from PBE. The interaction is mainly of

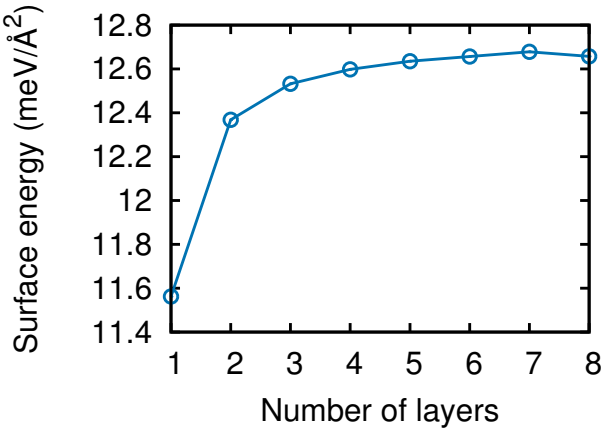

Figure 5.3: The surface energy of few-layer FeS.

van der Waals and stronger covalent bond lacks because a single layer of FeS is chemically inert. That is, the S atoms at the top and bottom boundary of a layer lack sufficient electronic states near the Fermi level, so the S atoms of neighboring layers do not form covalent bond. The small interlayer interaction of FeS means that its exfoliation is as easy as other vdW layered materials.

5.3.3 Adsorption of atoms and molecules on a monolayer FeS

Figure 5.3.3 displays various species adsorbed on a monolayer FeS, and Table 5.3.3 lists the analysis of adsorption. Adsorption energies show that charged species adsorb strongly, while neutral ones adsorb weakly. The weak interaction of the neutral ones are primarily of van der Waals interaction which is roughly estimated by the difference of binding energy (ΔE) by PBE-D2 and by PBE. The binding of a K atom on 4 S atoms is stronger than that for a K atom on 2 S atoms due to increased number of bonds or enhanced electrostatic stabilization. The adsorption energy of a Li atom to FeS relative to Li solid is a reference data

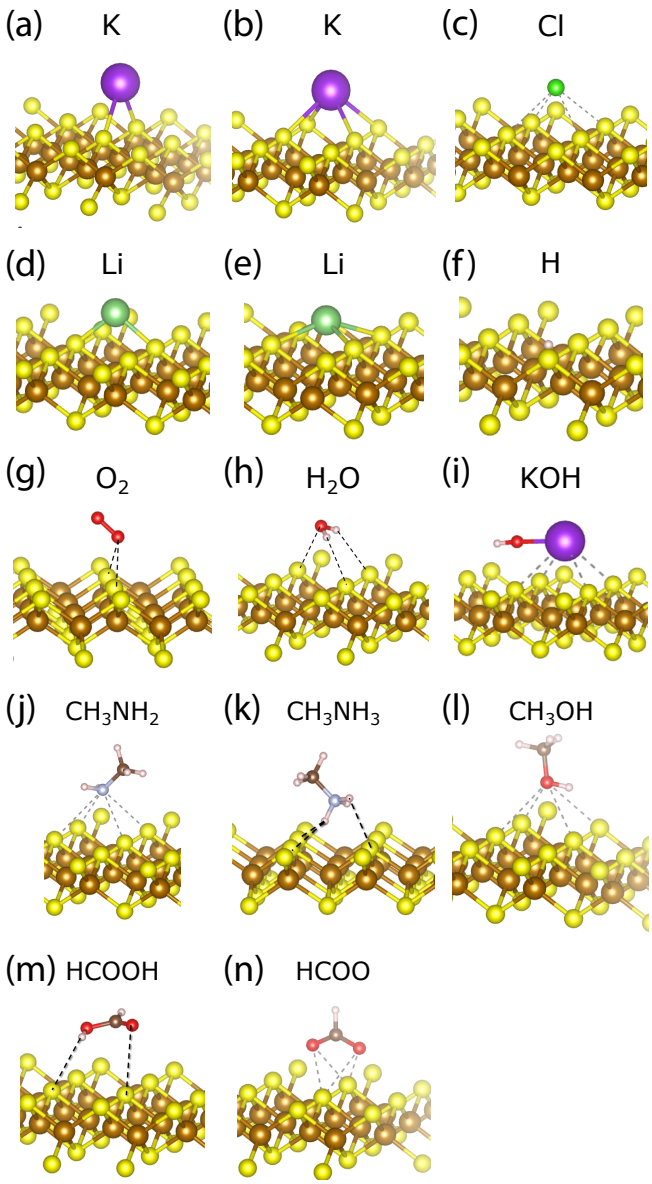

Figure 5.4: The structure of adsorbed atoms and molecules on a single layer FeS. The adsorbed species are the following: (a) K^+ on two S atoms, (b) K^+ on four S atoms (c) Cl^-, (d) Li^+ on 2 S atoms, (e) Li^+ on 4 S atoms, (f) H^+, (g) O_2, (h) H_2O (water), (i) KOH (potassium hydroxide) (j) CH_3NH_2 (methylamine), (k) $CH_3NH_3^+$ (methylammonium), (l) CH_3OH (alcohol), (m) HCOOH (formic acid), and (n) $HCOO^-$ (formate).

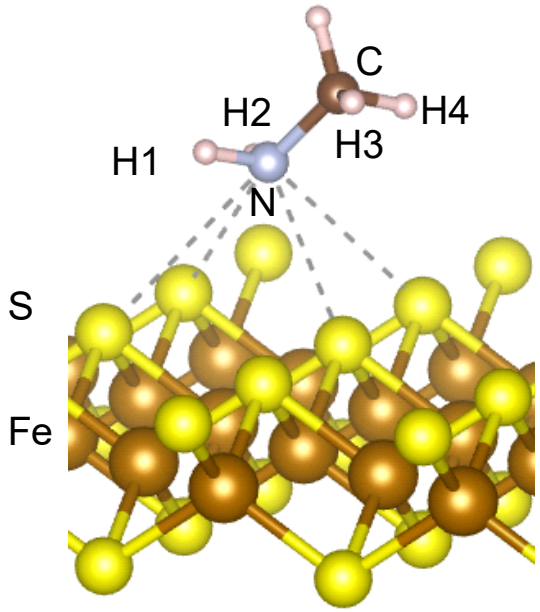

Figure 5.5: The adsorption of methylamine on a monolayer FeS.

when FeS is used as an electrode of a Li-ion battery.

5.3.3.1 Adsorption of methylamine

Methylamine is widely used as a capping ligand. Dzade et al. investigated the adsorption energy of methylamine on a single layer FeS [142], and we analyze it in more detail. At the structure optimized by using vdW correction (Fig. 5.3.3.1), the PBE binding energy of methylamine on a single layer FeS is -0.001 eV. With the vdW correction, the binding energy increases to -0.259 eV. The binding energy agrees with a previous calculation [142]. The binding comes mainly from the vdW interaction. Large vdW interaction comes from many close pairs of N-S, H-N, and N-Fe.

We studied the electronic structure of methylamine adsorbed on a single layer FeS. Fig. 5.6 shows the projected density of states of methylamine. The

Table 5.2: Adsorption of atoms and molecules on FeS. Adsorption energies evaluated by using PBE and PBE-D2, and Bader charges are shown. Charged species adsorb strongly, while neutral ones adsorb weakly via van der Waals interaction. The label column is pointing the subfigure of Fig 5.3.3 where the geometry of the adsorbed structure is shown. ΔE-atom denotes that ΔE is evaluated relative to the atomic adsorbant. ΔE-solid denotes that ΔE is evaluated relative to the solid phase of adsorbant.

Label	Adsorbate	ΔE (PBE)	ΔE (PBE-D2)	q ($\|e\|$)	Neighboring atoms and distance (Å)
(a)	K^+ on 2 S atoms	-1.98			K-S 3.03
(b)	K^+ on 4 S atoms	-2.28	-0.37	0.88	K-S 3.22
(c)	Cl^-	-1.186	-1.382	-0.568	Cl-S 3.200
(d)	Li^+ on 2 S atoms	ΔE-atom: -2.23		0.90	Li-S 2.33
		ΔE-solid: -0.63			
(e)	Li^+ on 4 S atoms	ΔE-atom: -2.62		0.89	Li-S 2.67
		ΔE-solid: -1.01			
(f)	H^+	-1.43		-0.11	H-S 2.64
(g)	O_2	-0.113	-0.319		O-S 2.77
(h)	H_2O		-0.172		H-S 2.70
(i)	KOH	-0.407	-0.858		K-S 3.295
(j)	CH_3NH_2	-0.001	-0.259		N-S 3.39
(k)	$CH_3NH_3^+$	-2.383	-2.809		H-S 2.34
(l)	CH_3OH	-0.001	-0.188		O-S 3.30
(m)	HCOOH	0.008	-0.204		H-S 2.81
(n)	$HCOO^-$	-0.900	-1.185		O-S 2.87

Table 5.3: Orbital charge of methylamine adsorbed on FeS before adsorption, and the change after adsorption.

Atom	*s* orbital		*p* orbital		*d* orbital	
	Before	Change	Before	Change	Before	Change
N	1.235	0.000	2.643	0.006	0	0
H1	0.651	-0.002	0.077	0.000	0	0
S1	1.347	0.000	2.343	0.002	0	0
S2	1.347	0.004	2.343	-0.010	0	0
Fe1	0.352	0.000	6.418	0.001	6.355	0.000
Fe2	0.352	0.000	6.418	0.001	6.355	-0.001

slightly broadened N *p* peak means that N *p* electrons are weakly hybridized. Weakly changed S *p* shows a small hybridization.

5.3.3.2 Orbital Charge of Methylamine on FeS

Orbital charge does not change appreciably after adsorption, in agreement with small adsorption energy (Tab. 5.3). Note that the orbital charge means the charge near the core captured by the projector augmented-wave method, and does not necessarily involve small change of valence charge. The maximum change of methylamine is only 0.010. Tiny charge seems to transfer from S2 to N. The direction of charge transfer agrees with the electronegativity: S, 2.6; N, 3.0.

5.3.3.3 Pairwise vdW correction of methylamine and FeS

The pairwise vdW correction of methylamine and FeS is studied. As the number of electrons in an atom increases, more electrons fluctuate and produce transient dipole moment. So its vdW increases. Fig. 5.7 shows the decomposition of vdW interaction correction between methylamine and a single layer FeS. The largest

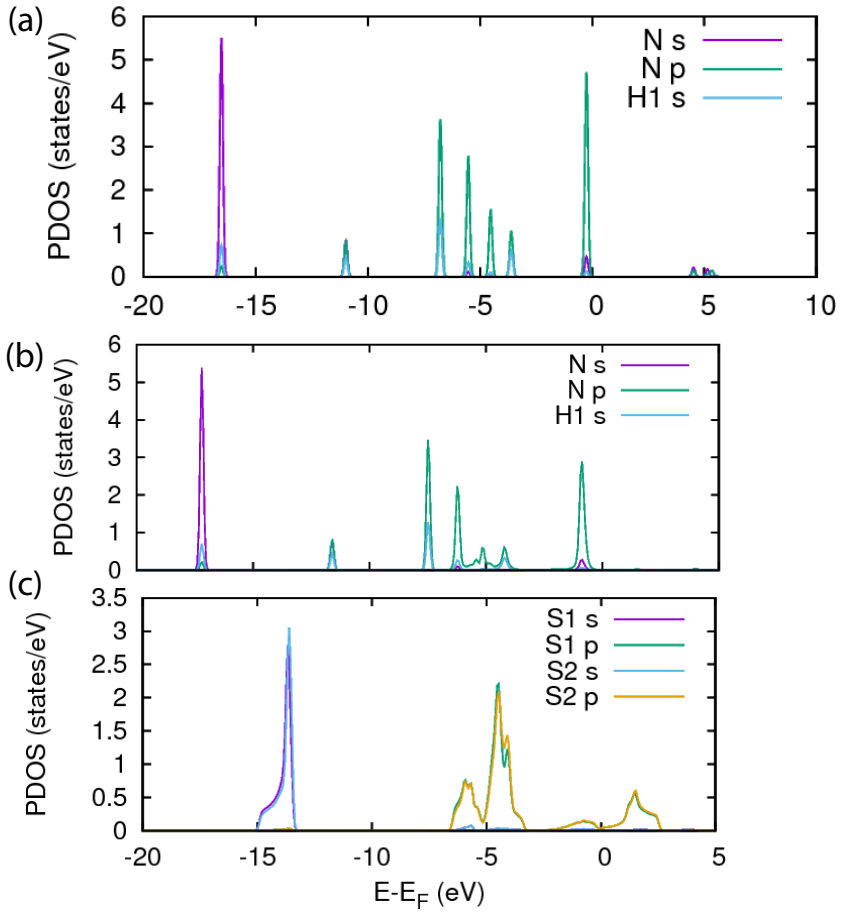

Figure 5.6: The change of PDOS upon the adsorption of methylamine on FeS. The PDOS's belong to (a) free methylamine, (b) adsorbed methylamine, and (c) FeS with adsorbed methylamine.

contribution comes from the N-S and N-Fe pairs. The vdW correction for 4 nearest pairs consist of 68 % of total $\Delta E_{\mathrm{vdW}} = -258$ meV. The remaining is from more distant pairs. Here, ΔE_{vdW} is very close to $\Delta E = -259$ meV.

5.3.4 The intercalation of NH_2 and tetraalkylammonium hydroxides in FeS

Figure 5.8 shows the structures of intercalated FeS. The structure of NH_3-intercalated FeS is shown in Fig. 5.8(a). Since NH_3 is a small molecule, it would be placed on the hollow site formed by 4 adjacent top S atoms of the bottom layer, and below the 4 adjacent bottom S atoms of the top layer. An H atom of NH_3 is at the hollow site probably because the H atom and the below S atoms are close and has large stabilization from vdW interaction. Figure 5.8(b,c) shows the structure of FeS intercalated with tetraalkylammonium hydroxides. To obtain reliable interlayer spacing, we focused on the interaction between an intercalate and the layers. We ignored a complex interaction between the intercalates in experiment, and placed an intercalate in a large supercell. The long alkyl chains have diverse configuration and we calculated the flat configurations. In experiment, the interaction between the chains may alter the configuration. Tetraethylammonium and tetrabutylammonium cations were distanced from the layers, while the small OH^- ions were bonded to FeS layers.

Table 5.4 shows the properties of intercalated FeS. When NH_3 is intercalated, the interlayer spacing is increased. A tetraethylammonium cation is larger than NH_3, and the interlayer spacing of tetraethylammonium-hydroxide-FeS is greater than that of NH_3-FeS. However, when tetrabutylammonium hydroxide is intercalated, the interlayer spacing did not change appreciably. This is

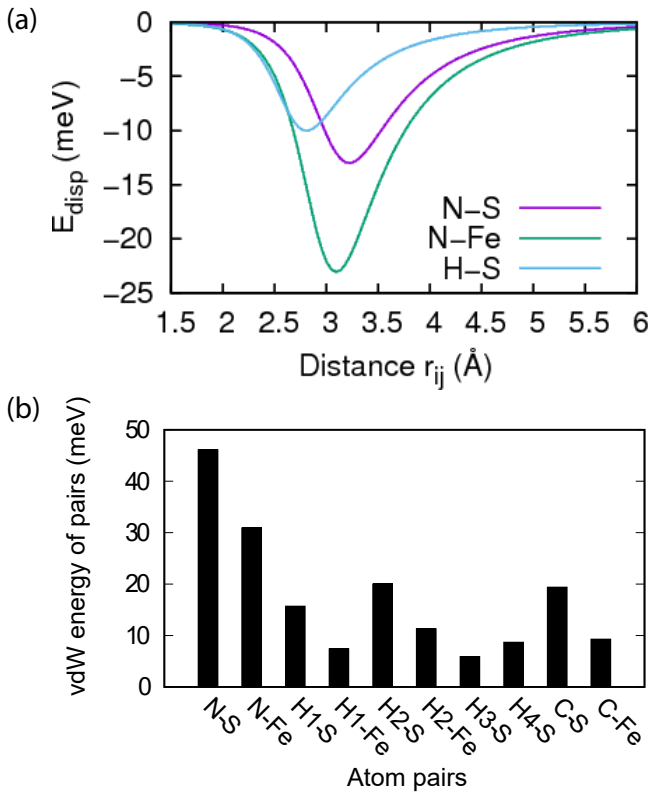

Figure 5.7: The decomposition of van der Waals interaction between adsorbed methylamine and FeS. (a) vdW correction to the total energy for a pair of atoms. (b) The vdw correction for 4 nearest pairs of given atomic pairs.

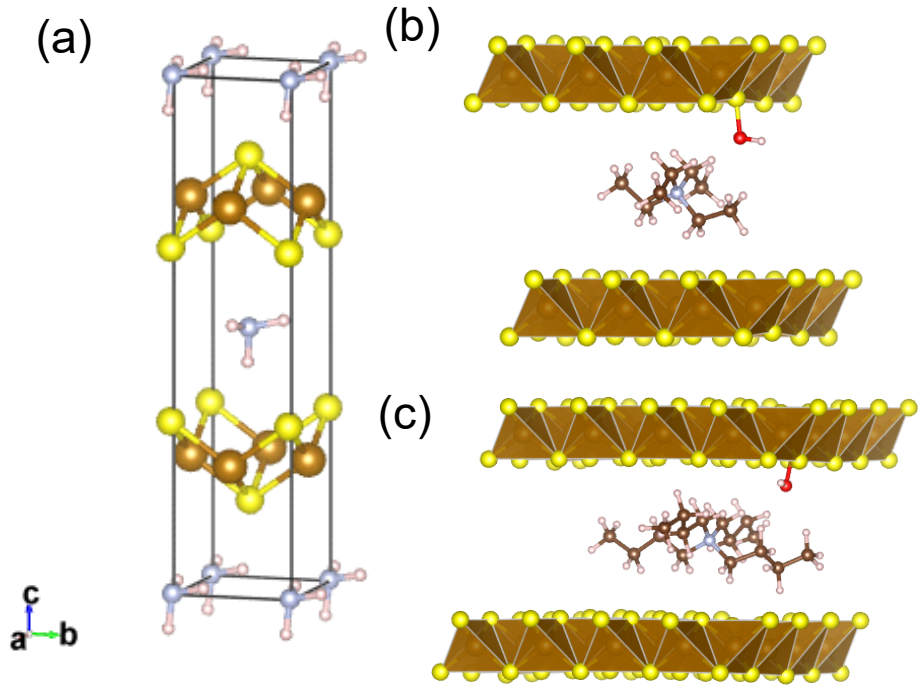

Figure 5.8: Structures of intercalated FeS. The intercalates are (a) NH_3, (b) tetraethylammonium hydroxide, and (c) tetrabutylammonium hydroxide.

Table 5.4: Properties of Intercalated FeS

Intercalated molecule	Layer spacing (Å)	Bader charge ($\|e\|$)			Intercalation energy per molecule (eV)	
		Cation or NH_3	Anion	FeS	PBE	PBE-D2
NH_3	7.512	0.00	None	0.00	-0.122	-0.273
Tetraethylammonium hydroxide	10.05	0.86	-0.48	-0.38	-1.607	0.228
Tetrabutylammonium hydroxide	10.02	0.82	-0.49	-0.32	-1.418	1.644

because we assumed flat configurations of alkyl chains. The Bader charge of NH_3 shows it is neutral and charge transfer is negligible. Tetraalkylammonium cations are positively charged while OH^- anions are negatively charged as expected. Charge transferred from OH^- to FeS and the small OH^- anion is stabilized. Because a free OH^- anion is unstable, during an intercalation experiment in an aqueous solution, H_2O molecules may accompany the OH^- anion and are intercalated together to stabilize the structure and form a hydrate. This is similar to the formation of solid tetrahydrate tetraethylammonium hydroxide [155].

The intercalation energy per molecule for NH_3-FeS is -0.122 eV at PBE level which means that weak hybridization of NH_3 and FeS is stable. When the vdW correction D2 is added, the intercalation is more favored, meaning that vdW is significant in the intercalation of NH_3 in FeS. Tetraalkylammonium hydroxides formed strongly bond intercalates at the PBE level because OH^- anion is closely bonded to FeS. When the vdW is taken into account, the intercalation product becomes unstable because the great vdW attraction between the large supercell layers could not be compensated by bonding to sparse intercalates. In experiment, the intercalates would be closely packed, and the intercalation product would be stabilized.

Figure 5.3.4 displays the wave number of the vibration of tetraethylammonium hydroxide-intercalated FeS. These vibrations can be observed by the corresponding wave number of the absorption peaks in the infrared spectrum. The wave number for bulk FeS is the wave number of phonon at the Γ point in the Brillouin zone (Fig. 5.3.4(a)). The wave number for FeS is small since Fe and S are heavy elements, while the wave number for tetraethylammonium hydroxide is large since C, H, and N are light elements (Fig. 5.3.4(b)). The wave

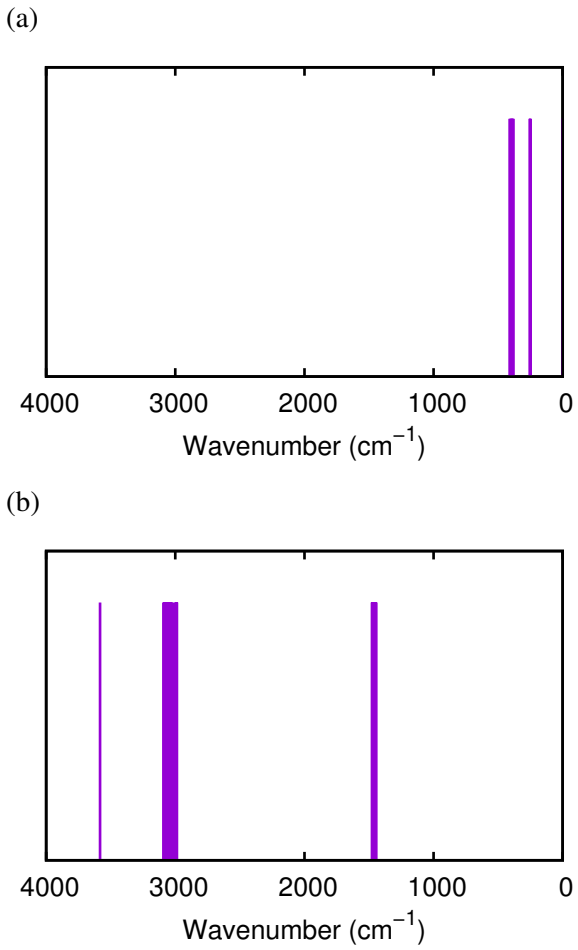

Figure 5.9: The wave number of the vibration of bulk FeS and tetraethylammonium hydroxide intercalated in FeS. (a) For the vibration with the wave vector at the Γ point of bulk FeS. (b) For the vibration for tetraethylammonium hydroxide in FeS.

number for the stretch of the O-H bond is 3600 cm^{-1}, that for C-H bond is 3000 cm^{-1}, and that for C-C or N-C bonds is 1500 cm^{-1}.

5.4 Conclusions

We have studied the electronic structure and properties of intercalated FeS for possible application in energy storage. When the size of intercalate increases from NH_3 to tetraalkylammonium hydroxides (tetraethylammonium hydroxide and tetrabutylammonium hydroxide), the interlayer spacing increased. This tuning of interlayer spacing will be useful for optimization of hydrogen storage material or supercapacitor electrode. The charge transfer from NH_3 to FeS was negligible, while OH^- anions donated charge to S of FeS and formed strong bond. The intercalation energy shows that the intercalation of NH_3 is stable, and for sparse tetraalkylammonium hydroxides, the intercalation is not favorable. Increased density of tetraalkylammonium anions or co-intercalation with H_2O may stabilize the intercalation product. We also studied the electronic band structure of monolayer and bulk FeS, its surface energy, and adsorption of various atoms and molecules common in real-world experiments.

Chapter 6

Conclusions

Hydrogen is an environment-friendly energy carrier useful for reducing the air pollution from fossil fuels. The hydrogen storage is one of crucial topics for commercialization of hydrogen energy. Current vehicles store hydrogen in a pressure vessel of 700 atm, which can be dangerous upon car accident.

For safer method of hydrogen storage, we have studied the hydrogen storage in $Mg(NH_2)_2$ and LiH which utilizes a strong ionic bond. KH is known to reduce the reaction temperature of $Mg(NH_2)_2$. We have studied the hydrogen storage and release mechanism for the magnesium amide system based on *ab initio* theoretical methods. This work presents a detailed dehydrogenation mechanism of the system, and aids in designing new catalysts to further lower the reaction temperature.

Another way to compensate the high reaction temperature of chemical hydride is to store hydrogen in the potential well of layered material by physisorption. This system is also advantageous in improving the slow kinetics of the hydride systems. We have investigated the hydrogen storage in $NiSO_4$-intercalated gibbsite, and $Ni(COO)_2$-intercalated gibbsite. Both systems have high capacity for storing H_2. This strong physisorption is advantageous for storing H_2 safely under low pressures, with fast kinetics at room temperature.

In Chapter 5, we have studied the electronic properties of another candidate layered material FeS. Due to its high surface area and metallicity, it can be also

Table 6.1: H_2 storage in gibbsite and FeS

	Gibbsite	FeS
H_2 binding energy on a layer using PBE-D2 (meV)	-119.6	-77.8
Mass per unit area (a.m.u/Å^2)	7.08	12.98

useful for supercapacitor electrode. When the size of intercalate increases from NH_3 to tetraalkylammonium hydroxides, the interlayer spacing increases. This tuning of interlayer spacing will lend itself well for optimization of hydrogen storage material or supercapacitor electrode.

The H_2 storage in gibbsite and FeS is compared in Table 6.1. Although gibbsite is advantageous over FeS for H_2 storage, FeS another possibility to be used as a supercapacitor electrode.

Bibliography

[1] R. Ströbel, J. Garche, P. Moseley, L. Jörissen, and G. Wolf, "Hydrogen storage by carbon materials," *J. Power Sources*, vol. 159, no. 2, pp. 781–801, 2006.

[2] M. Sevilla, R. Mokaya, and A. B. Fuertes, "Ultrahigh surface area polypyrrole-based carbons with superior performance for hydrogen storage," *Energy. Environ. Sci.*, vol. 4, no. 8, pp. 2930–2936, 2011.

[3] M. Dinca, A. Dailly, Y. Liu, C. M. Brown, D. A. Neumann, and J. R. Long, "Hydrogen storage in a microporous metal- organic framework with exposed Mn^{2+} coordination sites," *J. Am. Chem. Soc.*, vol. 128, no. 51, pp. 16876–16883, 2006.

[4] D. R. Lide, ed., *CRC Handbook of Chemistry and Physics*. CRC Press: Boca Raton, FL, 75 ed., 1994.

[5] A. Michels, W. D. Graaff, T. Wassenaar, J. Levelt, and P. Louwerse, "Compressibility isotherms of hydrogen and deuterium at temperatures between -175C and +150C (at densities up to 960 amagat)," *Physica*, vol. 25, no. 1, pp. 25 – 42, 1959.

[6] Y. Yürüm, A. Taralp, and T. N. Veziroglu, "Storage of hydrogen in nanostructured carbon materials," *Int. J. Hydrogen Energy*, vol. 34, no. 9, pp. 3784–3798, 2009.

[7] M. P. Suh, H. J. Park, T. K. Prasad, and D.-W. Lim, "Hydrogen storage in metal–organic frameworks," *Chem. Rev.*, vol. 112, no. 2, pp. 782–835, 2011.

[8] L. Schlapbach and A. Züttel, "Hydrogen-storage materials for mobile applications," *Nature*, vol. 414, pp. 265–270, 2011.

[9] H. Nishihara and T. Kyotani, "Templated nanocarbons for energy storage," *Adv. Mater.*, vol. 24, no. 33, pp. 4473–4498, 2012.

[10] N. Park, K. Choi, J. Hwang, D. W. Kim, D. O. Kim, and J. Ihm, "Progress on first-principles-based materials design for hydrogen storage," *Proc. Natl. Acad. Sci. U. S. A.*, vol. 109, no. 49, pp. 19893–19899, 2012.

[11] M. Sevilla and R. Mokaya, "Energy storage applications of activated carbons: supercapacitors and hydrogen storage," *Energy. Environ. Sci.*, vol. 7, no. 4, pp. 1250–1280, 2014.

[12] S. Gadipelli and Z. X. Guo, "Graphene-based materials: Synthesis and gas sorption, storage and separation," *Prog. Mater. Sci.*, vol. 69, pp. 1 – 60, 2015.

[13] C. Chung, J. Ihm, and H. Lee, "Recent progress on kubas-type hydrogen-storage nanomaterials: from theories to experiments," *J. Korean Phys. Soc.*, vol. 66, no. 11, pp. 1649–1655, 2015.

[14] US Drive, "Target explanation document: Onboard hydrogen storage for light-duty fuel cell vehicles," tech. rep., U.S. DRIVE Partnership, 2017. `https://www.energy.gov/sites/prod/files/2017/05/f34/fcto_targets_onboard_hydro_storage_explanation.pdf`.

[15] H. Barthelemy, M. Weber, and F. Barbier, "Hydrogen storage: recent improvements and industrial perspectives," *Int. J. Hydrogen Energy*, vol. 42, no. 11, pp. 7254–7262, 2017.

[16] N. Rusman and M. Dahari, "A review on the current progress of metal hydrides material for solid-state hydrogen storage applications," *Int. J. Hydrogen Energy*, vol. 41, no. 28, pp. 12108–12126, 2016.

[17] H. Wang, H. Lin, W. Cai, L. Ouyang, and M. Zhu, "Tuning kinetics and thermodynamics of hydrogen storage in light metal element based systems–a review of recent progress," *J. Alloys Compd.*, vol. 658, pp. 280–300, 2016.

[18] C. Webb, "A review of catalyst-enhanced magnesium hydride as a hydrogen storage material," *J. Phys. Chem. Solids*, vol. 84, pp. 96–106, 2015.

[19] X. Yu, Z. Tang, D. Sun, L. Ouyang, and M. Zhu, "Recent advances and remaining challenges of nanostructured materials for hydrogen storage applications," *Prog. Mater. Sci.*, vol. 88, pp. 1–48, 2017.

[20] E. S. Cho, A. M. Ruminski, S. Aloni, Y.-S. Liu, J. Guo, and J. J. Urban, "Graphene oxide/metal nanocrystal multilaminates as the atomic limit for safe and selective hydrogen storage," *Nat. Commun.*, vol. 7, p. 10804, 2016.

[21] J. Zhang, Y. Zhu, H. Lin, Y. Liu, Y. Zhang, S. Li, Z. Ma, and L. Li, "Metal hydride nanoparticles with ultrahigh structural stability and hydrogen storage activity derived from microencapsulated nanoconfinement," *Adv. Mater.*, vol. 29, no. 24, p. 1700760, 2017.

[22] M. V. Lototskyy, I. Tolj, M. W. Davids, Y. V. Klochko, A. Parsons, D. Swanepoel, R. Ehlers, G. Louw, B. van der Westhuizen, F. Smith, *et al.*, "Metal hydride hydrogen storage and supply systems for electric forklift with low-temperature proton exchange membrane fuel cell power module," *Int. J. Hydrogen Energy*, vol. 41, no. 31, pp. 13831–13842, 2016.

[23] X. Huang, X. Xiao, W. Zhang, X. Fan, L. Zhang, C. Cheng, S. Li, H. Ge, Q. Wang, and L. Chen, "Transition metal (Co, Ni) nanoparticles wrapped with carbon and their superior catalytic activities for the reversible hydrogen storage of magnesium hydride," *Phys. Chem. Chem. Phys.*, vol. 19, no. 5, pp. 4019–4029, 2017.

[24] R. N. Muthu, S. Rajashabala, and R. Kannan, "Hexagonal boron nitride (h-BN) nanoparticles decorated multi-walled carbon nanotubes (MWCNT) for hydrogen storage," *Renewable Energy*, vol. 85, pp. 387–394, 2016.

[25] E. D. Bloch, W. L. Queen, M. R. Hudson, J. A. Mason, D. J. Xiao, L. J. Murray, R. Flacau, C. M. Brown, and J. R. Long, "Hydrogen storage and selective, reversible O2 adsorption in a metal–organic framework with open chromium (II) sites," *Angew. Chem. Int. Ed.*, vol. 55, no. 30, pp. 8605–8609, 2016.

[26] D. Gygi, E. D. Bloch, J. A. Mason, M. R. Hudson, M. I. Gonzalez, R. L. Siegelman, T. A. Darwish, W. L. Queen, C. M. Brown, and J. R. Long, "Hydrogen storage in the expanded pore metal–organic frameworks M2 (dobpdc)(M= Mg, Mn, Fe, Co, Ni, Zn)," *Chem. Mater.*, vol. 28, no. 4, pp. 1128–1138, 2016.

[27] H. G. Shiraz and M. G. Shiraz, "Palladium nanoparticle and decorated carbon nanotube for electrochemical hydrogen storage," *Int. J. Hydrogen Energy*, vol. 42, no. 16, pp. 11528–11533, 2017.

[28] M. Mananghaya, D. Yu, G. N. Santos, and E. Rodulfo, "Scandium and titanium containing single-walled carbon nanotubes for hydrogen storage: a thermodynamic and first principle calculation," *Sci. Rep.*, vol. 6, p. 27370, 2016.

[29] T. H. Kim, J. Bae, T. H. Lee, J. Hwang, J. H. Jung, D. K. Kim, J. S. Lee, D. O. Kim, Y. H. Lee, and J. Ihm, "Room-temperature hydrogen storage via two-dimensional potential well in mesoporous graphene oxide," *Nano Energy*, vol. 27, pp. 402 – 411, 2016.

[30] H. Jung, K. T. Park, M. N. Gueye, S. H. So, and C. R. Park, "Bio-inspired graphene foam decorated with Pt nanoparticles for hydrogen storage at room temperature," *Int. J. Hydrogen Energy*, vol. 41, no. 9, pp. 5019–5027, 2016.

[31] I. Cabria and A. El-Meligi, "DFT simulation of hydrogen storage on manganese phosphorous trisulphide ($MnPS_3$)," *Int. J. Hydrogen Energy*, vol. 43, no. 11, pp. 5903–5912, 2018.

[32] C. Baykasoglu, Z. Ozturk, M. Kirca, A. T. Celebi, A. Mugan, and A. C. To, "Effects of lithium doping on hydrogen storage properties of heat welded random CNT network structures," *Int. J. Hydrogen Energy*, vol. 41, no. 19, pp. 8246–8255, 2016.

[33] Z. Ozturk, C. Baykasoglu, and M. Kirca, "Sandwiched graphene-fullerene composite: a novel 3-d nanostructured material for hydrogen storage," *Int. J. Hydrogen Energy*, vol. 41, no. 15, pp. 6403–6411, 2016.

[34] J. H. Jung, D. Kim, J. Hwang, Y.-L. Lee, and J. Ihm, "Theoretical study on the hydrogen storage mechanism of the Li-Mg-N-H system," *Int. J. Hydrogen Energy*, vol. 41, pp. 17506 – 17510, 2016.

[35] L. Mattera, F. Rosatelli, C. Salvo, F. Tommasini, U. Valbusa, and G. Vidali, "Selective adsorption of 1H2 and 2H2 on the (0001) graphite surface," *Surf. Sci.*, vol. 93, no. 2-3, pp. 515–525, 1980.

[36] L. J. Murray, M. Dincă, and J. R. Long, "Hydrogen storage in metal–organic frameworks," *Chem. Soc. Rev.*, vol. 38, no. 5, pp. 1294–1314, 2009.

[37] E. Dündar-Tekkaya and Y. Yürüm, "Mesoporous mcm-41 material for hydrogen storage: A short review," *Int. J. Hydrogen Energy*, vol. 41, no. 23, pp. 9789–9795, 2016.

[38] J. Ren, N. M. Musyoka, H. W. Langmi, M. Mathe, and S. Liao, "Current research trends and perspectives on materials-based hydrogen storage solutions: a critical review," *Int. J. Hydrogen Energy*, vol. 42, no. 1, pp. 289–311, 2017.

[39] E. Ruse, S. Pevzner, I. P. Bar, R. Nadiv, V. M. Skripnyuk, E. Rabkin, and O. Regev, "Hydrogen storage and spillover kinetics in carbon nanotube-mg composites," *Int. J. Hydrogen Energy*, vol. 41, no. 4, pp. 2814–2819, 2016.

[40] A. Ariharan, B. Viswanathan, and V. Nandhakumar, "Nitrogen-incorporated carbon nanotube derived from polystyrene and polypyrrole as hydrogen storage material," *Int. J. Hydrogen Energy*, vol. 43, no. 10, pp. 5077–5088, 2018.

[41] J. Bae, J. H. Jung, Y.-L. Lee, J. Hwang, D. Kim, S. Son, and J. Ihm, "Isosteric heat of potential confinement in the hydrogen storage material," *Nano*, vol. 10, no. 08, p. 1550120, 2015.

[42] J. Bae, D. Kim, J. H. Jung, and J. Ihm, "A computational study on hydrogen storage in potential wells using K-intercalated graphite oxide," *RSC Adv.*, vol. 7, pp. 33953–33960, 2017.

[43] G. K. Dimitrakakis, E. Tylianakis, and G. E. Froudakis, "Pillared graphene: A new 3-d network nanostructure for enhanced hydrogen storage," *Nano Lett.*, vol. 8, no. 10, pp. 3166–3170, 2008.

[44] J. P. Perdew, K. Burke, and M. Ernzerhof, "Generalized gradient approximation made simple," *Phys. Rev. Lett.*, vol. 77, pp. 3865–3868, Oct 1996.

[45] R. M. Martin, *Electronic structure: basic theory and practical methods*. Cambridge University Press, 2004.

[46] J. Kohanoff, *Electronic structure calculations for solids and molecules: theory and computational methods*. Cambridge University Press, 2006.

[47] J. P. Perdew and A. Ruzsinszky, "Fourteen easy lessons in density functional theory," *Int. J. Quantum Chem.*, vol. 110, no. 15, pp. 2801–2807, 2010.

[48] G. Giuliani and G. Vignale, *Quantum theory of the electron liquid*. Cambridge University Press, 2005.

[49] A. D. Becke, "Perspective: Fifty years of density-functional theory in chemical physics," *J. Chem. Phys.*, vol. 140, no. 18, p. 18A301, 2014.

[50] K. Burke *et al.*, "The ABC of DFT." preprint on webpage at `http://dft.uci.edu/doc/g1.pdf`, 2007.

[51] W. Koch and M. C. Holthausen, *A chemist's guide to density functional theory*. John Wiley & Sons, 2015.

[52] D. Sholl and J. A. Steckel, *Density functional theory: a practical introduction*. John Wiley & Sons, 2011.

[53] P. Hohenberg and W. Kohn, "Inhomogeneous electron gas," *Phys. Rev.*, vol. 136, no. 3B, p. B864, 1964.

[54] M. Levy, "Universal variational functionals of electron densities, first-order density matrices, and natural spin-orbitals and solution of the v-representability problem," *Proc. Natl. Acad. Sci. USA*, vol. 76, no. 12, pp. 6062–6065, 1979.

[55] W. Kohn and L. J. Sham, "Self-consistent equations including exchange and correlation effects," *Phys. Rev.*, vol. 140, no. 4A, p. A1133, 1965.

[56] J. Ihm, A. Zunger, and M. L. Cohen, "Momentum-space formalism for the total energy of solids," *J. Phys. C: Solid State Phys.*, vol. 12, no. 21, p. 4409, 1979.

[57] P. E. Blöchl, "Projector augmented-wave method," *Phys. Rev. B*, vol. 50, no. 24, p. 17953, 1994.

[58] G. Kresse and D. Joubert, "From ultrasoft pseudopotentials to the projector augmented-wave method," *Phys. Rev. B*, vol. 59, no. 3, pp. 1758–1775, 1999.

[59] G. E. Scuseria and V. N. Staroverov, "Progress in the development of exchange-correlation functionals," in *Theory Appl. Comput. Chem.: First Forty Years*, pp. 669–724, Elsevier, 2005.

[60] D. M. Ceperley and B. Alder, "Ground state of the electron gas by a stochastic method," *Phys. Rev. Lett.*, vol. 45, no. 7, p. 566, 1980.

[61] F. Herman, J. P. Van Dyke, and I. B. Ortenburger, "Improved statistical exchange approximation for inhomogeneous many-electron systems," *Phys. Rev. Lett.*, vol. 22, no. 16, p. 807, 1969.

[62] P.-S. Svendsen and U. von Barth, "Gradient expansion of the exchange energy from second-order density response theory," *Phys. Rev. B*, vol. 54, no. 24, p. 17402, 1996.

[63] J. P. Perdew, K. Burke, and Y. Wang, "Generalized gradient approximation for the exchange-correlation hole of a many-electron system," *Phys. Rev. B*, vol. 54, pp. 16533–16539, Dec 1996.

[64] J. P. Perdew, K. Burke, and M. Ernzerhof, "Generalized gradient approximation made simple," *Phys. Rev. Lett.*, vol. 77, pp. 3865–3868, Oct 1996.

[65] J. Sun, M. Marsman, G. I. Csonka, A. Ruzsinszky, P. Hao, Y.-S. Kim, G. Kresse, and J. P. Perdew, "Self-consistent meta-generalized gradient

approximation within the projector-augmented-wave method," *Phys. Rev. B*, vol. 84, p. 035117, Jul 2011.

[66] J. Tao, J. P. Perdew, V. N. Staroverov, and G. E. Scuseria, "Climbing the density functional ladder: Nonempirical meta–generalized gradient approximation designed for molecules and solids," *Phys. Rev. Lett.*, vol. 91, p. 146401, Sep 2003.

[67] J. Sun, A. Ruzsinszky, and J. P. Perdew, "Strongly constrained and appropriately normed semilocal density functional," *Phys. Rev. Lett.*, vol. 115, p. 036402, Jul 2015.

[68] Y. Yao and Y. Kanai, "Plane-wave pseudopotential implementation and performance of scan meta-gga exchange-correlation functional for extended systems," *J. Chem. Phys.*, vol. 146, no. 22, p. 224105, 2017.

[69] T. Björkman, A. Gulans, A. Krasheninnikov, and R. Nieminen, "Are we van der waals ready?," *J. Phys.: Condens. Matter*, vol. 24, no. 42, p. 424218, 2012.

[70] Y. S. Al-Hamdani, D. Alfe, and A. Michaelides, "How strongly do hydrogen and water molecules stick to carbon nanomaterials?," *J. Chem. Phys.*, vol. 146, no. 9, p. 094701, 2017.

[71] I. Cabria, M. J. López, and J. A. Alonso, "Searching for DFT-based methods that include dispersion interactions to calculate the physisorption of H_2 on benzene and graphene," *J. Chem. Phys.*, vol. 146, no. 21, p. 214104, 2017.

[72] M. Kocman, P. Jurecka, M. Dubecky, M. Otyepka, Y. Cho, and K. S. Kim, "Choosing a density functional for modeling adsorptive hydrogen storage: reference quantum mechanical calculations and a comparison of dispersion-corrected density functionals," *Phys. Chem. Chem. Phys.*, vol. 17, pp. 6423–6432, 2015.

[73] N. W. Ashcroft and N. D. Mermin, *Solid State Physics*. Brooks/Cole, 1976.

[74] S. Grimme, "Semiempirical gga-type density functional constructed with a long-range dispersion correction," *J. Comput. Chem.*, vol. 27, no. 15, pp. 1787–1799, 2006.

[75] S. Grimme, J. Antony, S. Ehrlich, and H. Krieg, "A consistent and accurate ab initio parametrization of density functional dispersion correction (dft-d) for the 94 elements h-pu," *J. Chem. Phys.*, vol. 132, no. 15, p. 154104, 2010.

[76] S. Grimme, S. Ehrlich, and L. Goerigk, "Effect of the damping function in dispersion corrected density functional theory," *J. Comput. Chem.*, vol. 32, no. 7, pp. 1456–1465, 2011.

[77] D. C. Langreth, M. Dion, H. Rydberg, E. Schröder, P. Hyldgaard, and B. I. Lundqvist, "Van der Waals density functional theory with applications," *Int. J. Quantum Chem.*, vol. 101, no. 5, pp. 599–610, 2005.

[78] K. Berland, V. R. Cooper, K. Lee, E. Schröder, T. Thonhauser, P. Hyldgaard, and B. I. Lundqvist, "van der waals forces in density functional theory: a review of the vdW-DF method," *Rep. Prog. Phys.*, vol. 78, no. 6, p. 066501, 2015.

[79] M. Dion, H. Rydberg, E. Schröder, D. C. Langreth, and B. I. Lundqvist, "Van der waals density functional for general geometries," *Phys. Rev. Lett.*, vol. 92, no. 24, p. 246401, 2004.

[80] K. Lee, É. D. Murray, L. Kong, B. I. Lundqvist, and D. C. Langreth, "Higher-accuracy van der waals density functional," *Phys. Rev. B*, vol. 82, no. 8, p. 081101, 2010.

[81] I. Hamada, "van der waals density functional made accurate," *Phys. Rev. B*, vol. 89, no. 12, p. 121103, 2014.

[82] I. Hamada, "Erratum: van der waals density functional made accurate [Phys. Rev. B 89, 121103(R) (2014)]," *Phys. Rev. B*, vol. 91, p. 119902, Mar 2015.

[83] O. A. Vydrov and T. Van Voorhis, "Nonlocal van der waals density functional: The simpler the better," *J. Chem. Phys.*, vol. 133, no. 24, p. 244103, 2010.

[84] R. Sabatini, T. Gorni, and S. de Gironcoli, "Nonlocal van der Waals density functional made simple and efficient," *Phys. Rev. B*, vol. 87, p. 041108, Jan 2013.

[85] H. Peng, Z.-H. Yang, J. P. Perdew, and J. Sun, "Versatile van der waals density functional based on a meta-generalized gradient approximation," *Phys. Rev. X*, vol. 6, p. 041005, Oct 2016.

[86] L. Schlapbach and A. Züttel, "Hydrogen-storage materials for mobile applications," *Nature*, vol. 414, pp. 353–358, 2001.

[87] A. J. Churchard, E. Banach, A. Borgschulte, R. Caputo, J.-C. Chen, D. Clary, K. J. Fijalkowski, H. Geerlings, R. V. Genova, W. Grochala, T. Jaroń, J. C. Juanes-Marcos, B. Kasemo, G.-J. Kroes, I. Ljubić, N. Naujoks, J. K. Nørskov, R. A. Olsen, F. Pendolino, A. Remhof, L. Románszki, A. Tekin, T. Vegge, M. Zäch, and A. Züttel, "A multifaceted approach to hydrogen storage," *Phys. Chem. Chem. Phys.*, vol. 13, pp. 16955–16972, 2011.

[88] P. Chen, Z. Xiong, J. Luo, J. Lin, and K. L. Tan, "Interaction of hydrogen with metal nitrides and imides," *Nature*, vol. 420, pp. 302–304, 2002.

[89] T. Kar, S. Scheiner, and L. Li, "Theoretical investigation on the mechanism of LiH + NH_3 $\rightarrow$ $LiNH_2$ + H_2 reaction," *J. Mol. Struct.: THEOCHEM*, vol. 857, pp. 111–114, 2008.

[90] M. H. Park, H. Kim, J. J. Urm, J. H. Lee, Y.-K. Han, and Y. S. Lee, "Hydrogen desorption mechanism of a Li–N–H hydrogen storage system," *J. Mol. Struct.: THEOCHEM*, vol. 962, no. 1-3, pp. 68–71, 2010.

[91] Z. Lan, W. Jiang, J. Bai, and J. Guo, "The first-principles investigation on the electronic structure and mechanism of LiH + NH_3 $\rightarrow$ $LiNH_2$ + H_2 reaction," *Int. J. Hydrogen Energy*, vol. 37, no. 24, pp. 18937–18943, 2012.

[92] G. Amica, P. Arneodo Larochette, and F. C. Gennari, "Hydrogen storage properties of $LiNH_2$–LiH system with MgH_2, CaH_2 and TiH_2 added," *Int. J. Hydrogen Energy*, vol. 40, no. 30, pp. 9335–9346, 2015.

[93] R. A. Davies and P. A. Anderson, "Synthesis and characterization of two new amide chloride compounds: Potential H_2 storage materials," *Int. J. Hydrogen Energy*, vol. 40, no. 7, pp. 3001–3005, 2015.

[94] C. Liang, S. Liang, Y. Xia, H. Huang, Y.-P. Gan, X.-Y. Tao, and W.-K. Zhang, "Progress in the $Mg(NH_2)_2$–2LiH material for hydrogen storage," *Acta Phys.-Chim. Sin.*, vol. 31, no. 4, pp. 627–635, 2015.

[95] S. Ikeda, K. Tokoyoda, T. Kiyobayashi, and N. Kuriyama, "Cyclic properties and ammonia by-product emission of Li/Mg–N–H hydrogen storage material," *Int. J. Hydrogen Energy*, vol. 36, pp. 8373–8380, 2011.

[96] J. Wang, H.-W. Li, and P. Chen, "Amides and borohydrides for high-capacity solid-state hydrogen storage—materials design and kinetic improvements," *MRS Bull.*, vol. 38, pp. 480–487, 6 2013.

[97] T. Durojaiye, J. Hayes, and A. Goudy, "Potassium, rubidium and cesium hydrides as dehydrogenation catalysts for the lithium amide/magnesium hydride system," *Int. J. Hydrogen Energy*, vol. 40, no. 5, pp. 2266–2273, 2015.

[98] H. Miyaoka, Y. Wang, S. Hino, S. Isobe, K. Tokoyoda, T. Ichikawa, and Y. Kojima, "Kinetic modification on hydrogen desorption of lithium hydride and magnesium amide system," *Materials*, vol. 8, no. 7, p. 3896, 2015.

[99] G. Xia, Y. Tan, D. Li, Z. Guo, H. Liu, Z. Liu, and X. Yu, "Hierarchical porous $Li_2Mg(NH)_2$@C nanowires with long cycle life towards stable hydrogen storage," *Sci. Rep.*, vol. 4, p. 6599, 2014.

[100] B. Paik, H.-W. Li, J. Wang, and E. Akiba, "A Li–Mg–N–H composite as H_2 storage material: a case study with $Mg(NH_2)_2$–4LiH–$LiNH_2$," *Chem. Commun.*, vol. 51, pp. 10018–10021, 2015.

[101] L. H. Jepsen, M. B. Ley, Y.-S. Lee, Y. W. Cho, M. Dornheim, J. O. Jensen, Y. Filinchuk, J. E. Jørgensen, F. Besenbacher, and T. R. Jensen, "Boron–nitrogen based hydrides and reactive composites for hydrogen storage," *Mater. Today*, vol. 17, no. 3, pp. 129–135, 2014.

[102] Z. Xiong, J. Hu, G. Wu, P. Chen, W. Luo, K. Gross, and J. Wang, "Thermodynamic and kinetic investigations of the hydrogen storage in the Li–Mg–N–H system," *J. Alloys Compd.*, vol. 398, no. 1–2, pp. 235–239, 2005.

[103] J. Wang, T. Liu, G. Wu, W. Li, Y. Liu, C. M. Araújo, R. H. Scheicher, A. Blomqvist, R. Ahuja, Z. Xiong, P. Yang, M. Gao, H. Pan, and P. Chen, "Potassium-modified $Mg(NH_2)_2$/2 LiH system for hydrogen storage," *Angew. Chem. Int. Ed.*, vol. 48, pp. 5828–5832, 2009.

[104] Z. Xiong, G. Wu, J. Hu, and P. Chen, "Ternary imides for hydrogen storage," *Adv. Mater.*, vol. 16, no. 17, pp. 1522–1525, 2004.

[105] J. Lu, Z. Z. Fang, and H. Y. Sohn, "A dehydrogenation mechanism of metal hydrides based on interactions between $H^{\delta+}$ and H^{-}," *Inorg. Chem.*, vol. 45, no. 21, pp. 8749–8754, 2006.

[106] R. R. Shahi, T. P. Yadav, M. A. Shaz, and O. N. Srivastva, "Studies on dehydrogenation characteristic of $Mg(NH_2)_2$/LiH mixture admixed with vanadium and vanadium based catalysts (V, V_2O_5 and VCl_3)," *Int. J. Hydrogen Energy*, vol. 35, no. 1, pp. 238–246, 2010.

[107] V. Shukla, A. Bhatnagar, S. K. Pandey, R. R. Shahi, T. Yadav, M. Shaz, and O. Srivastava, "On the synthesis, characterization and hydrogen storage behavior of $ZrFe_2$ catalyzed Li–Mg–N–H hydrogen storage material," *Int. J. Hydrogen Energy*, vol. 40, no. 36, pp. 12294–12302, 2015.

[108] D. E. Demirocak, S. S. Srinivasan, M. K. Ram, J. N. Kuhn, R. Muralidharan, X. Li, D. Y. Goswami, and E. K. Stefanakos, "Reversible hydrogen storage in the Li–Mg–N–H system – The effects of Ru doped single walled carbon nanotubes on NH_3 emission and kinetics," *Int. J. Hydrogen Energy*, vol. 38, no. 24, pp. 10039–10049, 2013.

[109] T. Durojaiye and A. Goudy, "Desorption kinetics of lithium amide/magnesium hydride systems at constant pressure thermodynamic driving forces," *Int. J. Hydrogen Energy*, vol. 37, no. 4, pp. 3298–3304, 2012.

[110] J. Wang, P. Chen, H. Pan, Z. Xiong, M. Gao, G. Wu, C. Liang, C. Li, B. Li, and J. Wang, "Solid-solid heterogeneous catalysis: The role of potassium in promoting the dehydrogenation of the $Mg(NH_2)_2$/2 LiH composite," *ChemSusChem*, vol. 6, no. 11, pp. 2181–2189, 2013.

[111] G. Kresse and J. Furthmüller, "Efficient iterative schemes for *ab initio* total-energy calculations using a plane-wave basis set," *Phys. Rev. B*, vol. 54, no. 16, pp. 11169–11186, 1996.

[112] G. Henkelman and H. Jónsson, "Improved tangent estimate in the nudged elastic band method for finding minimum energy paths and saddle points," *J. Chem. Phys.*, vol. 113, no. 22, pp. 9978–9985, 2000.

[113] W. Tang, E. Sanville, and G. Henkelman, "A grid-based bader analysis algorithm without lattice bias," *J. Phys.: Condens. Matter*, vol. 21, no. 8, p. 084204, 2009.

[114] Y. Wang and M. Y. Chou, "First-principles study of cation and hydrogen arrangements in the Li-Mg-N-H hydrogen storage system," *Phys. Rev. B*, vol. 76, p. 014116, Jul 2007.

[115] T. Noritake, M. Aoki, M. Matsumoto, K. Miwa, S. Towata, H.-W. Li, and S. Orimo, "Crystal structure change in the dehydrogenation process of the Li–Mg–N–H system," *J. Alloys Compd.*, vol. 509, no. 28, pp. 7553–7558, 2011.

[116] H. Jacobs, "Die kristallstruktur des magnesiumamids," *Z. Anorg. Allg. Chem.*, vol. 382, no. 2, pp. 97–109, 1971.

[117] W.-Q. Deng, X. Xu, and W. A. Goddard, "New alkali doped pillared carbon materials designed to achieve practical reversible hydrogen storage for transportation," *Phys. Rev. Lett.*, vol. 92, p. 166103, Apr 2004.

[118] E. Tylianakis, G. M. Psofogiannakis, and G. E. Froudakis, "Li-doped pillared graphene oxide: A graphene-based nanostructured material for hydrogen storage," *J. Phys. Chem. Lett.*, vol. 1, no. 16, pp. 2459–2464, 2010.

[119] B. J. W., G. Srinivas, F. Jamie, S. J. M., Z. Wei, and Y. Taner, "Graphene oxide framework materials: Theoretical predictions and experimental results," *Angew. Chem., Int. Ed.*, vol. 49, no. 47, pp. 8902–8904, 2010.

[120] S. S. Han and S. S. Jang, "A hydrogen storage nanotank: lithium-organic pillared graphite," *Chem. Commun.*, pp. 5427–5429, 2009.

[121] E. Klontzas, A. Mavrandonakis, E. Tylianakis, and G. E. Froudakis, "Improving hydrogen storage capacity of mof by functionalization of the organic linker with lithium atoms," *Nano Lett.*, vol. 8, no. 6, pp. 1572–1576, 2008.

[122] R. B. Getman, J. H. Miller, K. Wang, and R. Q. Snurr, "Metal alkoxide functionalization in metal-organic frameworks for enhanced ambient-temperature hydrogen storage," *J. Phys. Chem. C*, vol. 115, no. 5, pp. 2066–2075, 2011.

[123] R. C. Lochan and M. Head-Gordon, "Computational studies of molecular hydrogen binding affinities: The role of dispersion forces, electrostatics, and orbital interactions," *Phys. Chem. Chem. Phys.*, vol. 8, pp. 1357–1370, 2006.

[124] G. Kresse and D. Joubert, "From ultrasoft pseudopotentials to the projector augmented-wave method," *Phys. Rev. B*, vol. 59, no. 3, pp. 1758–1775, 1999.

[125] G. Kresse and J. Furthmüller, "Efficient iterative schemes for *ab initio* total-energy calculations using a plane-wave basis set," *Phys. Rev. B*, vol. 54, no. 16, pp. 11169–11186, 1996.

[126] G. Henkelman, B. P. Uberuaga, and H. Jónsson, "A climbing image nudged elastic band method for finding saddle points and minimum energy paths," *J. Chem. Phys.*, vol. 113, no. 22, pp. 9901–9904, 2000.

[127] Y. Zhao and D. G. Truhlar, "A new local density functional for main-group thermochemistry, transition metal bonding, thermochemical kinetics, and noncovalent interactions," *J. Chem. Phys.*, vol. 125, no. 19, p. 194101, 2006.

[128] D. Frenkel and B. Smit, *Understanding molecular simulation: from algorithms to applications*. Academic Press, 2 ed., 2001.

[129] J. Williams, "bspline-fortran: Multidimensional B-spline interpolation of data on a regular grid," 2018. URL: `doi.org/10.5281/zenodo.1215290`.

[130] D. C. Johnston, *Advances in Thermodynamics of the van der Waals Fluid*. 2053-2571, Morgan & Claypool Publishers, 2014.

[131] J. Rychlewski, "An accurate calculation of the polarizability of the hydrogen molecule and its dependence on rotation, vibration and isotopic substitution," *Mol. Phys.*, vol. 41, no. 4, pp. 833–842, 1980.

[132] A. Besserguenev, A. Fogg, R. Francis, S. Price, D. O'hare, V. Isupov, and B. Tolochko, "Synthesis and structure of the gibbsite intercalation compounds [LiAl2 (OH) 6] X {X= Cl, Br, NO3} and [LiAl2 (OH) 6] Cl· H2O using synchrotron X-ray and neutron powder diffraction," *Chemistry of Materials*, vol. 9, no. 1, pp. 241–247, 1997.

[133] D. Kim, J. H. Jung, and J. Ihm, "Theoretical study of aluminum hydroxide as a hydrogen-bonded layered material," *Nanomaterials*, vol. 8, no. 6, p. 375, 2018.

[134] D. Rickard and G. W. Luther, "Chemistry of iron sulfides," *Chem. Rev.*, vol. 107, no. 2, pp. 514–562, 2007.

[135] K. D. Kwon, K. Refson, S. Bone, R. Qiao, W.-l. Yang, Z. Liu, and G. Sposito, "Magnetic ordering in tetragonal FeS: Evidence for strong itinerant spin fluctuations," *Phys. Rev. B*, vol. 83, p. 064402, Feb 2011.

[136] X. Lai, H. Zhang, Y. Wang, X. Wang, X. Zhang, J. Lin, and F. Huang, "Observation of superconductivity in tetragonal FeS," *J. Am. Chem. Soc.*, vol. 137, no. 32, pp. 10148–10151, 2015.

[137] J. R. Miller and P. Simon, "Electrochemical capacitors for energy management," *Science*, vol. 321, no. 5889, pp. 651–652, 2008.

[138] M. Winter and R. J. Brodd, "What are batteries, fuel cells, and supercapacitors?," *Chem. Rev.*, vol. 104, no. 10, pp. 4245–4270, 2004.

[139] X. Lai, Z. Lin, K. Bu, X. Wang, H. Zhang, D. Li, Y. Wang, Y. Gu, J. Lin, and F. Huang, "Ammonia and iron cointercalated iron sulfide $(NH_3)Fe_{0.25}Fe_2S_2$: hydrothermal synthesis, crystal structure, weak ferromagnetism and crossover from a negative to positive magnetoresistance," *RSC Adv.*, vol. 6, pp. 81886–81893, 2016.

[140] N. Dzade, A. Roldan, and N. H. de Leeuw, "DFT-D2 simulations of water adsorption and dissociation on the low-index surfaces of mackinawite (FeS)," *J. Chem. Phys.*, vol. 144, no. 17, p. 174704, 2016.

[141] N. Dzade, A. Roldan, and N. H. de Leeuw, "DFT-D2 study of the adsorption and dissociation of water on clean and oxygen-covered $\{001\}$ and $\{011\}$ surfaces of mackinawite (FeS)," *J. Phys. Chem. C*, vol. 120, no. 38, pp. 21441–21450, 2016.

[142] N. Y. Dzade, A. Roldan, and N. H. de Leeuw, "Adsorption of methylamine on mackinawite (FeS) surfaces: A density functional theory study," *J. Chem. Phys.*, vol. 139, no. 12, p. 124708, 2013.

[143] N. Dzade, A. Roldan, and N. H. de Leeuw, "Surface and shape modification of mackinawite (FeS) nanocrystals by cysteine adsorption: a first-principles DFT-D2 study," *Phys. Chem. Chem. Phys.*, vol. 18, no. 47, pp. 32007–32020, 2016.

[144] N. Dzade, A. Roldan, and N. H. de Leeuw, "The surface chemistry of NO_x on mackinawite (FeS) surfaces: a DFT-D2 study," *Phys. Chem. Chem. Phys.*, vol. 16, no. 29, pp. 15444–15456, 2014.

[145] N. Dzade, A. Roldan, and N. H. de Leeuw, "Activation and dissociation of CO_2 on the (001),(011), and (111) surfaces of mackinawite (FeS): a dispersion-corrected DFT study," *J. Chem. Phys.*, vol. 143, no. 9, p. 094703, 2015.

[146] W. Tang, E. Sanville, and G. Henkelman, "A grid-based bader analysis algorithm without lattice bias," *J. Phys.: Condens. Matter*, vol. 21, no. 8, p. 084204, 2009.

[147] S. Lebègue, T. Björkman, M. Klintenberg, R. M. Nieminen, and O. Eriksson, "Two-dimensional materials from data filtering and ab initio calculations," *Phys. Rev. X*, vol. 3, p. 031002, Jul 2013.

[148] D. Welz and M. Rosenburg, "Electronic band structure of tetrahedral iron sulphides," *J. Phys. C: Solid State Phys.*, vol. 20, no. 25, p. 3911, 1987.

[149] N. Hao, F. Zheng, P. Zhang, and S.-Q. Shen, "Topological crystalline antiferromagnetic state in tetragonal FeS," *Phys. Rev. B*, vol. 96, p. 165102, Oct 2017.

[150] J. Kübler, "Magnetic moments of ferromagnetic and antiferromagnetic bcc and fcc iron," *Phys. Lett. A*, vol. 81, no. 1, pp. 81 – 83, 1981.

[151] C. Kittel and P. McEuen, *Introduction to Solid State Physics*. John Wiley and Sons, 8 ed., 2005.

[152] R. Skala, I. Cisarova, and M. Drabek, "Inversion twinning in troilite," *Am. Mineral.*, vol. 91, no. 5-6, p. 917, 2006.

[153] P. Raybaud, G. Kresse, J. Hafner, and H. Toulhoat, "Ab initio density functional studies of transition-metal sulphides: I. crystal structure and cohesive properties," *J. Phys.: Condens. Matter*, vol. 9, no. 50, p. 11085, 1997.

[154] W. Wang, S. Dai, X. Li, J. Yang, D. J. Srolovitz, and Q. Zheng, "Measurement of the cleavage energy of graphite," *Nat. Commun.*, vol. 6, p. 7853, Aug. 2015.

[155] M. Wiebcke and J. Felsche, "$NEt_4OH{\cdot}4H_2O$ containing infinite hydroxide–water ribbons," *Acta Crystallogr., Sect. C: Cryst. Struct. Commun.*, vol. 56, pp. 901–902, Jul 2000.

국문초록

만일 수소를 에너지 전달자(carrier)로 사용할 수 있다면 차량에서 사용하는 화석연료에 의한 오염이 의미있게 감소할 수 있다. 수소 저장은 이 수소 에너지의 상용화 응용을 위한 중대한 연구주제이다. 현재 수소는 700기압의 고압용기에 저장되고 있어 이는 잠재적인 위험을 내포하고 있다.

첫째로, 화학결합을 사용한 마그네슘 아미드($Mg(NH_2)_2$) 내의 수소 저장을 연구하였다. 이는 고압용기를 대체할 수 있는 안전한 방법인데, 그 연유는 강한 화학결합이 수소기체를 고체 안에 안정화시키기 때문이다. 마그네슘 아미드와 리튬 수소화물(LiH)은 볼로 분쇄되면 (ball milling) 수소를 발생한다. KH가 이 시스템에 삽입되면 높은 수소 방출 온도가 감소하는 것으로 알려져 있다. 실제적인 응용을 위해서는, 이 온도는 더 감소하여야 하며, 이 목적을 위해서 이 반응의 기초적인 이해가 요구된다. 수소가 이 시스템의 원자들과 하는 상호작용과 이 반응에 대한 KH의 영향은 아직 분자 수준에서 연구되지 않았다. 여기서, 우리는 $Mg(NH_2)_2$와 LiH 가 기체상태에서 반응하면 H_2가 방출되는 반응의 기작에 대한 설명을 목표로 하고자 한다. 여기에 우리는 제일원리를 사용하여 밀도 범함수 이론으로 전자구조와 총에너지 계산을 이용하였다. 우리는 또한 KH가 그 반응에 영향을 주는 기작을 연구하였다.

둘째로, 우리는 층상물질의 포텐셜 우물 안의 수소저장을 제안한다. 이는 화학결합으로 이루어진 시스템의 높은 반응온도와 늦은 반응속도를 보완하기 위함이다. 이 시스템에 H_2를 충전과 방전하는 것은 느린데, 그 이유는 H_2의 강한 화학결합이 끊어지고, 다시 형성되어야 하기 때문이다. 층상 물질은 이 시스템들보다 나은데, 물리흡착에 의해 상대적으로 약한 상호작용이 H_2의 탈착과 흡착 속도를 증가시키기 때문이다. 두가지 층상 물질의 후보는 층간삽

입된 깁사이트(gibbsite)와 층간삽입된 FeS이다.

층간삽입된 깁사이트의 수소저장 기작이 연구되었다. 구체적으로, $NiSO_4$가 층간삽입된 깁사이트와 $Ni(COO)_2$가 층간삽입된 깁사이트가 연구되었다. 우리는 H_2 분자의 이 시스템에 대한 결합에너지를 계산하였다. 물리흡착의 강도는 H_2 를 저압, 상온에서 높은 반응속도로 저장하는데 유리하였다. 우리는 상온에서의 저장량을 그랜드 캐노니칼 몬테 카를로 모사(grand canonical Monte Carlo simulation)을 사용하여 추정하였다. 또한, 다른 층상 물질 후보인 FeS의 전자구조, 흡착과 층간삽입에 대해 연구되었다. 이 물질은 높은 표면적을 가지고 있고, 금속성이기 때문에 이 물질은 초고용량 축전기(supercapacitor)로도 유용할 수 있다. 층간 삽입되는 분자의 크기가 NH_3에서 수산화 테트라알킬암모늄 (tetraalkylammonium hydroxides) (수산화 테트라에틸암모늄 (tetraethylammonium hydroxide)과 수산화 테트라부틸암모늄 (tetrabutylammonium hydroxide))로 증가하자 층간거리가 증가하였다. 층간 거리의 조정은 이 물질을 수소저장물질이나 초고용량축전기 전극으로 사용하기 위해 최적화하는데 유용할 것이다. 전하 이동과 층간삽입 에너지가 계산되었다. 또한, 이 물질에 대한 기초적인 연구로, FeS 단일층과 덩어리(bulk)의 전자구조가 비교되었다. 실험 조건에서 흔히 존재하는 원자와 분자의 흡착도 연구되었는데, 이는 추후 실험에 대한 참고자료가 될 것이다.

주요어 : 수소 저장, 슈퍼커패시터, 층상 물질, 밀도 범함수 이론, 마그네슘 아미드($Mg(NH_2)_2$), 깁사이트($Al(OH)_3$), 정방 정계 FeS (막키나와이트)

학번 : 2011-20422